Ingenieurfakultät Bau Geo Umwelt
Lehrstuhl für Geodäsie

Terrestrial Laser Scanning Technology from Calibration to Registration with Respect to Deformation Monitoring

Xuming Ge

Vollständiger Abdruck
der von der Ingenieurfakultät Bau Geo Umwelt
der Technische Universität München
zur Erlangung des akademischen Grades eines
Doktor-Ingenieurs (Dr.-Ing.)
genehmigten Dissertation.

Vorsitzender:
Univ. Prof. Dr. –Ing. Uwe Stilla

Prüfer der Dissertation:
1. Univ. Prof. Dr.-Ing. habil. Thomas Wunderlich
2. Univ. Prof. Dr. techn. Andreas Wieser
3. Univ. Prof. Dr.-Ing. Hans-Berndt Neuner

Die Dissertation wurde am 13.09.2016 bei der Technische Universität München eingereicht und durch die Ingenieurfakultät Bau Geo Umwelt am 20.10.2016 angenommen

Abstract

For several years now, terrestrial laser scanning (TLS) has been applied to metrology in geodesy and survey engineering. Since TLS is able to determine the spatial coordinates of a remote object using laser light and can obtain a huge high-resolution three-dimensional (3D) data set for an object of interest from just a single scan, it has become a standard surveying procedure in architecture, engineering, and construction, with a wide range of applications.

However, the application of TLS has some limitations. On the one hand, information from TLS is always expressed as a vast point cloud of 3D coordinates with a relatively random distribution on the scanning object's surface, and therefore it is not possible to extract the exact coordinates of a position of interest directly from the raw point cloud. On the other hand, the accuracy of TLS results is limited by a variety of factors, including uncompensated instrument biases, target surface structure and material properties, atmospheric effects, residual deviations of point cloud registration, among others. Thus, the first two objectives of this thesis focus on target identification and calibration in TLS. These two steps belong to the pre-processing of the point cloud. In the second half of this thesis, I will be concerned with post-processing of point clouds and the application of TLS. The topic most often discussed with regard to point clouds is 3D reconstruction (e.g., the digital city). The key technique in this area is rigid registration of point clouds (i.e., the assumption that two or more 3D point clouds are related by a rigid transformation). The goal of rigid registration is to align two or more point clouds that have been captured from different scanning perspectives. This thesis will go into the issue of rigid registration and provide a new algorithm to carry out this process. The final objective in this thesis is non-rigid registration. This is one of the state-of-the-art approaches in the post-processing of point clouds and has real potential for enabling TLS to handle the problems of deformation monitoring. Specifically, in this chapter of the thesis, deformation related information is not based on a single point from different epochs. Moreover, based on non-rigid registration, a real 3D deformed model can become a reality, with the ability to provide clear benefits compared with the 2.5D deformed models used in recent projects.

This dissertation is based on four scientific publications, which have been framed by an introduction and a concluding chapter. Publication 1 focuses on target identification in TLS. In this paper, we investigate the use of normal information from all kinds of scanners to calculate the center of a target. In order to verify the generality of the results, we exploit A4 paper targets in the tests, instead of the special material targets supplied with particular brands of scanners. Publication 2 describes TLS calibration. Based on a systematic error model and a stochastic

model, we derive different criteria for estimating the precision of each additional parameter, as well as correlations between parameters. After having generated such criteria, we search for different configurations to satisfy these requirements. Publications 3 and 4 concentrate on registration issues. Rigid and non-rigid cases are discussed separately in these papers. In the rigid case, we provide a variant least squares 3D surface-matching algorithm to deal with different kinds of observational errors in both source and target point clouds and further reveal the possibility of analyzing the error behavior of each point cloud. In the non-rigid case, we display the potential of the four-point congruent set algorithm to generate correspondence from deformed surfaces. An automatic method to execute non-rigid registration is proposed in publication 4, in which we further show the potential of the proposed method for 3D reconstruction and deformation monitoring.

Zusammenfassung

Terrestrisches Laserscanning ist bereits seit einigen Jahren eine anerkannte Messmethode in der Geodäsie und im Bereich der Ingenieurvermessung. Da es sich dabei um eine Technik handelt, die mit Laserlicht die räumlichen Koordinaten interessierender Objekte aus der Distanz erfassen und mittels eines einzigen Scans große, hochaufgelöste 3D-Datensätze erzeugen kann, ist das terrestrische Laserscanning heute eine Standard-Vermessungsmethode in Architektur, Ingenieurwesen und Bausektor mit einem großen Spektrum an Anwendungen.

Dennoch hat die Anwendung des terrestrischen Laserscannings einige Einschränkungen. Zum einen bestehen die Daten der Laserscanner immer aus riesigen 3D-Punktwolken, welche auf der gescannten Objektoberfläche relativ willkürlich verteilt sind, so dass die Koordinaten eindeutig definierter Positionen von Interesse nicht unmittelbar aus den Rohdaten entnommen werden können. Zum anderen ist die Genauigkeit terrestrischer Laserscanner aufgrund einer Vielzahl von Faktoren beschränkt, wozu unkompensierte Instrumentenabweichungen, Oberflächenstruktur und Materialeigenschaften des Zielobjekts, atmosphärische Effekte, Restklaffungsabweichungen bei der Punktwolkenregistrierung und andere gehören. Daher fokussieren die ersten beiden Zielstellungen dieser Arbeit auf der Bestimmung von Zielpunkten und auf der Kalibrierung beim terrestrischen Laserscanning (TLS). Diese zwei Schritte gehören zur Vorprozessierung von Punktwolken. Die zweite Hälfte dieser Arbeit wird sich mit der Nachprozessierung von Punktwolken und TLS Anwendungen beschäftigen. Das populärste Thema im Bereich der Punktwolken ist die 3D-Rekonstruktion, z.B. in digitalen Stadtmodellen. Die entscheidende Vorgehensweise ist dabei die Starrkörperregistrierung von Punktwolken (d.h. es wird angenommen, dass zwei oder mehr 3D Punktwolken durch eine Starrkörpertransformation in Beziehung gesetzt werden können). Das Ziel der Starrkörperregistrierung ist es, zwei oder mehr Punktwolken unterschiedlicher Scanperspektiven zusammenzuführen. Diese Arbeit wird die Aufgabenstellung der Starrkörperregistrierung aufnehmen und einen alternativen Algorithmus für die Ausführung dieses Vorgangs präsentieren. Das letzte Ziel dieser Arbeit ist die Registrierung nicht-starrer Körper. Diese ist eine der modernsten Technologien in der Nachprozessierung von Punktwolken, die für das terrestrische Laserscanning echtes Potenzial zur Behandlung von Deformationsüberwachungsaufgaben birgt. Die Ableitung eines Einzelpunkts aus einer Rohdaten-Punktwolke im TLS ist nämlich unsinnig, da die Deformation hier nicht mehr über einen Einzelpunkt an einer definierten Position repräsentiert wird, sondern über eine beliebig gelagerte Oberfläche. Darüber hinaus wird durch eine nicht-starre Registrierung ein echtes 3D-Deformationsmodell möglich, welches klare Vorteile gegenüber den 2,5D-Modellen gegenwärtiger Projekte hat.

Diese Dissertation gliedert sich in sieben Kapitel. Am Anfang wird eine Einführung in die Arbeit gegeben. Die Motivation, in Beziehung stehende Arbeiten und Beiträge werden im ersten Kapitel kurz vorgestellt. Danach werden die wichtigsten Werkzeuge eingeführt, die in den späteren Abschnitten verwendet werden. In diesem Kapitel werden auch ausschlaggebende Formulierungen und Definitionen festgesetzt. Kapitel 3 fokussiert auf der Identifizierung von Zielpunkten. Dabei sollen gebräuchliche Informationen genutzt werden, die von allen Arten von Scannern erfasst und zur Berechnung von Zielmarkenzentren verwendet werden können. Um sicherzustellen, dass der Ansatz allgemeingültig ist, werden in den Untersuchungen A4-Papier-Zielmarken verwendet anstatt spezieller, auf die jeweilige Scannermarke zugeschnittener Zielzeichen aus speziellen Materialien. Kapitel 4 beschreibt die Kalibrierung terrestrischer Laserscanner. Basierend auf einem Modell systematischer Fehlereinflüsse und einem stochastischen Modell werden verschiedene Kriterien zur Beurteilung der geschätzten Präzision und Korrelationen nach einer Kalibrierung abgeleitet. Nachdem diese Kriterien festgelegt worden sind, werden verschiedene lokale optimale Konfigurationen untersucht, die diese Anforderungen erfüllen. Ein Hauptzweck dieses Kapitels ist es, dass die Ergebnisse einer Kalibrierung durch einen festen Satz an Parametern beschrieben werden können. Kapitel 5 und 6 konzentrieren sich auf Registrierungsaufgaben in Starrkörper- und Nicht-Starrkörper-Fällen. Für den Starrkörperfall wird eine neue Variante eines 3D-Oberflächen-Matchingalgoritmus auf Basis der Kleinsten Quadrate gezeigt, welche verschiedene Arten von Beobachtungsfehlern sowohl in den Quell- wie in den Zielpunktwolken behandelt; außerdem wird dessen Fähigkeit aufgezeigt, das Fehlerverhalten jeder Punktwolke nach der Registrierung zu analysieren. Im nicht-starren Fall wird das Potenzial einer Variante des 4-Point Congruent Set – Algorithmus (4PCS) gezeigt, Beziehungen einer Original-Oberfläche zu ihrer deformierten Oberfläche zu erzeugen. Eine automatische Methode zur Durchführung einer nicht-starren Registrierung wird in diesem Kapitel vorgeschlagen. Schließlich folgen am Ende der Arbeit eine Zusammenfassung und ein Ausblick.

Contents

Chapter 1

Introduction

The exploitation of three-dimensional (3D) information is one of the key techniques in the recent digital age. For example, when attempting to provide an accurate representation of the surface of an object, it is necessary to efficiently obtain a huge amount of 3D data. Terrestrial laser scanning (TLS) is an exact technique that determines the spatial coordinates of a remote object using laser light, and its high resolution allows TLS to acquire a huge 3D data set from just a single scan of the target object. Furthermore, in the fast-paced laser scanner market, the capabilities of instruments are continually improving, including with regard to accuracy, resolution, and speed. All of these aspects have made TLS an increasingly popular technique in the fields of geodetic engineering and geo-information.

However, the limitations of TLS have also recently become obvious. First and foremost, the data from TLS cannot be directly exploited for projects. Both pre- and post-processing are necessary steps for each program when it needs to handle a raw point cloud. Second, since information from TLS is always expressed as a huge point cloud of 3D coordinates with a relatively random distribution on an object's surface, the density of point clouds decreases with distance, leading to an uneven point distribution, so that it is difficult to extract a specific position from a point cloud. Moreover, because of the working principle on which laser scanners are based, it is not feasible to reach the same accuracy as with a total station in terms of a specific position. However, information on a specific position is always key for a measurement project (e.g., to generate control points and subsequently establish a network). Last, but not least, the quality of point clouds from laser scanners is limited by a variety of factors, including uncompensated instrument biases, target surface structure and material properties, atmospheric effects, and others.

Although the aforementioned limitations remain in TLS applications, the potential of TLS in geodetic engineering and geo-information is also obvious. In this digital age, 3D digital models are becoming more and more frequently used. One of the most popular applications of TLS is in 3D reconstruction. The huge amount of data from a single scan gives TLS the capability to provide greater detail about an object's surface by using 3D coordinate information than any traditional measurement instrument, such as a total station. Point cloud registration is one of

the most important techniques in 3D reconstruction. This allows one to match point clouds of a scanned object from different perspectives in order to obtain a complete 3D model of the object. Usually, a scanned object is stationary (or nearly so) and so its surfaces are fixed. It is therefore necessary to move a laser scanner to different places around the object when capturing scanning data in order to avoid some parts being blocked by others, which would occur when scanning from a single perspective. In rigid registration, the point clouds need only be subject to a rigid-body transformation and be aligned with each other based on the correspondences in their areas of overlap. However, scanned objects are not always stationary and may have different orientations or different degrees of deformation at different epochs, with the result that it may not be possible to align two corresponding point clouds by a rigid-body transformation. In order to deal with these issues, non-rigid registration of point clouds has become an important area of research in TLS.

Overriding research questions. Taking into account the aforementioned limitations on TLS and its applications, this thesis looks into recent developments aimed at further advancing the TLS technique. The exploration of TLS here will be focused on the fields of geodetic engineering and geo-information, as was done in the early days of computer vision. In this context, it asks the following questions:

1. Is there a general technique to extract target centers from raw point clouds to represent specific positions?
2. Can we predict a feasible configuration to complete the calibration of a laser scanner to provide the expected results?
3. Can we register point clouds that are captured by different sensors and then further separately carry out a precision assessment for each sensor after an adjustment?
4. Can we align two point clouds that are obtained from different epochs when the scanned object within the overlapping scan areas has different deformation in different epochs?

This thesis will address these four questions in turn, in preparation for employing TLS technology for deformation monitoring.

1.1 Motivation

As already mentioned, this thesis focuses on TLS in the areas of geodetic engineering and geo-information. Therefore, we attempt to answer the above questions from the point of view of measurement and derive further motivation for our research.

Question 1: Is there a general technique to extract target centers from raw point clouds to represent specific positions?

Recent commercially available laser scanners for TLS always have specific dedicated software for extracting an artificial target center from a raw point cloud. The algorithm for target center extraction is a black-box, thus users will typically use the accompanying targets supplied by the scanner manufacture such that to obtain sufficient accuracy. But, users do not choose accompanying targets all the time but have a limited number available because as a rule those targets are always expensive. Moreover, those accompanying targets are not easy to install at some special places e.g. a roof. So, this a bottleneck in the TLS applications i.e. the accuracy of target center extraction mainly relates to the special targets and accompanying algorithm. Although recently more and more research has come to focus on the use of natural landmarks instead of artificial targets to avoid limitations imposed, for example, by a lack of information regarding scanner programming, this has led to a decrease in accuracy.

Considering the above limitations, we attempt here to investigate a general extraction approach for artificial targets in which no specific detailed information on the core aspects of the instrument's processing system is needed, nor are there any restrictions placed on the material composition of the target object. If the above expectations can be satisfied, then the approach presented here will have the two important properties of universality and repeatability, which means that we can apply the same algorithm with different brands of scanner.

The throughout results of this question is presented with permission from **X. Ge and T. Wunderlich 2015. Target Identification in Terrestrial Laser Scanning. *Survey Review*, vol. 47, pp. 129-140.**

Question 2: Can we predict a feasible configuration to complete the calibration of a laser scanner to provide the expected results?

Improve the qualities of the raw point clouds is a key method to significantly improve the accuracy of the TLS technique. Calibration is a powerful approach to doing this and is therefore currently attracting great interest. Scanners can be calibrated by component calibration or by system calibration. In this thesis, we are particularly interested in system calibration. In recent years, there has been much research on TLS system calibration and many valuable results have been obtained. However, so far, no specific rules have been given for predicting and assessing whether the accuracy of the additional parameters (APs), i.e. the adding parameters to model the biases of scanner measurements, obtained with a particular calibration point field and measurement set up is sufficient. In other words, there is no general rule to judge whether the calibration results can make the effect of instrumental biases negligible compared with other effects. Moreover, as far as we know, there are no specific research results providing guidance for users about how to establish their own point field and to execute their own calibration in order to obtain their expected results with minimal effort.

Taking into account the above requirements, this thesis attempts to fill this gap by proposing a criterion for relating predictable quality indicators to application requirements and by deriving related configuration requirements for the point field and scanner setup. After generating such a criterion and configurations, users can rely on the presented rules and guides to establish their own point field and then execute a system calibration. As mentioned above, the greatest benefit of such a point field is that the results of the calibration can then be predicted.

The throughout results of this question is presented with permission from **X. Ge, A. Wieser and T. Wunderlich. Configuration Requirements for Terrestrial Laser Scanner Calibration within a Point Field. Submit to the journal of *IEEE Transactions on Geoscience and Remote Sensing*. 2016. Under review.**

Question 3: Can we register two kinds of point cloud that are captured by two different sensors and then further assess the behavior of each kind of residual after adjustment?

Point cloud registration is one of the most important techniques in 3D reconstruction. In the early days, this topic was mostly explored in the field of computer vision. However, with rapid advances in its performance capabilities, TLS is currently attracting great interest also in geodetic engineering and geo-information. For computer vision, the primary concern with regard to registration is the need to align two point clouds accurately and quickly, whereas in geodetic engineering and geo-information, it is also desired to assess the registered point clouds after adjustment. In recent research, stochastic models have usually been employed to reflect the properties of observations, but there has been little discussion about how to assess precision if the registered point clouds are captured by different sensors. This means that the *source* and *target* point clouds may be captured by different sensors with different properties (e.g., different resolutions, different scales, and different degrees of precision).

Taking into account the limitations and the requirements of TLS in the field of measurement, we attempt in this thesis to address the above problems. The algorithm presented here allows the exploration of different properties of different kinds of observations; moreover, it is possible to envisage multi-source data fusion in point cloud registration.

The throughout results of this question is presented with permission from **X. Ge, and T. Wunderlich 2016. Surface-based matching of 3D point clouds with variable coordinates in source and target system. *ISPRS Journal of Photogrammetry and Remote Sensing*, vol. 111, pp. 1-12.**

Question 4: Can we align two point clouds that are obtained from different epochs when the scanned object has different orientations in each epoch?

Registration techniques can be classified as either rigid registration or non-rigid registration. As already mentioned, in rigid registration, the scanned objects are not deformed, so the goal is to find a six degrees of freedom (DoF) rigid-body transformation between two scans. However,

in measurement projects, the hypothesis of rigid registration (i.e., that the scanned object is stationary) does not always hold; i.e., the scanned object may undergo deformation and may have different orientations at different epochs. Generally, in the context of measurement, we classify these issues as deformation monitoring. In computer vision, the technique for dealing with registration problems arising from deformed point clouds is called non-rigid registration. Even in the relatively advanced field of computer vision, this procedure is still in its infancy, but, nevertheless, in this thesis, we shall attempt to introduce a non-rigid registration technique into deformation monitoring. In geodetic framework and/or measurement field, the rigid registration is primarily used to transform non-overlapping parts of point clouds into a public coordinate system using the overlapping parts. While, the non-rigid registration is used to assess changes within the overlapping parts and has no use whatsoever for non-overlapping parts. Given the absence of such techniques in the field of measurement, we shall try to present a reasonable algorithm for handling non-rigid registration cases. Specifically, we want to introduce more geo-reference information (e.g., control points in a control network) into the approach in order to improve the precision of registration. Furthermore, we shall use a real 3D model to reflect deformation information from a terrestrial laser scanner.

The throughout results of this question is presented with permission from **X. Ge, 2016. Non-rigid registration of 3D point clouds under isometric deformation. *ISPRS Journal of Photogrammetry and Remote Sensing*, vol.121, pp.192-202.**

1.2 Contributions

In this thesis, we will discuss the use of TLS for measurement. Specifically, we attempt to introduce TLS techniques into deformation monitoring and address some specific issues. Subsequently, we will answer the question of what the proposed approach can be used for.

Technically, after solving the first question raised in Section 1.1, we will obtain a general approach for extracting target centers from raw point clouds. No specific or core information on particular scanners is required and there are no specific requirements on target material, so users of this technique should be able to obtain target centers from raw point clouds with different brands of scanners without the need for dedicated software. Moreover, based on the general approach presented here, users can objectively compare different brands of scanners.

The point-field calibration approach presented here gives users the possibility of obtaining expected results with a given configuration. First of all, users can find reasonable rules to adjust the precision of a given estimated parameter in order to make bias negligible. Second, they can establish a particular point-field to execute calibration within a given subset of APs and then to obtain the expected precision of estimated APs.

To solve the third question posed in Section 1.1, we propose a Gauss–Helmert least squares 3D matching approach. The proposed approach not only allows users to align two overlapping point clouds effectively, but also provides the capability to assess the registered point clouds. With the proposed approach, the properties of different kinds of captured data can be fully considered in the calculation, thus providing further possibilities for users to handle multi-source data fusion.

Finally, we extend the TLS technique to deformation monitoring. We propose a novel combination approach to the solution of deformation issues by using a non-rigid registration technique within point clouds. Users can employ the proposed approach to effectively align two deformed point clouds. Moreover, geo-reference points can be introduced into the adjustment. Users can also obtain real 3D information, i.e., 3D translations and three rotation angles (e.g., Euler angles), instead of just 2.5D information on deformation.

In summary, this thesis proposes four different approaches in an attempt to address a number of questions arising in the application of deformation monitoring by TLS. Users can employ the method proposed here to solve a number of issues ranging from data quality to data registration.

1.3 Related work

In this section, we discuss the development of the proposed technique for TLS and briefly introduce the concepts and experimental realization of the proposed approaches. In order to allow readers to trace different references to the corresponding topics, we will divide this section into four subsections based on the four questions posed in Section 1.1. To begin each subsection, links to important literature will be given and then the key ideas of the proposed approach will be introduced, following which we will briefly describe our experiments on each topic.

1.3.1 Target identification

Research on target identification is divided into two categories, namely, specific target detection and extraction of a target center. After detecting an artificial target, an appropriate extraction program is employed to calculate the center of the target. Specific target detection deals with recognizing a particular example of an object (e.g., an HDS target) from a raw point cloud. The goal of extracting a target center is to calculate the coordinates of an artificial target, and, in most situations, this calculation is based on the results from the detection technique. In this thesis, we shall not consider the former technique but will concentrate on the extraction of a target center.

There are many valuable results in the early literature regarding the topic of target center extraction. Lichti et al. (2002) proposed three radiometric approaches based on intensity to define the target center respectively as the position with the maximum radiance, the radiometric center of the four strongest returns, and the radiometric center of all returns. All these approaches are based on the assumption that the maximum intensity is recorded from the target center. This assumption is also made in target design (Reshetyuk, 2009). However, it is violated at non-normal incidences because the recorded intensity falls off with increasing beam incidence angle. This will cause the function of automatic target recognition in the scanning software to fail, with a consequent loss of the target center. In later work, the third method (Lichti et al., 2002) was shown to perform better than the other two; however, it cannot render reliably accurate results. Valanis and Tsakiri (2004) evaluated the above-mentioned approaches for a Leica HDS 2500 scanner. They employed the c-means method to extract the target center, and the results that they described were better than those obtained by previous methods. The precision of a derivative target center can be estimated using the error propagation law in the least square adjustments. Lichti and Gordon (2004) presented an alternative estimate of the precision of the target center by introducing the angular position. One thing that should be pointed out here is that the precision of the target center position depends not only on the algorithm used for the extraction but also on the point-cloud quality. However, in order to independently investigate the performance of the proposed extraction algorithm, we shall assume here that the quality of the point clouds is sufficient. Interested readers can find further information regarding this topic in Thiel and Wehr (2004), Lichti et al. (2005), Gordon (2005), Boehler and Marbs (2005), and Schulz (2008).

Taking into account the requirement of the proposed approach raised in the first question in Section 1.1 and combining this with results from the early literature, we only employ common information, i.e., coordinates and intensities, to calculate the target center. In terms of geometric shape, spheres and quadrant planes are the principal artificial targets currently used in TLS; see Figure 1.1a and 1.1b, respectively. From the point of view of ease and economy of use in a real scanning project, the plane form is better than the spherical one. Moreover, in order to make the proposed algorithm more general, we used A4 paper targets (Figure 1.1c) in our experiments, rather than the target supplied with the scanner and shown in Figure 1.1b. This also has a benefit in terms of cost, given that the latter targets are relatively expensive and a large number may be needed in a real scanning project.

The main idea of the proposed method is to accurately find two cross lines in a target point cloud and then calculate the intersection to represent the target center. In a real scanning project, the scanner beams are not always perpendicular to targets, with the result that there is an incident angle from the scanner to a given target (see Figure 1.2a). Therefore, we simulated different incidence angles in our experiments by using special equipment (see Figure 1.2b) to ensure that our approach is effective in different cases.

(a) *(b)* *(c)*

Figure 1.1 Different artificial targets for TLS: (a) a sphere target; (b) a quadrant plane target; (c) an A4 paper quadrant plane target.

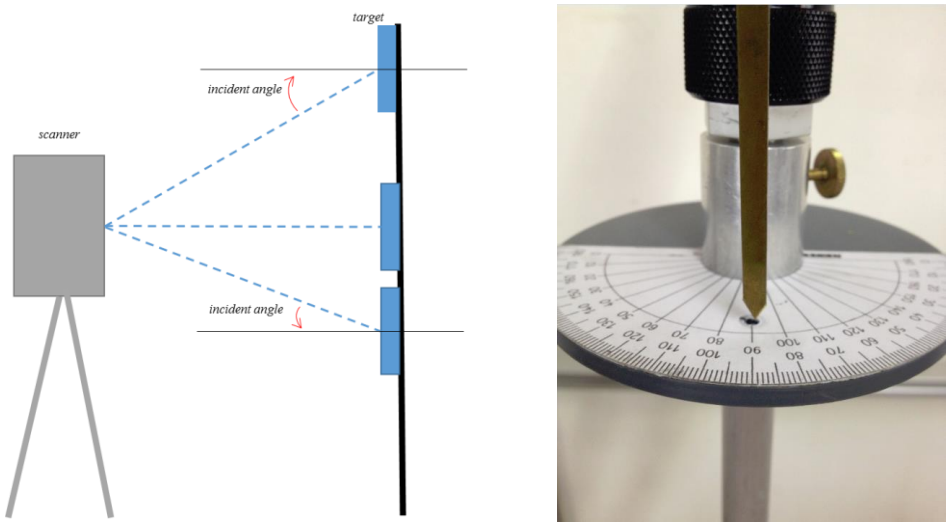

(a) *(b)*

Figure 1.2 (a) Incident angles in a scanning project. (b) Equipment for simulating different incidence angles in our experiments.

1.3.2 Calibration

In TLS, calibration of a scanner can be defined as estimation of the parameters of a deterministic model of scanner biases in order to mitigate these biases and their effect on the scanning results. So far, calibration has been concerned with the determination of instrumental errors, i.e., discrepancies between the real instrument and an ideal instrument due to mechanical imperfections (Schulz, 2008). As already mentioned, scanners can be calibrated by component

calibration or by system calibration. Figure 1.3 shows the calibration procedures. In component calibration we need to separately detect the errors in the distance and angle measurement system respectively. Moreover, instrumental error, which is caused by the behindhand manufacture, should also be detected independent in this case. Furthermore, some external factors e.g. environment should be investigated as non-instrumental error in component calibration. In system calibration, mathematical models are introduced to model the errors in scanner measurements. Parameters, which can be divided into physically interpretable and empirically interpretable elements (Lichti, 2007), are used to model and mitigate the deviations of TLS measurements are all determined together within one calibration process.

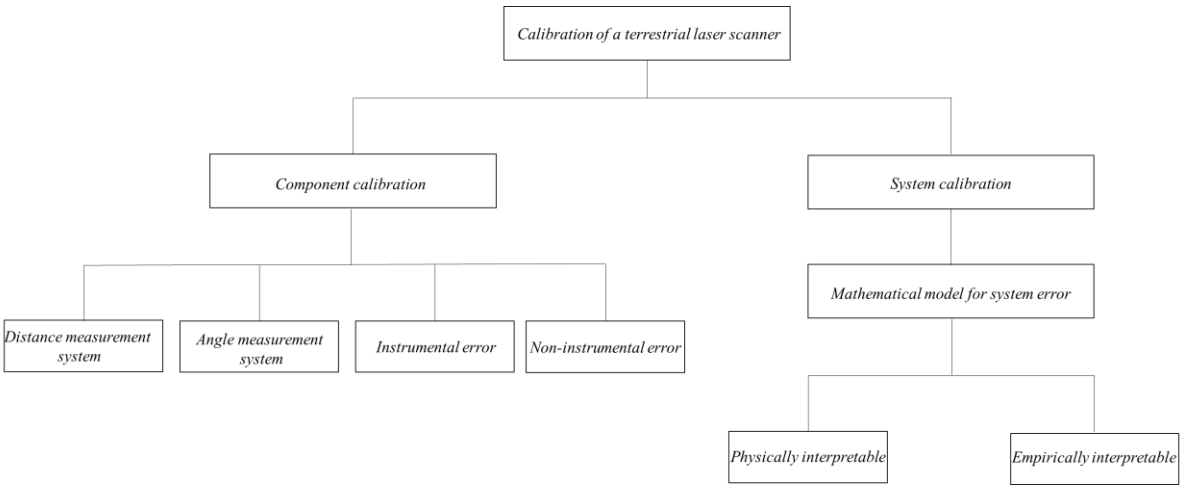

Figure 1.3 Calibration of terrestrial laser scanners.

In component calibration, precise knowledge of the individual system components and their respective error contributions is required (Schulz, 2008). However, this knowledge is often very limited owing to the proprietary design of the scanners. In addition, component calibration requires access to special facilities, such as a calibration track line, an electronic unit for frequency measurement, and stable and accurate control points, which may not be readily available to most users. More information regarding scanner calibration by means of component calibration can be found in Schulz (2008). In order to further learn about component calibration and check the accuracy of our Leica HDS 7000 laser scanner, some experiments were performed in our geo-laboratory. Figure 1.4a shows the calibration of the scanner distance measurement. The scanner was fixed on the calibration track line and a target was set up on a special base that could be moved along the track line to specific positions (see Figure 1.4b). Figure 1.4c shows a schematic diagram of this experiment.

(a) (b)

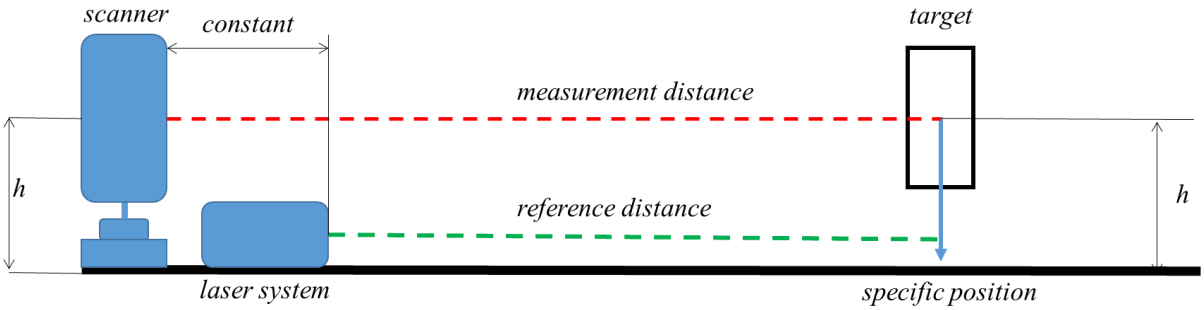

(c)

Figure 1.4 Component calibration for distance measurement. (a) Equipment for calibration of distance measurements. (b) Equipment for setting the target at a specific position. (c) Schematic diagram of the experiment.

The angular measurement system of our laser scanner was also calibrated based on component calibration in our geo-laboratory. Five targets were distributed around the scanner in a near-circular arrangement (see Figure 1.5a). In order to avoid the influence of vertical angles, all the targets were installed on pillars or tripods and approximately at the same horizon. A laser tracker target was fixed on the scanner and was used to check that the scanner was sufficiently leveled and to obtain reference values (see Figure 1.5b and 1.5c).

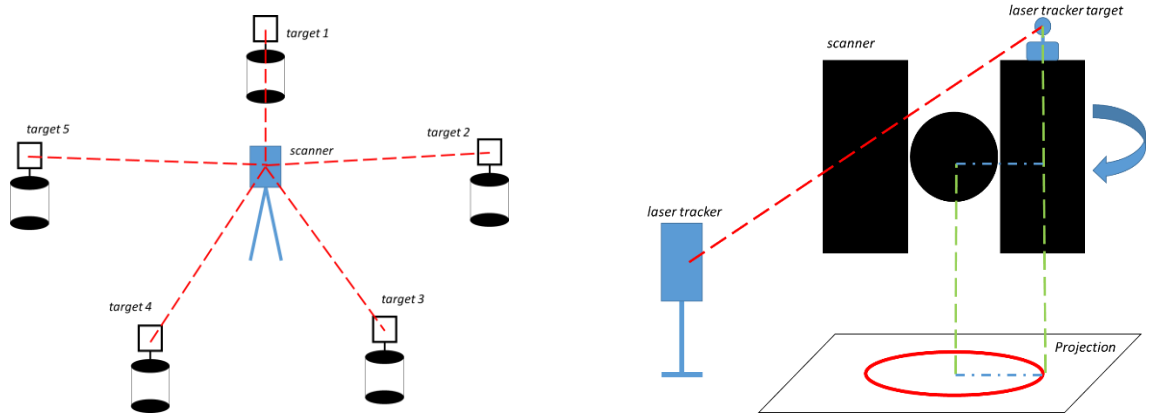

(a) *(b)*

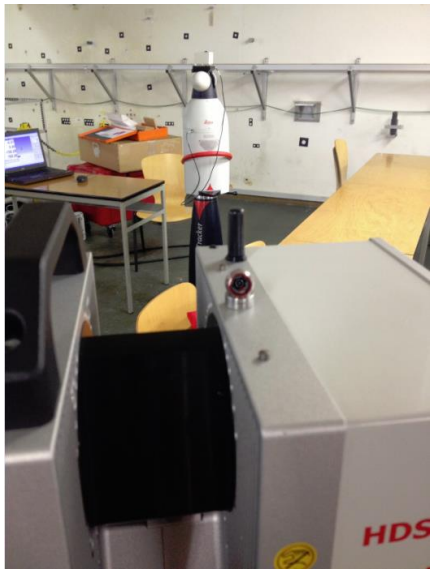

(c)

Figure 1.5 Component calibration for the angular measurements. (a) Schematic diagram of angular measurement calibration. (b) Schematic diagram illustrating how reference values were obtained using a laser tracker. (c) Equipment using a laser tracker.

In this thesis, we will focus on system calibration in chapter 4. In system calibration, the parameters used to model and mitigate the deviations of TLS measurements are all determined together within one calibration process. In contrast to component calibration, knowledge of the scanner's error model is not very important in system calibration. The error model can be established using some physical knowledge before calibration, and further corrections can be empirically derived during the calibration by a least squares adjustment. Therefore, system calibration can be exhaustively formulated so as to determine all the systematic errors of a scanner simultaneously with all the other system-related parameters. System calibration can be performed through self-calibration, and, because of its advantages (Lichti, 2007), this method has become a popular approach for TLS calibration in recent years. The problem of sensor

modeling (i.e., selection of an error model) is perhaps the most important one in TLS system calibration (Lichti and Licht, 2006). To date, most researchers have chosen the total station error model as the basis for TLS system calibration, because it operates similarly to a reflectorless total station. Thus, the most significant additional parameters (APs) are:

- zero (a_0) and scale error (a_1) of the laser rangefinder;
- collimation (b_1) and horizontal (b_2) axis errors;
- vertical circle index error (c_0).

Lichti (2007) has presented a group of synthesized error models in which the above errors are classified as physical APs because they have a definite physical interpretation. There are many other TLS error models; see, for example, Gordon and Lichti (2007), Holst and Kuhlmann (2014), and Hartzell et al. (2015). In this thesis, we base our investigation on the AP model introduced by Lichti (2007). However, we should point out that our approach can easily be applied using any other TLS error model.

Lichti and others have published a series of papers on laser scanner self-calibration, discussing correlation sources and parameter decorrelation for both panoramic and hybrid scanners. Specifically, Lichti (2007) described the self-calibration of the FARO 880 scanner. The experiments were conducted during a period of over one year. Based on those experiments, Lichti analyzed the temporal behavior of the calibration parameters, the estimated precision of unknown parameters, and the relationships among unknown parameters. Lichti (2009) compared the performances in terms of precision and correlation of a panoramic scanner and a hybrid scanner and pointed out that the inclusion of at least two orthogonal scans (i.e. $\kappa_{i+1} = \kappa_i + n * 90°, n = 1,2,3 ...$) can decorrelate the $b_1 - \kappa$ angle (the tertiary rotation angle of the scanner exterior orientation) in a panoramic scanner but not in a hybrid scanner. In the same paper, Lichti also showed the influence of vertical angles far from the horizon on both precision and correlation. Lichti (2010) discussed correlation sources and their mitigation in TLS self-calibration and showed that the inclusion of additional tilt angle observations is very important for reducing some correlations in both panoramic and hybrid scanners. Lichti et al. (2011), investigated the correlations in $b_1 - \kappa$ angle in a hybrid scanner and presented two useful methods to reduce such correlations: (i) independent observation of the κ angle and (ii) employing a modified function to remove the constant part of the model. Reshetyuk (2010) presented an approach in which all parameters of the model were additionally treated as observations with suitably chosen prior weights. This allows the inclusion of prior knowledge, reduction of correlations, and increased precision of the estimated parameters—provided that suitable prior values are available (e.g., from a previous calibration). Using certain AP models and stochastic information about the parameters of exterior orientation (EOs), Reshetyuk (2010)

succeeded in decorrelating APs and nuisance parameters even further. Here, we should point out that both the aforementioned self-calibration literature and the discussion in this thesis are concerned with point-based calibration. For plane-based calibration, interested readers can refer to Muhammad and Lacroix (2010), Glennie and Lichti (2010, 2011), Chen and Chien (2012), Gong et al. (2013), and Chan et al. (2015).

Based on earlier methods and results, we carried out system calibration in our geo-laboratory (see Figure 1.5a) and also in the Dieter-Thoma-Laboratory (see Figure 1.5b) at TUM in order to have different scales for the calibration.

(a)

(b)

Figure 1.6 System calibration field for terrestrial laser scanners. (a) Geo-laboratory; (b) Dieter-Thoma-Laboratory.

As shown in Figure 1.6a and 1.6b, the targets that were used in the calibration appear to be randomly distributed around the calibration fields. Moreover, the procedure for carrying out each scan also seems to be arbitrary. Therefore, in this thesis, we attempt to determine a configuration that will guide users to install a limited number of targets at specific positions in a calibration field, as well as providing guidance to users about how to execute scans during calibration. Users can then obtain the expected precision of the estimated APs.

1.3.3 Rigid registration

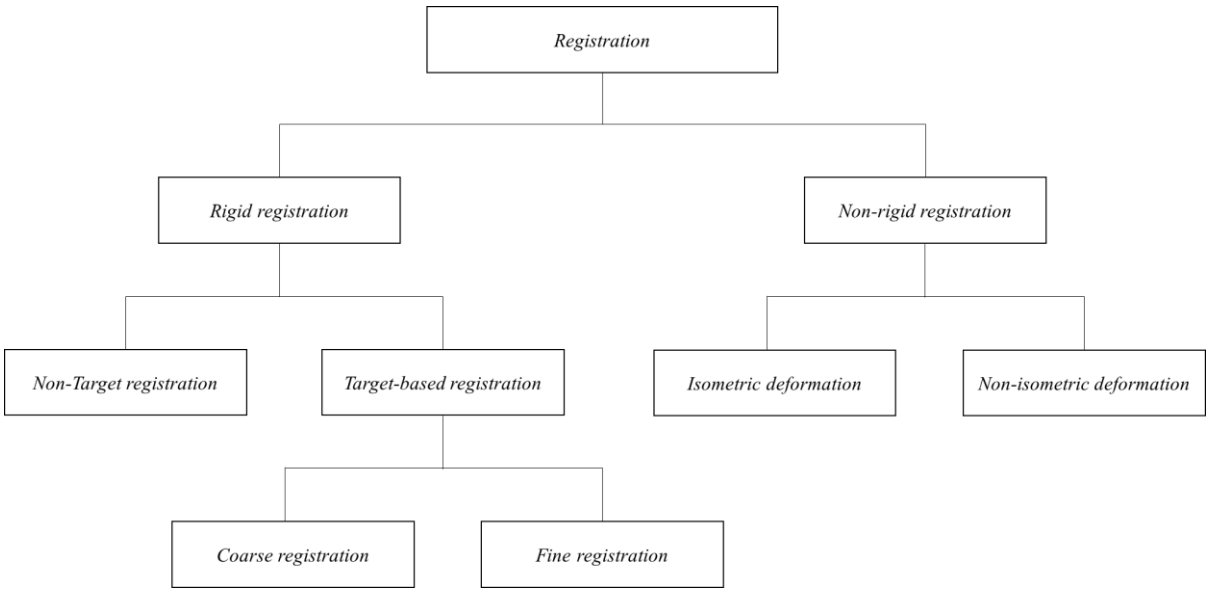

Figure 1.7 Classification of approaches to registration.

As already mentioned, the registration strategy can be divided into target-based registration and non-target registration. In target-based registration, at least three targets should appear in the area of overlap between two clouds of point sets. Based on those public targets alone, two point clouds can be aligned using calculated transformation parameters, i.e., 6 DoF (Reshetyuk, 2009). Although the advantages of target-based registration are clear (e.g., ease of computation), the negative aspects of such a strategy are also obvious. First of all, it is not always possible to distribute enough targets at ideal positions on an object's surface; second, it is not economic and is inconvenient to install so many targets and keep them stable. However, robustness is poor when there is a limited number of targets. Therefore, in this thesis, we will be most interested in non-target registration.

Figure 1.7 shows a classification of approaches to registration, from which we can see that non-target rigid registration techniques can be further classified as either coarse or fine registration, depending on whether initial information is required. In coarse registration, the main goal is to compute an initial estimate of the rigid motion between two corresponding clouds of 3D points.

Chua (1997) presented a method of searching for correspondences using a point descriptor, i.e., a point signature method. Johnson (1997) presented a method of spin images. The main problem of the latter method is that the spin image depends strongly on the resolution of the method, and therefore Carmichael et al. (1999) proposed the use of a face-based spin image to solve this problem. Chung and Lee (1998) and Kim et al. (2003) proposed a registration algorithm based on principal component analysis. Tarel et al. (1998) proposed a method to estimate the motion between surfaces represented as a polynomial model. Feldmar and Ayache (1994) described the use of the principal curvature as an invariant characteristic of a point to search for correspondences. As scanning resolutions become higher and higher, and input raw point clouds potentially consist of millions of points, recent studies of coarse registration have placed more emphasis on registration of large-scale point clouds. To deal with such issues, feature points or lines, or even planes, are usually employed to execute coarse registration. In general, point features are most commonly used for point cloud registration. Böhm and Becker (2007) explored the application of the scale-invariant feature transform (SIFT) method to the automatic marker-free registration of TLS data. Rusu et al. (2008) presented a point-feature histogram (PFH) method for estimating a set of robust 16D features describing the geometry of each point feature locally in order to determine an approximate alignment. They later proposed the use of fast point-feature histograms (FPFH) (Rusu et al. 2009). Aiger et al. (2008) introduced a four-point congruent set (4PCS) algorithm to execute coarse registration. Theiler et al. (2014) exploited 4PCS on key points extracted using a difference-of-Gaussians or Harris key point strategy. Mohammad et al. (2014, 2015) extended 4PCS to more general cases in which the four selected points no longer need to be coplanar.

In fine registration, the goal is to obtain the most accurate solution possible. After making a higher-quality initial estimate to provide an initial value, fine registration is achieved by using a sufficient overlap of the point clouds in different datasets and minimizing the sum of squares of the distance between the temporarily corresponding points in each iteration. The most popular approach to solving this problem is the iterative closest point (ICP) method (Besl and McKay, 1992; Zhang, 1994; Chen and Medioni, 1991, 1992). Although ICP is a powerful algorithm for non-target rigid registration even in the presence of Gaussian noise, it has obvious drawbacks; for example, its time efficiency is low and it can easily fall into a local minimum (Fusiello et al., 2002; Gruen and Acka, 2005; Salvi et al., 2007). Taking account of those shortcomings, some modifications of ICP have been presented. Trucco et al. (1999) used the least median of squares approach to increase the robustness of ICP. Greenspan and Godin (2001) exploited the nearest-neighbor problem to facilitate the search for closest points. Rusinkiewicz and Levoy proposed to solve the least squares problem by using a generic nonlinear method (e.g., Levenberg–Marquardt) in ICP. Jost and Hugli (2002) presented a multi-resolution scheme ICP algorithm. Sharp et al. (2002) presented an ICP method using invariant features. Zinsser et al. (2003) introduced a robust method based on outlier thresholds known as the picky ICP

algorithm. Low (2004) introduced a fast algorithm to solve fine registration, namely, linear least squares optimization for point-to-plane ICP. Another powerful approach used to complete 3D surface matching originates from the least-squares matching (LSM) technique (Gruen, 1984, 1985a; Ackermann, 1984; Pertl, 1984). Surface patch matching in photogrammetry was first resolved by Gruen (1985a) using this technique. Gruen (1985b) introduced multiple patch matching with 2D images using the LSM technique. Gruen and Acka (2005) presented a least squares 3D (LS3D) surface matching approach. Akca (2010) enhanced the LS3D approach in terms of computational cost. Grant et al. (2012) presented a point-to-plane (P2P) approach that is formulated using the general least squares adjustment model and in which the stochastic properties of both scanned points are utilized during the calculation.

Keeping the third question from Section 1.1 and the purpose of registration in mind, we developed a Gauss–Helmert least squares 3D matching approach to handle different kinds of data. The full information about observations is feasibly employed to improve the accuracy of the alignment and provides the capability of analyzing the behaviors of each kind of residual. We carried out both indoor and outdoor experiments to verify the proposed approach. Both scanning projects are concerned with close-range scanning. Two different brands of scanners (a Leica HDS7000 and a Rigel scanner) were used. Figure 1.8a shows the program for scanning a statue from two perspectives. From the figure, we can see that there exists an area of overlap between two scans (the red and blue areas represent the left and right views, respectively), which is necessary for non-target registration. Figure 1.8b shows the actual scanning scene.

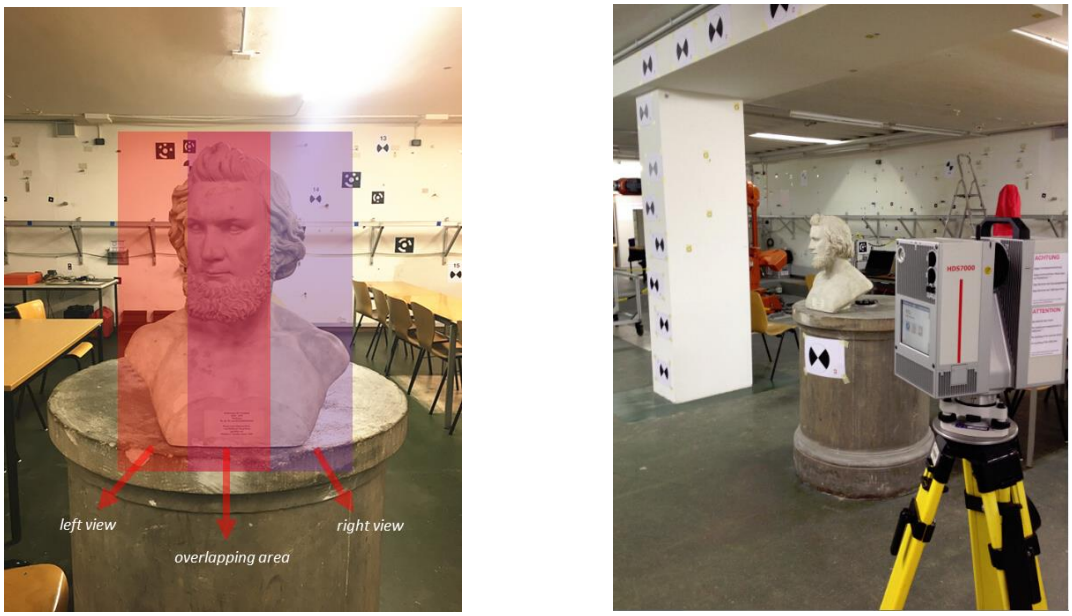

(a) *(b)*

Figure 1.8 Indoor experiment for rigid registration. (a) Scanning from two perspectives. (b) Actual scanning scene.

1.3.4 Non-rigid registration

As Figure 1.7 shows, depending on the properties of deformations, non-rigid registration can be further classified as handling either isometric or non-isometric deformation. So far, most research on non-rigid registration has focused on (approximately) isometric deformation. In the case of (approximately) isometric deformation, intrinsic geometric properties (e.g., geodesic distance and surface angle) are always employed as invariant characteristics in the search for point correspondences. The geodesic distance is one of the most frequently used intrinsic geometric properties when searching for correspondences. Berretti et al. (2006) derived a method based on iso-geodesic stripes in which a compact representation was constructed to represent these stripes and quantitatively determine their spatial relationships. Mpiperis et al. (2007) employed a geodesic polar representation in which each point on a face was characterized by the geodesic distance from the pole and by the polar angle. Jain and Zhang (2006) used a low-dimensional embedding that preserved all pairwise-geodesic distances. Bronstein et al. (2006) applied generalized multidimensional scaling to embed one mesh in another for partial matching. Huang et al. (2008) generated robust correspondences using a pruning mechanism based on geodesic consistency. In all of this work, one of the key assumptions was that the deformation was (approximately) isometric and that therefore the geodesic distance was invariant. However, one of the shortcomings of using the geodesic distance is instability, since it is more sensitive to topological relationships. Furthermore, this latter influence will be particularly evident in the TLS technique. As the data of point clouds are discrete, we usually need to generate a triangulation mesh on the scanned object using discrete coordinates. Thus, the quality of the triangulation mesh will directly influence the topological relationship; moreover, this quality depends not only on the triangulation algorithm but also on the quality of the point clouds. Pauly et al. (2005) and Bronstein et al. (2008) proposed to use landmarks to alleviate stability problems. Ovsjanikov et al. (2010) described the use of a heat kernel to find geometric feature points and generate correspondences from a single isometric matching. Tevs et al. (2009) described a method for overcoming the influence of topological noise. Bronstein et al. (2010) proposed the use of the diffusion and Gromov–Hausdorff distances to handle this problem. Smeets et al. (2012) exploited the geodesic distance matrix as an isometry-invariant shape representation in a method that did not need explicit point correspondences for the comparison of 3D shapes, thereby avoiding contamination by topological noise. After correspondences have been generated, different strategies can be adopted to align the target point cloud with the source point cloud and achieve an optimized result. Chang and Zwicker (2008) segmented the whole point cloud into different rigid sub-parts and then executed a rigid-body transformation between two rigid clusters from target point cloud to source point cloud. Huang et al. (2008) adopted a forward search method (Fleishman

et al. 2005) to iteratively combine neighboring clusters until a quality threshold was reached, after which they carried out a rigid-body transformation and achieved an energy optimization. Zhang et al. (2008) formulated potential correspondences in a tree and performed a global optimal tree search. Based on this method, natural correspondences can be obtained. Yemez (2012) used an expectation maximization approach to estimate shape correspondences. Tam et al. (2013) presented a comprehensive survey of both rigid and non-rigid registration, describing developments in both approaches and pointing out the differences and connections between them. The use of TLS in cases with deformation is currently attracting a great deal of interest. So far, most research on this topic has focused on detecting the deformation using TLS (e.g., Pesci et al., 2013) and comparing the results with a given template, for example with digital elevation models (DEMs) (Bitelli et al., 2004) or with a cylinder parameterization model (Van Gosliga et al., 2006). Monserrat and Crosetto (2007) presented a rigid surface registration method to detect deformation and further to give transformation information, including the three translation distances and three rotation angles. However, in their cases, the deformation was always a rigid-body transformation. Although there are limitations to their approach, it does reveal the potential for using a registration approach to represent deformation.

Taking account of earlier approaches and our requirements, we investigated isometric deformation cases using non-rigid registration. We extended the concept of the four-point congruent set (4PCS) algorithm from rigid to non-rigid cases by using geodesic distances instead of Euclidean distances in order to obtain an invariance property. After generating correspondences between two corresponding point clouds, a consistency sampling approach was adopted to identify and transform rigid subsets. TOSCA high-resolution datasets were used in the experiments to verify the proposed approach. Figure 1.9 shows some sample datasets from TOSCA (Bronstein et al., 2008) that have true correspondence information.

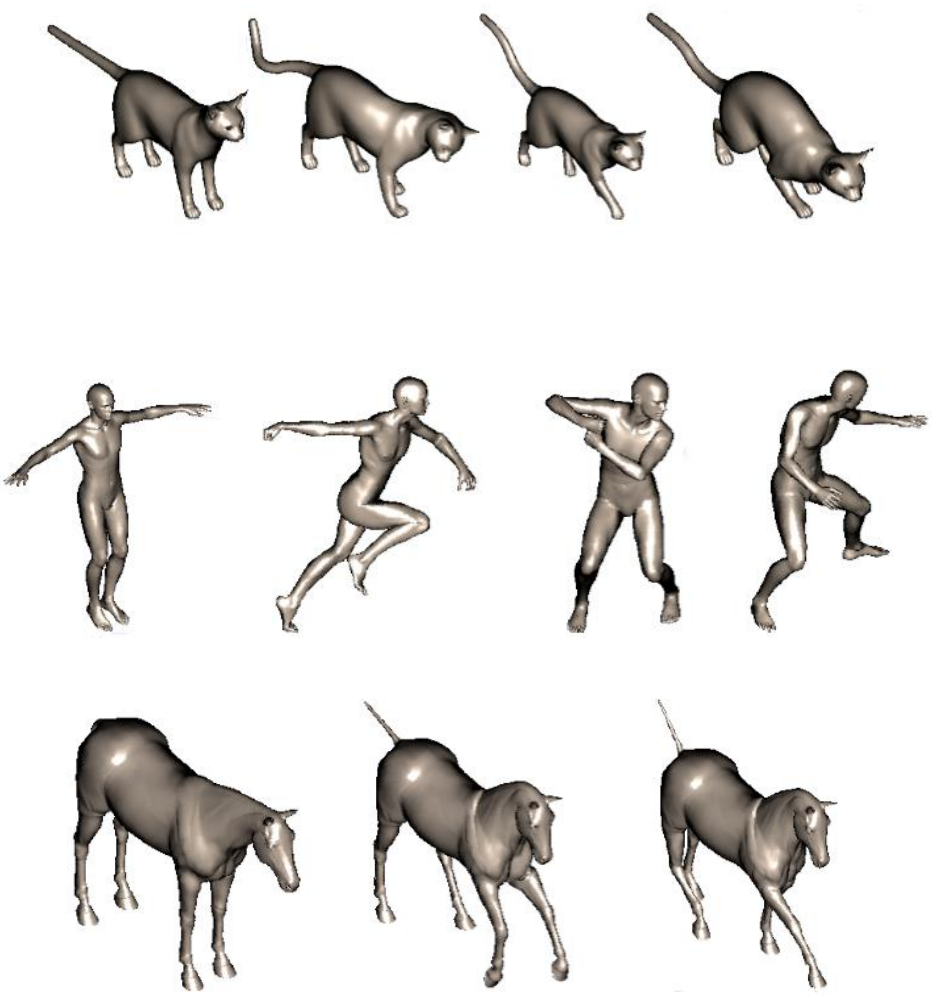

Figure 1.9 Three samples of TOSCA high-resolution datasets for non-rigid registration.

Real scanning experiments were also performed to verify the proposed method in the geo-laboratory. Figure 1.10a shows the equipment for a curved surface experiment and Figure 1.10b shows the surface point clouds that were captured from different epochs. On the curved surface, we marked 143 reference points (see Figure 1.11) to detect the deformation of the surface at different epochs. These reference points were measured by a Leica MS50 total station (with accuracies of 1 mm and 0.5″ for distance and angular measurements, respectively) at different epochs, and the values thus determined were employed as the "true" values to verify the proposed method using TLS with a Leica HDS 7000 scanner. It should be pointed out here that when using the laser scanner to measure the curved surface, it was not possible to extract the coordinates of a specific reference point and then compare its positions at the first and second epochs, as was done with the total station. It was first necessary to obtain different rigid clusters, find the corresponding clusters for each reference point, and then represent the deformation of the reference points by the deformation of the corresponding clusters. As already mentioned, we represent deformation using real 3D information, i.e., 3D translations and 3 rotation angles,

and therefore, in order to compare the results with those obtained using the total station, we presented the deformation in a uniform manner as follows. $(x,y,z)_{i,j}^{T}$ represents the *i*th reference point in the total station system at the *j*th epoch and $(x,y,z)_{i,j+1}^{T}$ is the same point at the (j+1)th epoch. The deformation for this point in the total station system can then be expressed as the Euclidean distance:

$$d_{i,(j,j+1)}^{T} = \left\|(x,y,z)_{i,j}^{T} - (x,y,z)_{i,j+1}^{T}\right\|. \tag{1.1}$$

For the same specific reference point in the scanner system, the deformation is obtained as $R_{i,(j,j+1)}$ and $T_{i,(j,j+1)}$. This transformation parameter is then used to obtain a virtual point by transforming the reference point in the total station system at the *j*th epoch:

$$(x,y,z)_{i,j+1}^{V} = R_{i,(j,j+1)} \cdot (x,y,z)_{i,j}^{T} + T_{i,(j,j+1)} \tag{1.2}$$

where $(x,y,z)_{i,j+1}^{V}$ is a virtual point. The deformation of the *i*th reference point between the *j*th and (j+1)th epochs in the laser scanner system can then be expressed using the total station form:

$$d_{i,(j,j+1)}^{V} = \left\|(x,y,z)_{i,j}^{T} - (x,y,z)_{i,j+1}^{V}\right\|. \tag{1.3}$$

All data sets were transformed into a same coordinate system before the deformation calculations. We assumed that there is no error in the measurements such that the TPS measured reference points in the *j*th epoch should fall into the TLS scanned curved surface at the same epoch. Obviously, such hypothesis is not work so we can calculate the perpendicular projection distances from each point to the scanned curved surface at the same epoch. Therefore, those distances can be seem as the measurements errors of the scanner so as to reflect the actual measurement accuracy of the using scanner. Figure 1.12 shows above distances of each reference point at the epoch 1 (before deformation) and the epoch 2 (after deformation). From figure 1.12 we can see that the using scanner has approximately 3 mm systematic error and the actual measurement accuracy is about $\pm$1 mm. Figure 1.13 shows the deformations from the laser scanner in terms of coordinate components: $(\Delta x, \Delta y, \Delta z)_{i,j+1} = (x,y,z)_{i,j+1}^{V} - (x,y,z)_{i,j+1}^{T}$. Finally, the point error for each reference point can be obtained as (see Figure 1.14)

$$e_{i,(j,j+1)} = \sqrt{\Delta x^2 + \Delta y^2 + \Delta z^2}. \tag{1.4}$$

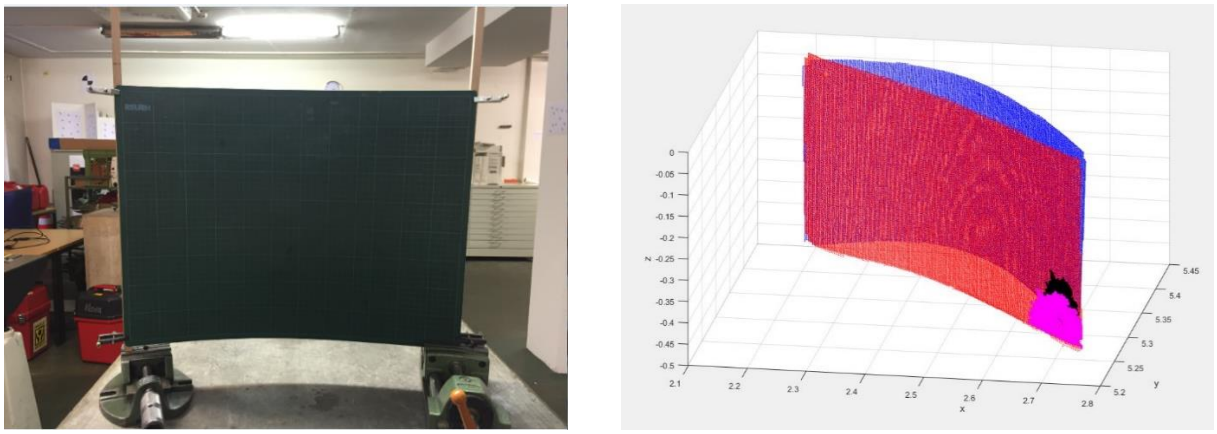

(a) *(b)*

Figure 1.10 (a) Scanned curved surface. (b) Point clouds from two epochs.

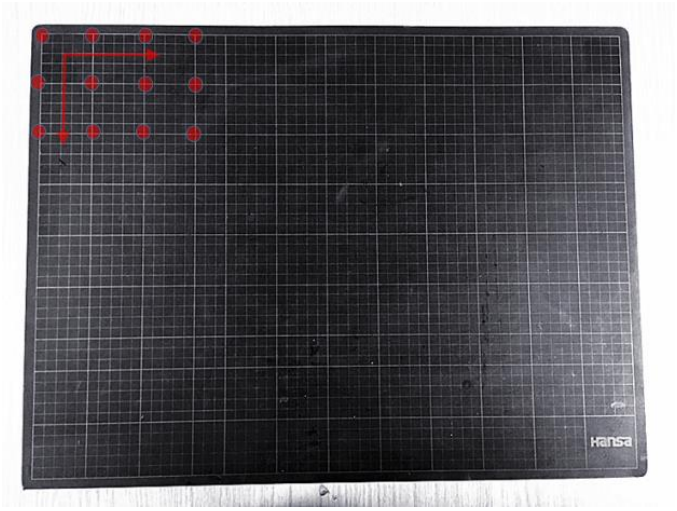

Figure 1.11 Reference points (red points) on the curved surface.

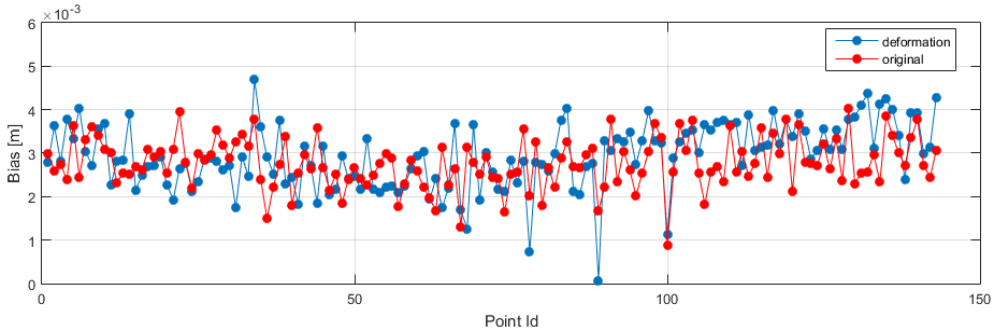

Figure 1.12 The perpendicular projection distances from each reference point to the corresponding scanned curved surface so as to reflect the actual measurement accuracy of the using scanner. The red and blue points reflect the results before and after deformation respectively.

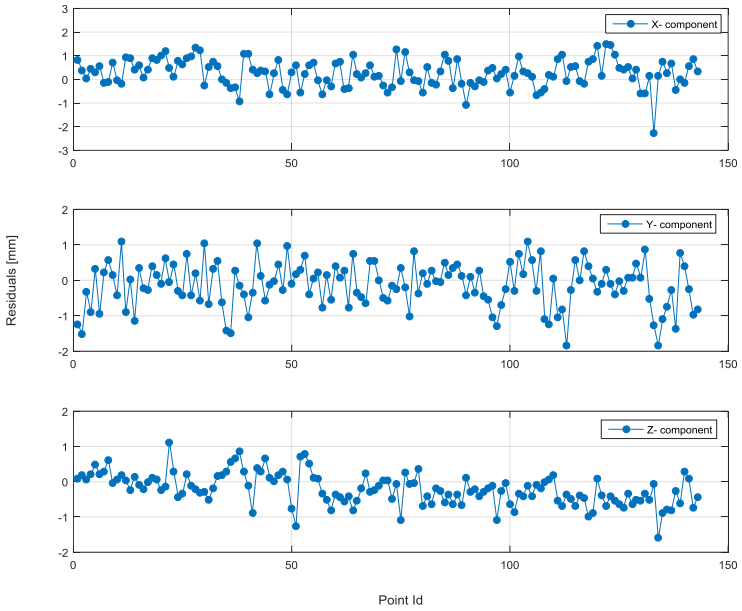

Figure 1.13 Deformation from the laser scanner in terms of the coordinate components. To compare each reference points that were measured by the TPS in the deformed epoch with corresponding virtual points that were calculated with the transformation parameters from the results of deformation by the TLS in each coordinate components.

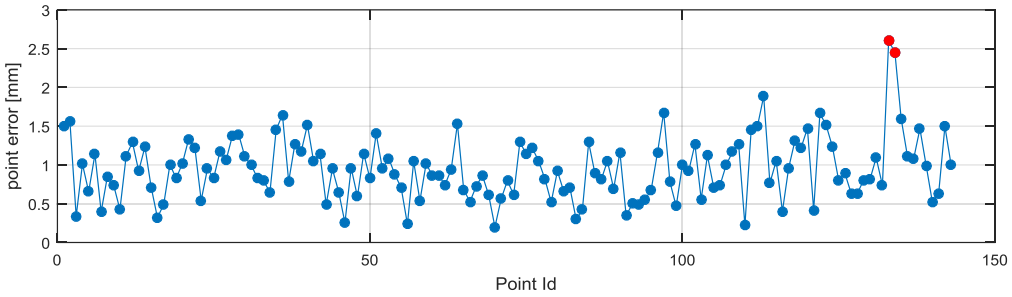

Figure 1.14 Point error: comparison of laser scanner results with total station results. The point errors reflect the Euclidean distances between the TPS measured positions and their corresponding calculated positions by the TLS in the deformed epoch.

Chapter 2

Background

In this chapter, we briefly introduce the main tools that we build upon in the coming chapters.

2.1 Weighted total least square

The least squares method, developed by C.F. Gauss, has been applied to estimate model parameters for the Gauss-Markov model, i.e.

$$\mathbf{A}\cdot\mathbf{x}=\mathbf{y}+\mathbf{e}_{\mathbf{y}} \tag{2.1}$$

where $\mathbf{A}$ represents the $n \times m$ coefficient matrix, $\mathbf{y}$ is $n \times 1$ observation vector affected by the random error vector $\mathbf{e}_{\mathbf{y}}$, and $\mathbf{x}$ is the (unknown) $m \times 1$ parameter vector. In Eq. (2.1) a hypothesis should hold i.e. the coefficient matrix $\mathbf{A}$ is error free. However, the principal hypothesis of a certain coefficient matrix $\mathbf{A}$ in the Gauss-Markov model is not necessarily fulfilled for all applications. From a geodetic perspective, a Gauss-Markov models with an uncertain coefficient matrix $\mathbf{A}$ is known as a standard errors-in-variables model (Fuller, 1987). Then the relationship in Eq. (2.1) can be redefined as

$$\left(\mathbf{A}+\mathbf{E}_{\mathbf{A}}\right)\cdot\mathbf{x}=\mathbf{y}+\mathbf{e}_{\mathbf{y}} \tag{2.2}$$

where the coefficient matrix $\mathbf{A}$ is affected by the random error matrix $\mathbf{E}_{\mathbf{A}}$. Least squares within the errors-in-variables model is usually called the total least squares technique (Van Huffel and Vandewalle, 1991; Schaffrin and Wieser, 2008) because of its symmetrical adjustment. From the geodetic tradition view, we called "weight" to express the quality of observations and is based on element-wise definition of variances and co-variances. The stochastic properties of the errors in Eq. (2.2) be characterized by

$$\begin{bmatrix}\mathbf{e}_{\mathbf{y}}\\ \mathbf{e}_{\mathbf{A}}\end{bmatrix}:=\begin{bmatrix}\mathbf{e}_{\mathbf{y}}\\ \mathrm{vec}(\mathbf{E}_{\mathbf{A}})\end{bmatrix}\sim\left(\begin{bmatrix}0\\ 0\end{bmatrix},\quad \sigma_0^2\begin{bmatrix}\mathbf{Q}_{\mathbf{y}} & \mathbf{0}\\ \mathbf{0} & \mathbf{Q}_{\mathbf{A}}\end{bmatrix}\right) \tag{2.3}$$

where "vec" denotes the operator that stacks one column of a matrix underneath the previous one. σ_0^2 denote an (unknown) variance component. $\mathbf{Q}_{\mathbf{A}}$ and $\mathbf{Q}_{\mathbf{y}}$ are the symmetric and non-

negative-defined cofactor matrices of $\mathbf{e_A}$ and $\mathbf{e_y}$ respectively and $\mathbf{P_A}$ and $\mathbf{P_y}$ are corresponding weight matrices. The weighted total least squares problem is expressed as the constrained optimization problem

$$\begin{aligned} &\mathbf{e}_\mathbf{y}^T\mathbf{P}_\mathbf{y}\mathbf{e}_\mathbf{y} + \mathbf{e}_\mathbf{A}^T\mathbf{P}_\mathbf{A}\mathbf{e}_\mathbf{A} = \min \\ &\textit{subject to} \quad \left(\mathbf{A}+\mathbf{E}_\mathbf{A}\right)\cdot\mathbf{x} = \mathbf{y}+\mathbf{e}_\mathbf{y}. \end{aligned} \tag{2.4}$$

The constrained optimization problem (2.4) is typically solved using Lagrange multipliers. The target function as follows:

$$\Phi\left(\mathbf{e}_\mathbf{y}, \mathbf{e}_\mathbf{A}, \mathbf{x}, \lambda\right) = \mathbf{e}_\mathbf{y}^T\mathbf{P}_\mathbf{y}\mathbf{e}_\mathbf{y} + \mathbf{e}_\mathbf{A}^T\mathbf{P}_\mathbf{A}\mathbf{e}_\mathbf{A} + 2\boldsymbol{\lambda}^T\left(\mathbf{A}\cdot\mathbf{x} + \mathbf{E}_\mathbf{A}\cdot\mathbf{x} - \mathbf{y} - \mathbf{e}_\mathbf{y}\right) = \min \tag{2.5}$$

with $\boldsymbol{\lambda}$ as the Lagrange multiplier vector. The normal approach to solve Eq. (2.5) is to set the partial derivatives of the target function w.r.t $\mathbf{e}_\mathbf{y}, \mathbf{e}_\mathbf{A}, \mathbf{x}, \lambda$ to $\mathbf{0}$ i.e.

$$\left.\frac{\partial\Phi}{\partial\mathbf{x}}\right|_{\hat{\mathbf{x}},\hat{\mathbf{e}}_\mathbf{y},\hat{\mathbf{e}}_\mathbf{A},\hat{\lambda}} = \mathbf{0}, \left.\frac{\partial\Phi}{\partial\boldsymbol{\lambda}}\right|_{\hat{\mathbf{x}},\hat{\mathbf{e}}_\mathbf{y},\hat{\mathbf{e}}_\mathbf{A},\hat{\lambda}} = \mathbf{0},$$

$$\left.\frac{\partial\Phi}{\partial\mathbf{e}_\mathbf{y}}\right|_{\hat{\mathbf{x}},\hat{\mathbf{e}}_\mathbf{y},\hat{\mathbf{e}}_\mathbf{A},\hat{\lambda}} = \mathbf{0}, \left.\frac{\partial\Phi}{\partial\mathbf{e}_\mathbf{A}}\right|_{\hat{\mathbf{x}},\hat{\mathbf{e}}_\mathbf{y},\hat{\mathbf{e}}_\mathbf{A},\hat{\lambda}} = \mathbf{0}.$$

then

$$\hat{\mathbf{x}}^{(\mathrm{i}+1)} = \left(\mathbf{A}^T\left(\mathbf{P}_\mathbf{y}^{-1} + \left(\hat{\mathbf{x}}^{(i)^T}\mathbf{P}_0^{-1}\hat{\mathbf{x}}^{(i)}\right)\mathbf{P}_\mathbf{x}^{-1}\right)^{-1}\mathbf{A} - \hat{\boldsymbol{\upsilon}}^{(\mathrm{i})}\mathbf{P}_0^{-1}\right)^{-1}\mathbf{A}^T\left(\mathbf{P}_\mathbf{y}^{-1} + \left(\hat{\mathbf{x}}^{(\mathrm{i})^T}\mathbf{P}_0^{-1}\hat{\mathbf{x}}^{(\mathrm{i})}\right)\mathbf{P}_\mathbf{x}^{-1}\right)^{-1}\mathbf{y} \tag{2.6}$$

with

$$\boldsymbol{\lambda}^{(\mathrm{i})} = \left(\mathbf{P}_\mathbf{y}^{-1} + \left(\hat{\mathbf{x}}^{(\mathrm{i})^T}\mathbf{P}_0^{-1}\hat{\mathbf{x}}^{(\mathrm{i})}\right)\mathbf{P}_\mathbf{x}^{-1}\right)^{-1}(\mathbf{y} - \mathbf{A})\hat{\mathbf{x}}^{(\mathrm{i})}$$

$$\hat{\boldsymbol{\upsilon}}^{(\mathrm{i})} = \boldsymbol{\lambda}^{(\mathrm{i})^T}\mathbf{P}_\mathbf{x}^{-1}\boldsymbol{\lambda}^{(\mathrm{i})}$$

$$\mathbf{P}_\mathbf{A} = \mathbf{P}_\mathbf{0} \otimes \mathbf{P}_\mathbf{X}$$

$\mathbf{P}_0$ and $\mathbf{P}_X$ represent the column vector's weight matrix and the row vector's weight matrix of the design matrix, respectively. More detailed and complete derivations can be found in Schaffrin and Wieser (2008), Shen et al. (2010), Mahboub (2012), Snow (2012) and Fang (2013).

2.2 Gauss-Helmert model

The iteratively linearized Gauss-Helmert model method proposed by Pope (1972) was used to adjust the errors-in-variables model by least squares (Neitzel, 2010). The nonlinear Gauss-Helmert model has also been applied to the total least squares field (Neitzel, 2010; Schaffrin and Snow, 2010). In this case, all the observations are considered, namely, the coefficient matrix **A** is also affected by the random errors. The nonlinear model $\mathbf{f}(\mathbf{e},\mathbf{x}) = \mathbf{0}$ is linearized through the truncated Taylor series

$$\mathbf{f}(\mathbf{e},\mathbf{x}) \approx \mathbf{f}(\mathbf{e}_0,\mathbf{x}_0) + \left.\frac{\partial \mathbf{f}}{\partial \mathbf{x}^T}\right|_{\mathbf{x}_0,\mathbf{e}_0} \left(\mathbf{x}-\mathbf{x}_0\right) + \left.\frac{\partial \mathbf{f}}{\partial \mathbf{e}^T}\right|_{\mathbf{x}_0,\mathbf{e}_0} \left(\mathbf{e}-\mathbf{e}_0\right) = \mathbf{0} \tag{2.7}$$

with

$$\left.\frac{\partial \mathbf{f}}{\partial \mathbf{x}^T}\right|_{\mathbf{x}_0,\mathbf{e}_0} =: \mathbf{A}_0, \left.\frac{\partial \mathbf{f}}{\partial \mathbf{e}^T}\right|_{\mathbf{x}_0,\mathbf{e}_0} =: \mathbf{B}_0 \tag{2.8}$$

where **x** is also the (unknown) $m \times 1$ parameter vector and the observations affected by the random error vector **e**. In the nonlinear Gauss-Helmert model, appropriate initial values are needed to execute an iteration. Based on Eq. (2.7), iterate by setting for i+1th iteration:

$$\begin{aligned} \mathbf{x}_0^{i+1} &:= \hat{\mathbf{x}}^i := \mathbf{x}_0^i + d\hat{\mathbf{x}}^i \\ \mathbf{e}_0^{i+1} &:= \hat{\mathbf{e}}^i \end{aligned} \tag{2.9}$$

and then estimating $d\hat{\mathbf{x}}^i$, $\hat{\mathbf{e}}^i$ from the following Lagrange multipliers formulation

$$\Phi(d\mathbf{x},\mathbf{e},\boldsymbol{\lambda}) := \mathbf{e}^T\mathbf{P}\mathbf{e} + 2\boldsymbol{\lambda}^T\left(\mathbf{A}^i \cdot d\mathbf{x} + \mathbf{B}^i \cdot \mathbf{e} + \mathbf{f}(\mathbf{x}_0^i,\mathbf{e}_0^i) - \mathbf{B}^i\mathbf{e}_0^i\right) = \min \tag{2.10}$$

with

$$\mathbf{A}_i := \left.\frac{\partial \mathbf{f}}{\partial \mathbf{x}^T}\right|_{\mathbf{x}_0^i,\mathbf{e}_0^i}, \mathbf{B}_i := \left.\frac{\partial \mathbf{f}}{\partial \mathbf{e}^T}\right|_{\mathbf{x}_0^i,\mathbf{e}_0^i}$$

and

$$\mathbf{f}(\mathbf{x}_0^i,\mathbf{e}_0^i) - \mathbf{B}^i\mathbf{e}_0^i := \mathbf{w}_i$$

then the solution for the unknowns is obtained from the equation system

$$\begin{bmatrix} \mathbf{B}^i\mathbf{P}^{-1}\mathbf{B}^{i^T} & \mathbf{A}_i \\ \mathbf{A}_i^T & 0 \end{bmatrix} \begin{bmatrix} \hat{\lambda}^{i+1} \\ \hat{\mathbf{x}}^{i+1} - \hat{\mathbf{x}}^i \end{bmatrix} + \begin{bmatrix} \mathbf{w}^i \\ 0 \end{bmatrix} = \mathbf{0} \tag{2.11}$$

where **P** in Eq. (10) represents the weight matrix and $\boldsymbol{w}_i$ is the vector of misclosures. More detailed and complete derivations can be found in Lenzmann and Lenzmann (2004, 2007), Schaffrin and Snow (2010), Snow (2012) and Fang (2013).

2.3 Intensity of laser beam

The intensity of the reflected laser beam is one of the important inherent properties for all terrestrial laser scanners and can be gained with 3D coordinates simultaneously. Thus, the intensity information is always employed into TLS projects to act (Pseudo) 4 dimension information. The information of intensity of laser beam is important since the amplitude of the received signal is correlated with the quality of the detected range. The intensity (*I*) is influenced by three parameters:

- the range $d(I \sim \frac{1}{d^2})$,
- the reflectivity of the object, and
- the angle of incidence.

Wunderlich et al., (2013) executed tests to investigate the factors (including the distance, the color and the angle of incidence) that will influence the intensity of laser beam in Chair of Geodesy's laboratory at Technische Universität München. The testing specimen is a 60×80 cm flake board which has been coated with a dim white and therefore is diffusively dispersive surface. It is furthermore subdivided in individual testing areas for special testing parameters (Figure 2.1). The different sizes of boards are displayed in Figure 2.1. The top three boards with the same color (dim white) are used to test the influence of the angle of incidence (from left to right: $45°, 30°, 15°$). In the main board, three individual areas were printed with different colors (black RGB 16/16/15, gray RGB 162/162/160 and white RGB 220/224/223). The tests were carried out with different distances (i.e. 20 m and 100 m) by using different scanners (i.e. Focus^{3D}, Leica HDS7000 and Leica Scan Station P20). The results can be found in Figure 2.2.

From Figure 2.2 we can see that although the intensity values will be changed dependent on different distances and different brands of scanners, the different properties (the color and the angle of incidence) can also be separated in each specific situation with the intensity values. This good characteristic gives us a great potential to utilize the information of intensity of laser beam.

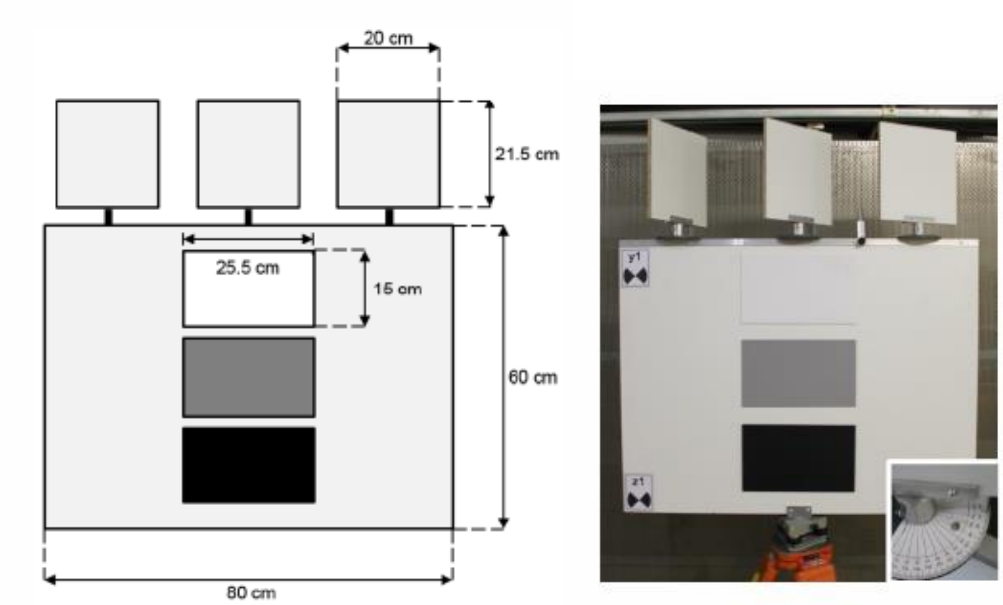

Figure 2.1 Specimen “Board” to test the intensity of laser beam (Wunderlich et al. 2013).

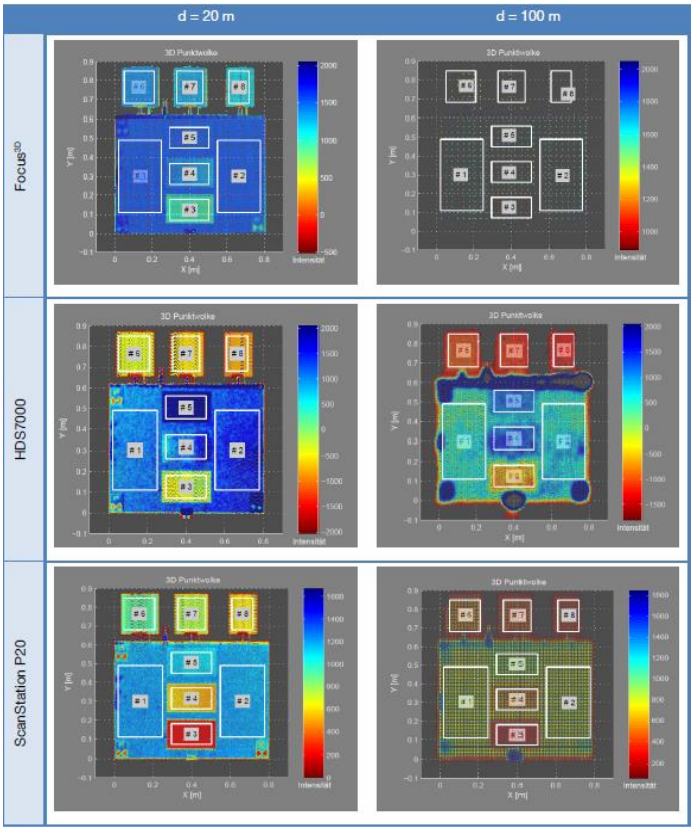

Figure 2.2 Point clouds on the “board” specimen with different intensities. Different scanners: 1st row: Focus3D, 2nd row: Leica HDS7000, 3rd row: Scan Station P20. Different measurement distances: 1st col: 20 m, 2nd col: 100 m. (Wunderlich et al. 2013).

2.4 An additional parameters model for laser scanner systematic error calibration

One of the main advantages of system calibration is that precise knowledge of the individual system components and their respective error contributions is no longer required, but instead of a deterministic model of the deviations of distance and angle measurements. In this thesis, we execute our research based on the Lichti's (2007) presented APs models which contain both the physical interpretation errors and empirical errors. The full error models as follows:

$$\begin{aligned}\delta\rho &= a_0 + a_1\rho + a_2\sin(\alpha) \\ &+ a_3\sin\left(\frac{4\pi}{U_1}\rho\right) + a_4\cos\left(\frac{4\pi}{U_1}\rho\right) + a_5\sin\left(\frac{4\pi}{U_2}\rho\right) + a_6\cos\left(\frac{4\pi}{U_2}\rho\right) \\ &+ a_7\sin(4\theta) + a_8\cos(4\theta)\end{aligned}$$

$$\delta\theta = b_1\sec(\alpha) + b_2\tan(\alpha) + b_3\sin(2\theta) + b_4\cos(2\theta) + b_5\theta + b_6\cos(3\theta) + b_7\sin(4\theta)$$

$$\delta\alpha = c_0 + c_1\alpha + c_2\sin(\alpha) + c_3\sin(3\alpha) + c_4\cos(3\alpha) \tag{2.12}$$

where ρ is the measured distance, θ is the measured horizontal angle and α is the measured vertical angle. The a_i, b_i and c_i are the parameters of the model i.e., the APs, whereas the U_i are the first (finest) and second modulation wavelength of the distance measurement unit. a_0 is the zero error (or called additive constant). Because the virtual electro-optical origin or zero of an electronic distance measurement instrument is usually not located on the vertical axis of the instrument, a small correction has to be added to all distance measurements to refer the distance to the instrument's vertical axis. a_1 is the scale error of the laser rangefinder. The scale error for an instrument may depend both on internal and external effects. The former one include the oscillator and diode errors and the external effects have the velocity of light, humidity, temperature, pressure and so on. b_1 is the collimation axis error, the non-orthogonality between the instrument's collimation and horizontal axes. b_2 is the horizontal axis error, the non-orthogonality between the scanner's horizontal and vertical axes. c_0 is the vertical circle index error, which models the constant offset between the scanner-space horizontal plane and the elevation-angle measurement origin. The subset of APs model i.e. (a_0, a_1, b_1, b_2 and c_0) can be regarded as physical APs, since they have definite physical interpretation and are typically the most significant ones (Lichti and Licht, 2006). It is possible to analyze the observation residuals after a system calibration based on above mentioned APs subset in order to verify there is no systematic trends present in the residuals. Those systematic trends can be called empirical errors (Lichti 2007) and be simulated by a mathematic model. There are two methods to execute a calibration with such APs models. The first is directly to use the full error model to calculate

and subsequently do the *t-test* for each AP to check the significant property. Then we re-select the AP elements who have 95% significance in the *t-test* to generate a subset to do a system calibration again. The second method is only to use the physical interpretation subset and subsequently analyze the residuals whether they contain systematic trends and then to further exploit some empirical elements. Table 2.1-2.3 show more details about the Lichti's (2007) APs models.

Table 2.1 APs component in range.

Parameters	**Explanation**	**Physical**	**Empirical**
a_0	The zero error in the range finder.	x	
a_1	The scale error in the range finder.	x	
a_2	The sinusoidal error in range has a 360o period and is hypothesized to be due to a vertical offset between the laser and horizontal axis.	x	
a_3 & a_4	The first-order periodic error terms inherent to AM-CW rangefinder system.	x	
a_5 & a_6	The second-order periodic error terms inherent to AM-CW rangefinder system.	x	
a_7 & a_8	The sinusoidal error in range as a function of horizontal direction with period 90o, for which the physical cause is not known.		x

Table 2.2 APs component in horizontal direction.

Parameters	Explanation	Physical	Empirical
b_1	The collimation axis error.	x	
b_2	The horizontal axis error.	x	
b_3 & b_4	The non-orthogonality of the plane containing the horizontal angle encoder and the vertical axis causes a sinusoidal error with period 180^o.	x	
b_5	The scale factor in the horizontal direction.	x	
b_6 & b_7	Residual errors in horizontal direction as a function of elevation angle that are not corrected by the collimation axis and horizontal axis models.		x

Table 2.3 APs component in vertical direction.

Parameters	Explanation	Physical	Empirical
c_0	The vertical circle index error.	x	
c_1	Scale in vertical direction.	x	
c_2	A sinusoidal error in vertical angle with a period of 360^o, which suggests circle eccentricity error.	x	
c_3 & c_4	A sinusoidal error as a function of horizontal direction with period of 120^o.		x

2.5 Correspondences

To generate stable correspondences between the source and target point clouds is a crucial step in all registration strategies (both in rigid and non-rigid cases). Incorrect correspondences easily trap the registration in local minima. As we discussed above, there are three popular methods to search corresponding points namely point-to-point, point-to-plane and point-to-projection. Figure 2.3 respective shows these three approaches.

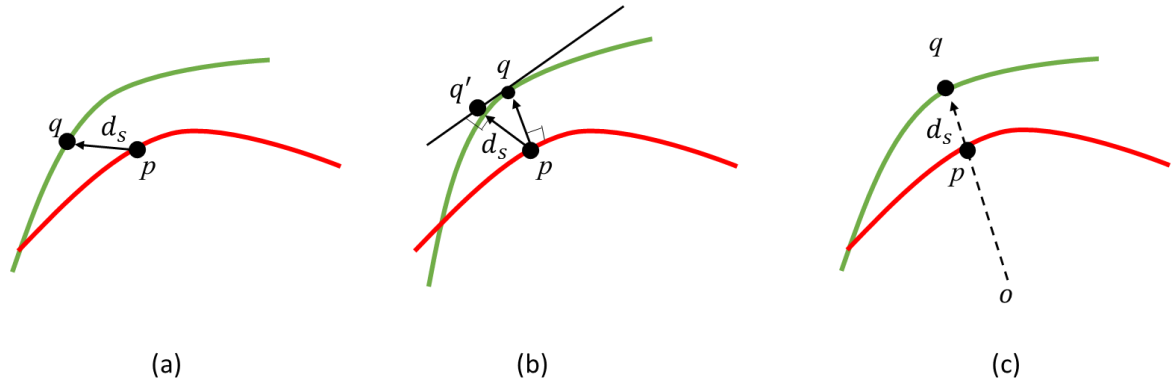

Figure 2.3 Three common techniques to generate correspondences. (a) point-to-point (b) point-to-plane (c) point-to-projection

Figure 2.3 (a) shows the principle of point-to-point strategy which is most common method to search corresponding points from target (**T**) to source (**S**) point clouds. An error metric d_s is the distance between two corresponding points. The idea in the point-to-point strategy is simple namely select a point p from **T** and to find a nearest point q from **S**, i.e. assure $d_s = \min$, and then to store a correspondence (p, q). Figure 2.3 (b) displays the point-to-plane approach. It searches the intersection on the destination surface from the normal vector of the source point. As shown in Figure 2.3 (b), the intersection point q' is the projection of p onto the tangent plane at q which is the intersection from the normal of p. Figure 2.3 (c) gives the idea of point-to-projection. This approach determines a point q which is the conjugate of a source point p, by forward-projecting p from the point of view of the destination o. Many strategies have been presented to improve the robustness of the generated correspondences, e.g.

$$\gamma = \frac{\sqrt{\sum_{i=1}^{N} \left(d_s^i\right)^2}}{N} \tag{2.13}$$

and to assure

$$d_s^i \leq 2.5 \cdot \gamma. \tag{2.14}$$

If one of d_s cannot satisfy the Eq. (2.14) then such correspondence will be removed from the correspondence subset. Moreover, after obtaining all the satisfied correspondences, we can employ a Gauss core to weight those correspondences in terms of d_s i.e.

$$W_i = \exp(-\frac{(\alpha \cdot d_s)^2}{2\sigma^2}) \tag{2.15}$$

where α is a significance factor.

In non-rigid cases, the aforementioned methods cannot be directly used to generate correspondences since the deformations may change the relationships between point to point e.g. the Euclidean distance, see Figure 2.4. Generally, another kind of invariant characteristics should be added to generate stable correspondences at deformed areas. This topic will be discussed in detail in chapter 6.

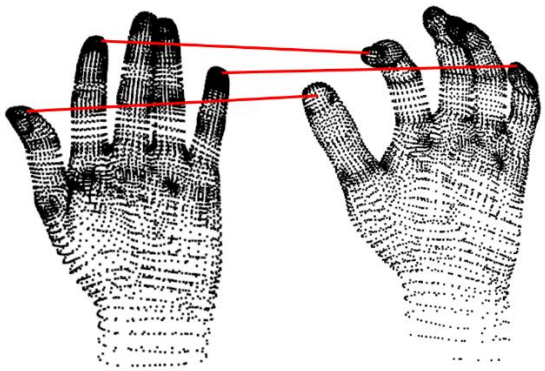

Figure 2.4 An example to find correspondences in a non-rigid case (TOSCA high-resolution dataset, Bronstein et al., 2008).

2.6 Iterative closest point (ICP) algorithm

The ICP algorithm is one of the common techniques for fine registration of 3D surfaces (or models). ICP starts with two point cloud datasets and an initial guess for their relative rigid-body transformation, and iteratively refines the transform by repeatedly generating pairs of corresponding points on the point clouds and minimizing an error metric. Although there are variances of ICP techniques have been proposed to improve the properties of the original ones, either all of these improved ICPs or original ICP mainly consist of two steps:

- matching and selection,
- computation of the transformation parameters.

Here we label these two steps *M* and *C*, respectively. The key idea in *M*-step is to refresh the corresponding points based on the latest transformed target point cloud. While the key idea in

C-step is to calculate the rigid-body transformation parameters by using the latest correspondences. There are three original strategies to execute the searching of correspondences:

- point-to-point (Besl and McKay, 1992),
- point-to-plane (Chen and Medioni, 1991, 1992), and
- point-to-projection (Blais and Levine, 1995).

The important schemes in all above three strategies are how to represent (or define) the closest point and how to find such point. The nearest neighbor searching (Arya et al., 1998) is one of the most important techniques in the *M*-step. Moreover, in the *M*-step information of the normal vector of each point is always employed to accelerate the searching process and to improve the accuracy of the correspondences. KD-tree (Arya et al., 1995) is also a powerful tool that is usually exploited in the *M*-step to speed-up the searching process. The general methods to calculate the normal vectors of point cloud are the local surface fitting, principal components analysis and triangulation. In the *C*-step, the ICP program estimates the updated transformation parameters by calculating a 6 DoF within

$$\mathbf{X}_s = \mathbf{R}\left(\omega,\varphi,\kappa\right)\cdot\mathbf{X}_t + \mathbf{T}(t_x,t_y,t_z) \tag{2.16}$$

where $\boldsymbol{X}_s$ and $\boldsymbol{X}_t$ represent point clouds from source and target respectively. $\boldsymbol{R}(\omega,\varphi,\kappa)$ is a rotation matrix and $\mathbf{T}(t_x,t_y,t_z)$ is a 3D translation. Based on the *M* and *C* steps the ICP algorithm wants to address an optimization problem

$$\min\left\{\sum_{i=1}^{N}\left\|\mathbf{X}_s^i - \left(\mathbf{R}\left(\omega,\varphi,\kappa\right)\cdot\mathbf{X}_t^i + \mathbf{T}\right)\right\|^2\right\}. \tag{2.17}$$

A threshold, ε, always be given to control the iteration. When the following equation holds i.e.

$$\min\left\{\sum_{i=1}^{N}\left\|\mathbf{X}_s^i - \left(\mathbf{R}\left(\omega,\varphi,\kappa\right)\cdot\mathbf{X}_t^i + \mathbf{T}\right)\right\|^2\right\} \le \varepsilon \tag{2.18}$$

the iteration will be terminated.

As we mentioned above, although ICP is a powerful alignment algorithm and usually can generate good results, it still has some shortcomings. In the past two decades, many different strategies (see the references in the last chapter) were presented both in the *M* and *C* steps in order to improve the ICP's properties. In the *M*-step the strategies mostly focus on improving the quality of the correspondences and decreasing the influence from the outliers. In the *C*-step the contributions mainly focus on how to solve the nonlinear minimal problem e.g. using Levenberg-Marquardt method. Many more details about the calculation of ICP the readers can be found from the above-mentioned references.

2.7 Least squares 3D matching (LS3D) algorithm

The LS3D method (Akca, 2010) is a generalization of the least square image matching which is also used to fine registration of two surfaces (source and target). These surfaces are digital/sampled point by point, at different times or from different perspectives. $s(x,y,z)$ and $t(x,y,z)$ are overlapping areas of the object in the source and target surfaces respectively. $s(x,y,z)$ and $t(x,y,z)$ are both implicit representations of a surface fitted to a subset of the points within the point clouds. Similar as the ICP strategy, LS3D is also set to iteratively refresh the translation vector and rotation matrix in order to align $t(x,y,z)$ to $s(x,y,z)$, then the function model in LS3D is

$$s(x,y,z)=t'(x,y,z). \tag{2.19}$$

where $t'(x,y,z)$ represents transformed target surface. According to the property of TLS, it is hard to find true correspondences between $t(x,y,z)$ and $s(x,y,z)$, so taking into account random errors $e(x,y,z)$ in Eq. (2.19) then we can derive the observation equations as:

$$s(x,y,z)-e(x,y,z)=t'(x,y,z). \tag{2.20}$$

The matching is achieved by least squares minimization of a goal function

$$\sum_{i=1}^{n} d^2 = \min. \tag{2.21}$$

where *d* represents the Euclidean distance. Compared with the ICP, the LS3D needs quite good initial values to begin the iteration. If the target surface $t'(x,y,z)$ transformed from its approximation, $t^0(x,y,z)$, then we can linearize Eq. (2.20) by truncated Taylor expansion:

$$s(x,y,z)-e(x,y,z)=t^0(x,y,z)+\frac{\partial t^0(x,y,z)}{\partial x}\cdot dx+\frac{\partial t^0(x,y,z)}{\partial y}\cdot dy+\frac{\partial t^0(x,y,z)}{\partial z}\cdot dz. \tag{2.22}$$

with

$$dx=\sum\frac{\partial x}{\partial o_i}\cdot do_i, dy=\sum\frac{\partial y}{\partial o_i}\cdot do_i, dz=\sum\frac{\partial z}{\partial o_i}\cdot do_i. \tag{2.23}$$

where $o_i \in \{t_x, t_y, t_z, \omega, \varphi, \kappa\}$ is the *i*-th transformation parameter vector. We can write the matrix expression for Eq. (2.23) as

$$\begin{bmatrix} dx \\ dy \\ dz \end{bmatrix} = \begin{bmatrix} dt_x \\ dt_y \\ dt_z \end{bmatrix} + \begin{bmatrix} a_{11} & a_{12} & a_{13} \\ a_{21} & a_{22} & a_{23} \\ a_{31} & a_{32} & a_{32} \end{bmatrix} \cdot \begin{bmatrix} d\omega \\ d\varphi \\ d\kappa \end{bmatrix} \tag{2.24}$$

where a_{ij} are the coefficient terms. Keeping the 3D rigid-body transformation equation Eq.

(2.24) in mind, we can derive a_{ij} as

$$
\begin{aligned}
a_{11} &= 0 \\
a_{12} &= -\sin\varphi\cdot\cos\kappa\cdot x_0 + \sin\varphi\cdot\sin\kappa\cdot y_0 + \cos\varphi\cdot z_0 \\
a_{13} &= r_{12}\cdot x_0 - r_{11}\cdot y_0 \\
a_{21} &= -r_{31}\cdot x_0 - r_{32}\cdot y_0 - r_{33}\cdot z_0 \\
a_{22} &= \sin\omega\cdot\cos\varphi\cdot\cos\kappa\cdot x_0 - \sin\omega\cdot\cos\varphi\cdot\sin\kappa\cdot y_0 + \sin\omega\cdot\sin\varphi\cdot z_0 \\
a_{23} &= r_{22}\cdot x_0 - r_{21}\cdot y_0 \\
a_{31} &= r_{21}\cdot x_0 + r_{22}\cdot y_0 + r_{23}\cdot z_0 \\
a_{32} &= -\cos\omega\cdot\cos\varphi\cdot\cos\kappa\cdot x_0 + \cos\omega\cdot\cos\varphi\cdot\sin\kappa\cdot x_0 - \cos\omega\cdot\sin\varphi\cdot z_0 \\
a_{33} &= r_{32}\cdot x_0 - r_{31}\cdot y_0
\end{aligned}
\tag{2.25}
$$

with rotation matrix as

$$
\begin{aligned}
\mathbf{R} &= \begin{bmatrix} r_{11} & r_{12} & r_{13} \\ r_{21} & r_{22} & r_{23} \\ r_{31} & r_{32} & r_{32} \end{bmatrix} \\
&= \begin{bmatrix} \cos\varphi\cos\kappa & -\cos\varphi\sin\kappa & \sin\varphi \\ \cos\omega\sin\kappa + \sin\omega\sin\varphi\cos\kappa & \cos\omega\cos\kappa - \sin\omega\sin\varphi\sin\kappa & -\sin\omega\cos\varphi \\ \sin\omega\sin\kappa - \cos\omega\sin\varphi\cos\kappa & \sin\omega\cos\kappa + \cos\omega\sin\varphi\sin\kappa & \cos\omega\cos\varphi \end{bmatrix}.
\end{aligned}
\tag{2.26}
$$

Then connecting Eq. (2.22) and Eq. (2.24) we can derive

$$
\begin{aligned}
&-e(x,y,z) = -\left(s(x,y,z) - t^0(x,y,z)\right) + \\
&\begin{bmatrix} \dfrac{\partial t^0(x,y,z)}{\partial x} & \dfrac{\partial t^0(x,y,z)}{\partial y} & \dfrac{\partial t^0(x,y,z)}{\partial z} \end{bmatrix} \cdot \left\{ \begin{bmatrix} dt_x \\ dt_y \\ dt_z \end{bmatrix} + \begin{bmatrix} a_{11} & a_{12} & a_{13} \\ a_{21} & a_{22} & a_{23} \\ a_{31} & a_{32} & a_{32} \end{bmatrix} \cdot \begin{bmatrix} d\omega \\ d\varphi \\ d\kappa \end{bmatrix} \right\}.
\end{aligned}
\tag{2.27}
$$

Eq. (2.27) can be written by matrix notation

$$\mathbf{v} = \mathbf{l} + \mathbf{Ax}. \tag{2.28}$$

For Eq. (2.28) we can use least squares method to solve the Gauss-Markov model. The corresponding stochastic model can be introduced into the adjustment to gain a weight least squares solution. More information about calculation of LS3D can refer to Gruen and Akca (2005), Akca (2010).

2.8 Four-point congruent set (4PCS) algorithm

4PCS algorithm presented by Aiger et al. (2008) is a global rigid registration algorithm for 3D point sets. 4PCS algorithm belongs to coarse registration thus the goal is to align two point clouds and in preparation for fine registration. The key idea of 4PCS is to find a set of four-

point bases in the source cloud that are congruent to a four-point base selected from the target cloud.

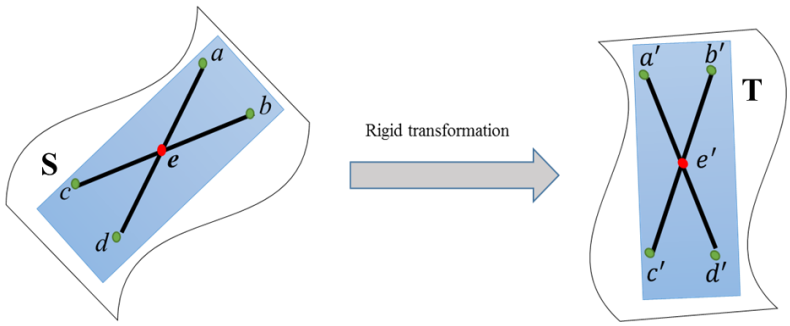

Figure 2.5 Principle of 4PCS.

Pick a set of 4 coplanar points but not collinear from the target point cloud, **T**, and we denote this set as **X' = {a', b', c', d'}** see Figure 2.5. Such that **a'd'** intersects **b'c'** at the intermediate point **e'** (also see Figure 2.5). Then two ratios can be defined as follow:

$$r_1 = \|\mathbf{a}' - \mathbf{e}'\| / \|\mathbf{a}' - \mathbf{d}'\|$$
$$r_2 = \|\mathbf{b}' - \mathbf{e}'\| / \|\mathbf{b}' - \mathbf{c}'\|. \tag{2.29}$$

These ratios are preserved under affine transformations and therefore act as invariants to constrain the search for congruent 4-point bases in the source point cloud, **S**. Based on such characteristic, the program of 4PCS need to find all potential bases from **S**. For each potential base, verify the corresponding aligning transformation, and retain the best transform according to some similarity score. After iteration, the beat congruent 4-point construct can be found in **S** i.e. **X = {a, b, c, d}** (see Figure 2.5). Take into account the stability of 4PCS, many constraints are added into the standard 4PCS e.g. to define

$$\mathbf{e}_{\mathbf{ad}} = \mathbf{a} + r_1 \cdot (\|\mathbf{d} - \mathbf{a}\|)$$
$$\mathbf{e}_{\mathbf{da}} = \mathbf{d} - r_2 \cdot (\|\mathbf{d} - \mathbf{a}\|)$$
$$\mathbf{e}_{\mathbf{bc}} = \mathbf{b} + r_1 \cdot (\|\mathbf{c} - \mathbf{b}\|)$$
$$\mathbf{e}_{\mathbf{cb}} = \mathbf{c} - r_2 \cdot (\|\mathbf{c} - \mathbf{b}\|) \tag{2.30}$$

and then to check

$$\|\mathbf{e}_{\mathbf{ad}} - \mathbf{e}_{\mathbf{bc}}\| < \mu$$
$$\|\mathbf{e}_{\mathbf{ad}} - \mathbf{e}_{\mathbf{cb}}\| < \mu$$
$$\|\mathbf{e}_{\mathbf{da}} - \mathbf{e}_{\mathbf{bc}}\| < \mu$$
$$\|\mathbf{e}_{\mathbf{da}} - \mathbf{e}_{\mathbf{cb}}\| < \mu \tag{2.31}$$

where μ is a given threshold (Theiler et al., 2014). The generalized 4PCS broke the constraint in the construct of 4-point base. Mohamad et al. (2014) gave the third invariant condition in the generalized 4PCS i.e.

$$d_3 = \left\| \mathbf{e}_1 - \mathbf{e}_2 \right\| \tag{2.32}$$

where d_3 represents the intersection distance (see Figure 2.6), which measures the degree of separation between the two pairs. From Eq. (2.32) and Figure 2.6 we can see that when $d_3 = 0$, it implies that the two pairs intersect on the plane, a standard 4PCS base.

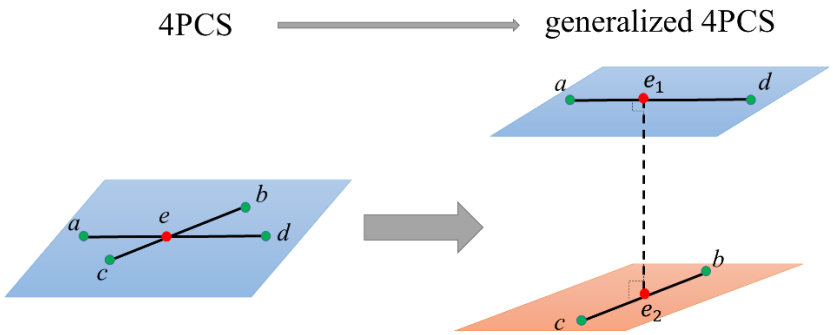

Figure 2.6 Principle of 4PCS to generalized 4PCS.

Chapter 3

Target Identification in Terrestrial Laser Scanning

X. Ge, T. Wunderlich

Survey Review, 47(March), 129-140, 2015

(The text given here is a revised version)

3.1 Abstract

Target identification is an important process in terrestrial laser scanner (TLS) measurements; however, due to strong competition between manufacturers, the design of laser scanners is kept secret and is usually strengthened by accompanying proprietary software. Moreover, the target identification algorithms (i.e., definitions of the target center) are not specified. This makes it difficult for users to objectively compare scanners from different manufacturers and to judge the reliability of the captured scan data by a brand scanner and accompanying software. This paper presents a unified general method to complete the process of target identification. In this paper, the only targets considered are planar quadrant targets. The proposed method consists of four major steps: 1) determination of the target plane, 2) classification of the reflection intensity values and extraction of the border between white and black, 3) detection and elimination of erroneous points from step two, and 4) fitting of the intersection lines and calculation of the center of the two lines. Because TLS is a reflectorless surveying model that can receive hundreds of signals, its measurements require more stringent objective conditions than traditional measurement by total stations (TS). Therefore, robust estimation methods are used to reduce the influence of random errors; moreover, the model of error-in-value (EIV) is also introduced to deal with captured data. Finally, the target's center can be obtained from an

iteration process. For the experiments, a Leica HDS 7000 terrestrial laser scanner, with its accompanying software, Cyclone, and a Leica Laser Tracker AT901were employed. The performance of the proposed method is compared with Cyclone and some early methods from published studies at different resolutions and distances. The paper concludes that the proposed method can obtain reliable results at the same level of accuracy level as those obtained using accompanying software; thus, it provides an objective means to compare the quality of different scanners. The advantage is that our method only makes use of information provided by all scanners and does not require additional proprietary information that cannot be accessed.

Key word: Terrestrial laser scanner; Target identification; Surveying engineering; Reflected intensity

3.2 Introduction

Terrestrial laser scanning (TLS) is a technique that remotely obtains the spatial coordinates of an object using laser light and has become a standard surveying procedure in the architecture, engineering, and construction sectors with a wide range of applications (Gordon and Lichti, 2007; Tristan, 2011; Ebeling et al., 2011). However, the application of TLS has some limitations. On the one hand, information from TLS is always expressed by a vast point cloud of 3D coordinates with a relatively random distribution on the object's surface, preventing a one-to-one correspondence from spots to points. Thus, captured scan data cannot be directly exploited in engineering projects to extract coordinates of a specific object point. On the other hand, TLS measurements require more stringent objective conditions. Researchers have classified the errors in TLS into mainly two categories: internal and external (Lichti and Gordon, 2004; Gordon, 2005; Staiger, 2005) with the latter, i.e., temperature, atmospheric scintillation, dust, distance, reflectance, and spot size, largely affecting the accuracy of the point cloud, which is supported by Granthamn et al., 1997; Lichti and Harvey, 2002; Thiel and Wehr, 2004. Therefore, to enable accurate registration and georeferencing of point clouds, special targets are usually employed to provide virtual center coordinates through automatic extraction algorithms. Any uncertainty in these center coordinates will directly affect the accuracy of the entire project. According to the above, the accuracy of the TLS surveys is to a great extent limited by the target identification quality.

Due to patent protection and strong competition, we cannot access the core of the instrumental system information and the proprietary software algorithms. Without an objective public approach, it is difficult for users to select an appropriate terrestrial laser scanner for their engineering projects in the fast-paced laser scanner market, which has a great variety of measurement systems and a near annual updating of well-known and improved models showing more and more promising specifications. Moreover, different reference standards also provide

further difficulties in the investigation of instrument calibration. Although not very well documented, the topic of target identification has been addressed previously in published literature (Lichti et al., 2000; Gordon et al., 2001; Valanis and Tsakiri, 2004; Kersten et al., 2004). Lichti et al., (2000) proposed three radiometric approaches based on intensity to define the target center as the position with the maximum radiance, the radiometric center of the four strongest returns, and the radiometric center of all returns. In later references, the third method has been proved to perform better than the other two; however, it cannot render reliably accurate results. In Valanis et al., (2004) the C-Means method was used to extract the target center, and the results described are better than those obtained by previous methods. In all the published literature, the results by scanner accompanying software are considered as the true or best center values, and can then be used to verify the proposed methods. Although the results by accompanying software currently seem to be the best choice and assumed to be the virtual "true" value of the target, the different resolutions may also force the accompanying software to produce errors. To the authors' knowledge, there are no documents discussing accompanying software performance over different resolutions or comparisons with self-proposed methods. The purpose of the paper is to propose a new method for laser scanner target identification and to compare its performance over different resolutions and distances with that of the accompanying software. Although there are also other geometric shapes of targets (e.g. spheres, cylinders), we restrict ourselves here to quadrants plane targets. Furthermore, the plane targets are easy to use and more economical than the sphere and cylinder targets especially when you need a lot of targets in your project (e.g. self-calibration see Reshetyuk 2006, 2010; Lichti 2007).

The rest of the paper is organized as follows. In Section 3, we will introduce the iterative formulae of weighted total least squares to solve target fitting. The design of the weight matrix for all observations will be described in detail. Furthermore, the reflection and refraction errors that may be caused by material properties of the object, surface color, moisture of the surface, and so on, and the planarity condition of the resulting plane will be considered, and a robust estimation will be discussed. Section 4 will describe a concept for appropriate reflected intensity values for the captured scan data and will present an iterative calculation method to obtain a reliable target center. Section 5 will discuss the influence of incidence angle in the target identification. The real experiments are carried out in Section 6 to demonstrate the performance and efficiency of the developed method. Finally, remarks will conclude the paper in Section 7.

3.3 Target Plane Fitting

The plane model is defined by:

$$\mathbf{z} = a\mathbf{x} + \mathrm{b}\,\mathbf{y} + \mathrm{c} \tag{3.1}$$

in a leveled scanner local coordinates system. Rewritten as an observation equation:

$$\mathbf{z}+\mathbf{v}_z=\begin{bmatrix}\mathbf{x} & \mathbf{y} & 1\end{bmatrix}\begin{bmatrix}a\\ b\\ c\end{bmatrix}=\mathbf{A}\boldsymbol{\beta} \tag{3.2}$$

where $\mathbf{z}=n\times 1$ is a vector of observed $\mathbf{z}$ coordinates, $\mathbf{v}_z=n\times 1$ is a residual vector of the observations, $\mathbf{A}=n\times 3$ is the design matrix, and $\boldsymbol{\beta}=3\times 1$ is a vector of unknown parameters. Clearly, **x**, **y** in the design matrix are the same coordinate components as in the observation vector **z**, so it is improper to neglect their errors in the calculation. Rewriting the observation equation:

$$\mathbf{z}+\mathbf{v}_z=\left(\begin{bmatrix}\mathbf{x} & \mathbf{y} & 1\end{bmatrix}+\begin{bmatrix}\mathbf{E}_A & 1\end{bmatrix}\right)\begin{bmatrix}a\\ b\\ c\end{bmatrix} \tag{3.3}$$

where $\mathbf{E}_A=n\times 2$ represents the residual matrix of the design matrix $\mathbf{A}$. Then, the restriction turns to the weighted total least squares:

$$\min\left(\mathbf{v}_z^T\mathbf{P}_z\mathbf{v}_z+\mathbf{e}_A^T\mathbf{P}_A\mathbf{e}_A\right) \tag{3.4}$$

where $\mathbf{P}_Z=n\times n$ means the weight matrix of the observation vector, $\mathbf{P}_A=3n\times 3n$ represents the weight matrix of the design matrix, and $\mathbf{P}_A=\mathbf{P}_0\otimes\mathbf{P}_X$ where $\otimes$ expresses the Kronecker product. $\mathbf{P}_0$and $\mathbf{P}_X$ represent the column vector's weight matrix and the row vector's weight matrix of the design matrix, respectively, moreover $\mathbf{P}_0=\boldsymbol{Q}_0^{-1}$, $\mathbf{P}_X=\boldsymbol{Q}_X^{-1}$ and $\mathbf{Q}_A=\mathbf{Q}_0\otimes\mathbf{Q}_X$ (Langville et al. 2003). $\mathbf{e}_A=vec(\mathbf{E}_A)$ and *vec*(.) are to reconstruct a matrix as a vector. In the captured scan data, we assume each returned point to be independent of the others and the coordinate errors to have zero mean, but the coordinate components of a point to be correlated. Then, writing the observation vector's cofactor matrix as:

$$\mathbf{Q}_Z=\begin{bmatrix}\sigma_{z_1}^2 & & & \\ & \sigma_{z_2}^2 & & \\ & & \ddots & \\ & & & \sigma_{z_n}^2\end{bmatrix} \tag{3.5}$$

where $\sigma_{z_1}^2$ is the variance of the *z*-coordinate component of the first point and $\mathbf{P}_Z=\boldsymbol{Q}_z^{-1}$. The column vector's and row vector's cofactors of the design matrix are, respectively:

$$\mathbf{Q}_0=\begin{bmatrix}\sigma_x^2 & \sigma_{xy}^2 & \\ \sigma_{xy}^2 & \sigma_y^2 & \\ & & \kappa\end{bmatrix} \tag{3.6}$$

$$\mathbf{Q}_X = \begin{bmatrix} H_1 & & & \\ & H_2 & & \\ & & \ddots & \\ & & & H_n \end{bmatrix}_{n\times n} \tag{3.7}$$

where σ_x^2 and σ_y^2 represent the mean value of the variances of the *x*- and *y*-axis coordinate components, respectively, and σ_{xy}^2 is the mean value of the co-variance. κ is an epsilon like $\kappa = 10^{-12}$ that means the 3rd column of the design matrix is error free. In Eq. (3.7) $H_i = \sigma_{x_i}^2 + \sigma_{y_i}^2$ and σ_{x_i} , σ_{y_i} express the variances of the *x*-axis and *y*-axis coordinate components of the *i*th point, respectively. Because the points are independent, the off-diagonal elements in Eq. (3.5) and Eq. (3.7) are all assumed zeros. In Eq. (3.4) $\mathbf{v}_z^T\mathbf{P}_z\mathbf{v}_z \geq 0$ and $\mathbf{e}_A^T\mathbf{P}_A\mathbf{e}_A \geq 0$; thus, we can simply obtain the inequality as:

$$\min\left(\mathbf{v}_z^T\mathbf{P}_z\mathbf{v}_z + \mathbf{e}_A^T\mathbf{P}_A\mathbf{e}_A\right) \geq \min\left(\mathbf{v}_z^T\mathbf{P}_z\mathbf{v}_z\right) + \min\left(\mathbf{e}_A^T\mathbf{P}_A\mathbf{e}_A\right) \tag{3.8}$$

Assuming the equality holds, the problem in Eq. (3.4) translates to solve two independent optimization problems. The first element at the right hand-side of Eq. (3.8) is the classical least squares problem and the cofactor matrix for the observation vector as Eq. (3.5), and the second element at the right hand-side of Eq. (3.8) is the data for the least squares problem and the weight matrix for the design matrix as $\mathbf{P}_A$. Therefore, in the above process, coordinate component *z* seems to be independent from coordinate components *x* and *y,* which means the values of covariance between *x*-*z* and *y*-*z* have no influence in the calculation of our model.

From the laser scanning measurement principle, we can obtain each coordinate component's variance-covariance.

$$\begin{cases} x = r \cdot cos\theta \cdot cos\varphi \\ y = r \cdot cos\theta \cdot sin\varphi \\ z = r \cdot sin\theta \end{cases} \tag{3.9}$$

$$\begin{bmatrix} \sigma_x^2 & \sigma_{xy}^2 & \sigma_{xz}^2 \\ \sigma_{xy}^2 & \sigma_y^2 & \sigma_{yz}^2 \\ \sigma_{zx}^2 & \sigma_{zy}^2 & \sigma_z^2 \end{bmatrix} = \mathbf{JCJ}^T \tag{3.10a}$$

$$\mathbf{J}=\begin{bmatrix} \frac{\partial x}{\partial r} & \frac{\partial x}{\partial \theta} & \frac{\partial x}{\partial \varphi} \\ \frac{\partial y}{\partial r} & \frac{\partial y}{\partial \theta} & \frac{\partial y}{\partial \varphi} \\ \frac{\partial z}{\partial r} & \frac{\partial z}{\partial \theta} & \frac{\partial z}{\partial \varphi} \end{bmatrix} \quad and \quad \mathbf{C}=\begin{bmatrix} \sigma_r^2 & & \\ & \sigma_\theta^2+\sigma_{beam}^2 & \\ & & \sigma_\varphi^2+\sigma_{beam}^2 \end{bmatrix} \tag{3.10b}$$

where r, θ, and φ are the range and vertical and horizontal angles of the TLS beam, respectively, and σ_r^2, σ_θ^2 and σ_φ^2 are the respective variances, which can be obtained, for example, from the manufacturer's specification. σ_{beam}^2, the accuracy of laser divergence, is the uncertainty due to the beam width (Lichti and Gordon, 2004). The impact is not obvious over short distances but will show up over longer distances.

We introduced the iterative weighted total least squares by Schaffrin and Wieser (2008) to the calculation as follows:

1. Calculate $\hat{\boldsymbol{\beta}}^{(0)}$ using Least squares method, and $\hat{\boldsymbol{\upsilon}}^{(0)}=0$

$$\hat{\boldsymbol{\beta}}^{(1)}=\left(\mathbf{A}^T\left(\mathbf{Q}_Z+\left(\hat{\boldsymbol{\beta}}^{(0)^T}\mathbf{Q}_0\hat{\boldsymbol{\beta}}^{(0)}\right)\mathbf{Q}_X\right)^{-1}\mathbf{A}\right)^{-1}\mathbf{A}^T\left(\mathbf{Q}_Z+\left(\hat{\boldsymbol{\beta}}^{(0)^T}\mathbf{Q}_0\hat{\boldsymbol{\beta}}^{(0)}\right)\mathbf{Q}_X\right)^{-1}\mathbf{z} \tag{3.11}$$

2. Calculate new $\hat{\boldsymbol{\upsilon}}$ and new $\hat{\boldsymbol{\beta}}$ using the following equations:

$$\boldsymbol{\lambda}^{(i)}=\left(\mathbf{Q}_Z+\left(\hat{\boldsymbol{\beta}}^{(i)^T}\mathbf{Q}_0\hat{\boldsymbol{\beta}}^{(i)}\right)\mathbf{Q}_X\right)^{-1}(\mathbf{z}-\mathbf{A})\hat{\boldsymbol{\beta}}^{(i)} \tag{3.12}$$

$$\hat{\boldsymbol{\upsilon}}^{(i)}=\boldsymbol{\lambda}^{(i)^T}\mathbf{Q}_X\boldsymbol{\lambda}^{(i)} \tag{3.13}$$

$$\hat{\boldsymbol{\beta}}^{(i+1)}=\left(\mathbf{A}^T\left(\mathbf{Q}_Z+\left(\hat{\boldsymbol{\beta}}^{(0)^T}\mathbf{Q}_0\hat{\beta}^{(0)}\right)\mathbf{Q}_X\right)^{-1}\mathbf{A}-\hat{\boldsymbol{\upsilon}}^{(i)}\mathbf{Q}_0\right)^{-1}\mathbf{A}^T\left(\mathbf{Q}_Z+\left(\hat{\boldsymbol{\beta}}^{(i)^T}\mathbf{Q}_0\hat{\boldsymbol{\beta}}^{(i)}\right)\mathbf{Q}_X\right)^{-1}\mathbf{z} \tag{3.14}$$

where the superscript (i)denotes the iteration count.

3. Repeat Step 2 until $\left\|\hat{\boldsymbol{\beta}}^{(i+1)}-\hat{\boldsymbol{\beta}}^{(i)}\right\|\le\delta_0$, where δ_0 is the given threshold.

4. Obtain the vectors of the unknown parameters after the iteration as follows:

$$\hat{\boldsymbol{\beta}}_{WTLS}=\hat{\boldsymbol{\beta}}^{(i+1)} \tag{3.15}$$

In the aforementioned algorithm, $\hat{\boldsymbol{\lambda}}$ is a Lagrange factor, $\hat{\boldsymbol{\upsilon}}$ is an intermediate variable, and δ_0 is the threshold; here we give $\delta_0=10^{-6}$. In the whole process, a threshold ε serves to control the planarity of the resulting plane; in other words, the point will be removed if the distance to the resulting plane exceeds the given threshold. The value of the threshold mainly depends on scanning resolution, distance, and material properties of the object. In the following

experiments, we accept the threshold from 1 mm to 2 mm corresponding to different resolutions. The aforementioned iterative algorithm is repeated, and the threshold is applied to judge the robustness of the captured plane until the entire calculation progresses to convergence. Here, we should note that the so-called total least square estimate within an EIV model can be identified as a special case of the model of least square within the nonlinear Gauss-Helmert model. Thus, the cases in our tests can also be solved by the least square method within the Gauss-Helmert model. In our paper, we assumed that z- value is not correlated with x- and y-values such that we can choose weighted total least squares method to address the linear problems with fewer iterations than least squares method within Gauss-Helmert model.

3.4 Threshold of Intensity and Center Identification

Reflected intensity is one common information parameter we can obtain from the captured scan data with a range of -2047 to +2048. To make the calculation easier and to avoid non-convergence, the intensity range is mapped linearly to the interval of 0 to 1 as follows:

$$\bar{I} = \frac{(I - I_{min})}{I_{max} - I_{min}} \tag{3.16}$$

where I is the original intensity value and $\overline{I}$ is the processed value. I_{min} and I_{max} represent the minimum and maximum values of original intensity respectively. Figure 3.1 shows the point cloud of a target with its property of reflected intensity from an *x*-*z* perspective. It is clear that the target is regularly divided into three categories by the reflected intensity, the 1st category corresponds to the white area of the target with values of intensity approximately over 0.9; the 2nd category corresponds to the black area of the target with that value approximately below 0.3; the rest of the points with an intensity range between 0.3 and 0.9 are classified as the 3rd category, which we called "Middle Value (MV)" in this paper (see Figure 3.2), and those points mainly appear at the junction of black and white areas and also at some parts near the edges. In the example, 0.3 and 0.9 are given as thresholds that show the lower and upper limit, respectively, to select the appropriate point cloud in the later section. The lower and upper limit depend on the resolution and distance in each scanning measurement, but show only slight changes in different situations. Figure 3.3 shows the tests related to the distribution of reflected intensity of target with different resolution within a range of 20 meters, using the Leica HDS 7000 laser scanner. Evidently, all intensity histograms have two peaks, except the last two figures in the first row with middle resolution and over 15 meters. The upper limit rests stably at about 0.9, and the lower limit is approximately in the range of 0.3 to 0.4. In Fig. 3.3 and Fig. 3.8 we used different scales only for visual purposes i.e. esayly finding two-peaks-structure. Selecting the points with an MV of intensity in the point cloud to calculate the target center, see the points with red circles in Figure 3.4.

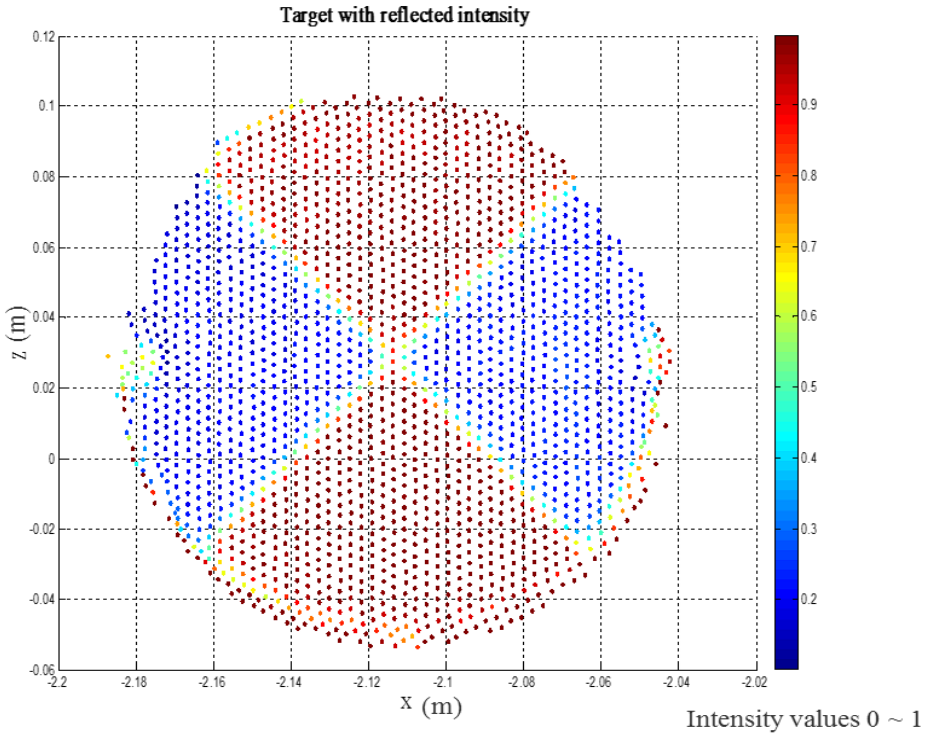

Figure 3.1 Target's point cloud with reflected intensity.

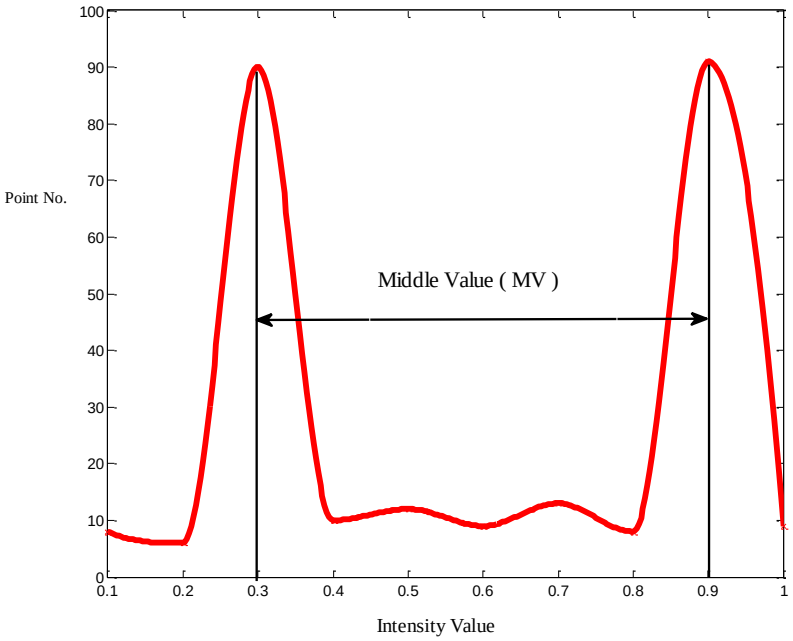

Figure 3.2 "MV" of intensity.

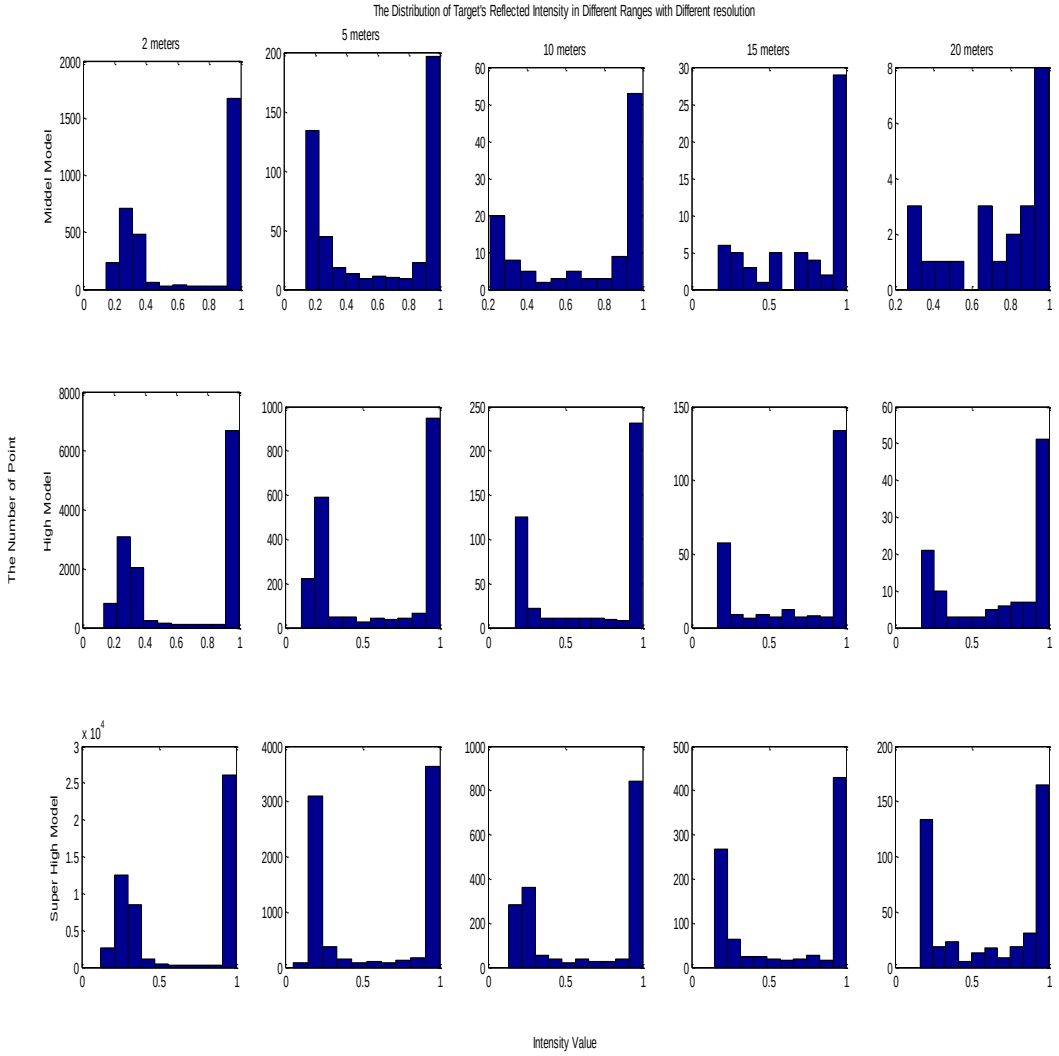

Figure 3.3 Property of intensity with different resolutions and distances

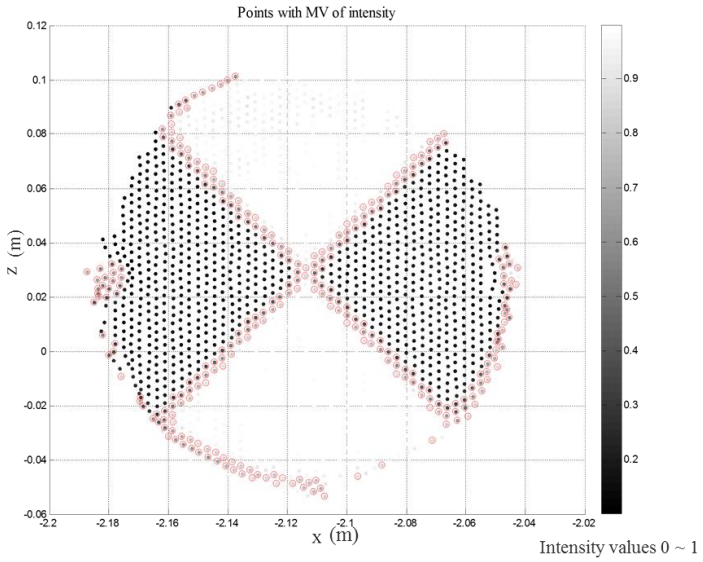

Figure 3.4 Selected points with "MV" of intensity.

According to the discussion above, the points with an MV of intensity do not only appear at the border between black and white, they are also at some parts of the target's edges, see Figure 3.4. Because the target radius is known, we can easily reduce the impact of the edge noise in the center calculation. Exploiting the mean value of the whole target point cloud as an approximate target center, called the mean value center (MVC), the distance of each point to MVC can be calculated, giving a distance threshold smaller than the target's radius to produce a safe range, finally deleting the outside points. It does not prove necessary to complete this process with high accuracy because the loss of some non-edge points does not affect center identification in our approach. Then, the remaining points are projected to the resulting plane so as to transform 3D coordinates to 2D plane coordinates. Figure 3.5 displays an example of the projection result. Obviously, after accurate fitting of two intersecting lines, the center of the target can be obtained. However, setting intensity thresholds cannot always remove all improper points, in other words, there are some noise points with MV of intensity not belonging to the two lines, for example, when scanning in a lower distance with higher resolution. Figure 3.6 shows this with scans within 2 m at a super-high resolution. Taking into account the above-mentioned problem, the M-estimate method is applied in the calculation. Firstly, the MVC is used as the initial value of the target's center, and then the entire area is divided into four quadrants, also see Figure 3.6. Secondly, apply the data in the 1st and 3rd quadrants to fit the 1st line and the data in the remaining quadrants to fit the 2nd line, respectively. Thirdly, calculate the intersection to replace the center in Step 1 and repeat Steps 1 to 3 until the entire process converges. The weighted total least squares technique is applied again to calculate these two lines, and the restriction is the same as in Eq. (3.4). The observation equation reads:

$$\mathbf{y} + \mathbf{v}_y = \left(\begin{bmatrix} 1 & \mathbf{x} \end{bmatrix} + \begin{bmatrix} 1 & \mathbf{E}_A \end{bmatrix}\right)\begin{bmatrix} d \\ e \end{bmatrix} \tag{3.17}$$

where $\mathbf{E}_A = n \times 1$ is the residual matrix of the design matrix $\mathbf{A}$, and $\mathbf{v}_y = n \times 1$ represents the residual vector of the observations (i.e. values in y-axis). *d* and *e* are two unknown parameters. The weight matrices of the design matrix and the observation vector are given as in Eqs. (3.5) to (3.7), using variance of coordinate components. In order to solve the problem of some points with MV of intensity not belonging to the two lines, we apply the weight kernel function (Zhou, 1989) to reweight each point after each iteration.

$$\omega_i = \begin{cases} 1 & |e_i| \le 1.5\hat{\sigma}_0 \\ \dfrac{1.5\hat{\sigma}_0}{|e_i|} & 1.5\hat{\sigma}_0 \le |e_i| \le 2.5\hat{\sigma}_0 \\ 0 & |e_i| > 2.5\hat{\sigma}_0 \end{cases} \tag{3.18}$$

where e_i is the residual of linear fitting and $\hat{\sigma}_0$ is the posterior standard deviation of each iteration. Based on Schaffrin and Wieser (2008), the posterior standard deviation can be calculated by:

$$\hat{\sigma}_0 = \sqrt{\frac{\mathbf{v}_y^T \mathbf{P}_y \mathbf{v}_y + \mathbf{e}_A^T \mathbf{P}_A \mathbf{e}_A}{n-2}} \tag{3.19}$$

where $\mathbf{P}_y$ and $\mathbf{P}_A$ are weight matrices of the observation vector and the design matrix, respectively, in the process of linear fitting. $\mathbf{e}_A$ has the same definition as before. The residual is the vertical distance from the point to the resulting line when applying the total least squares technique in linear fitting.

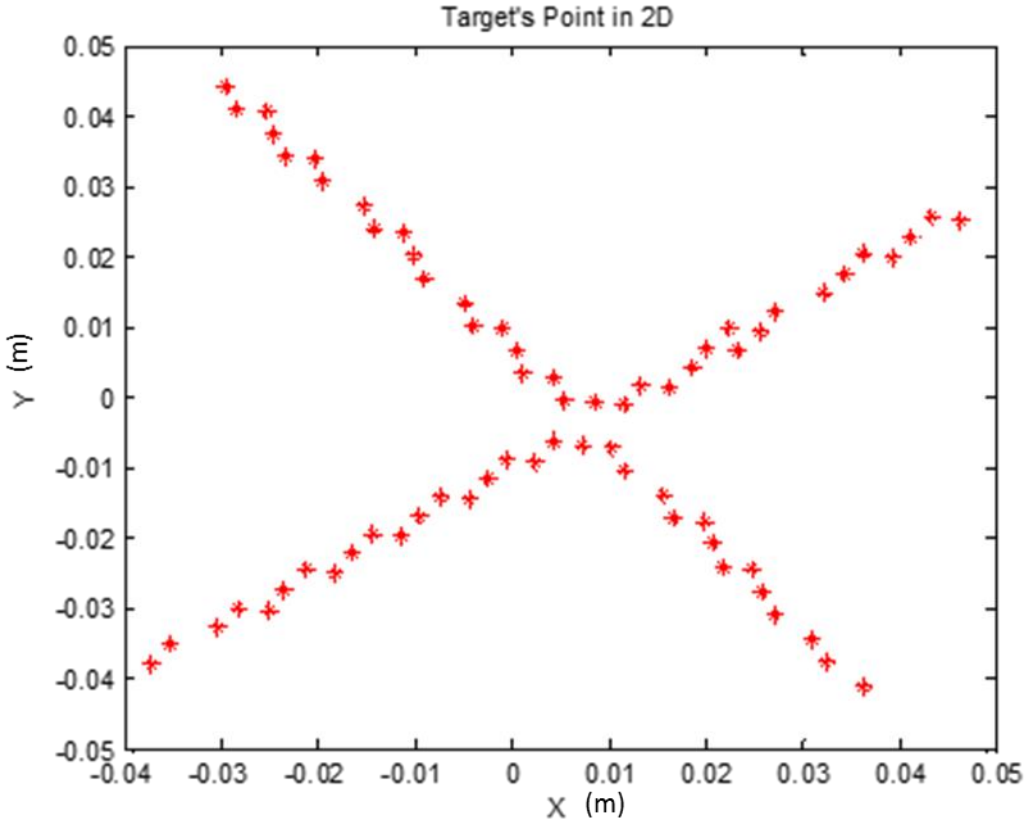

Figure 3.5 Point cloud in 2D system.

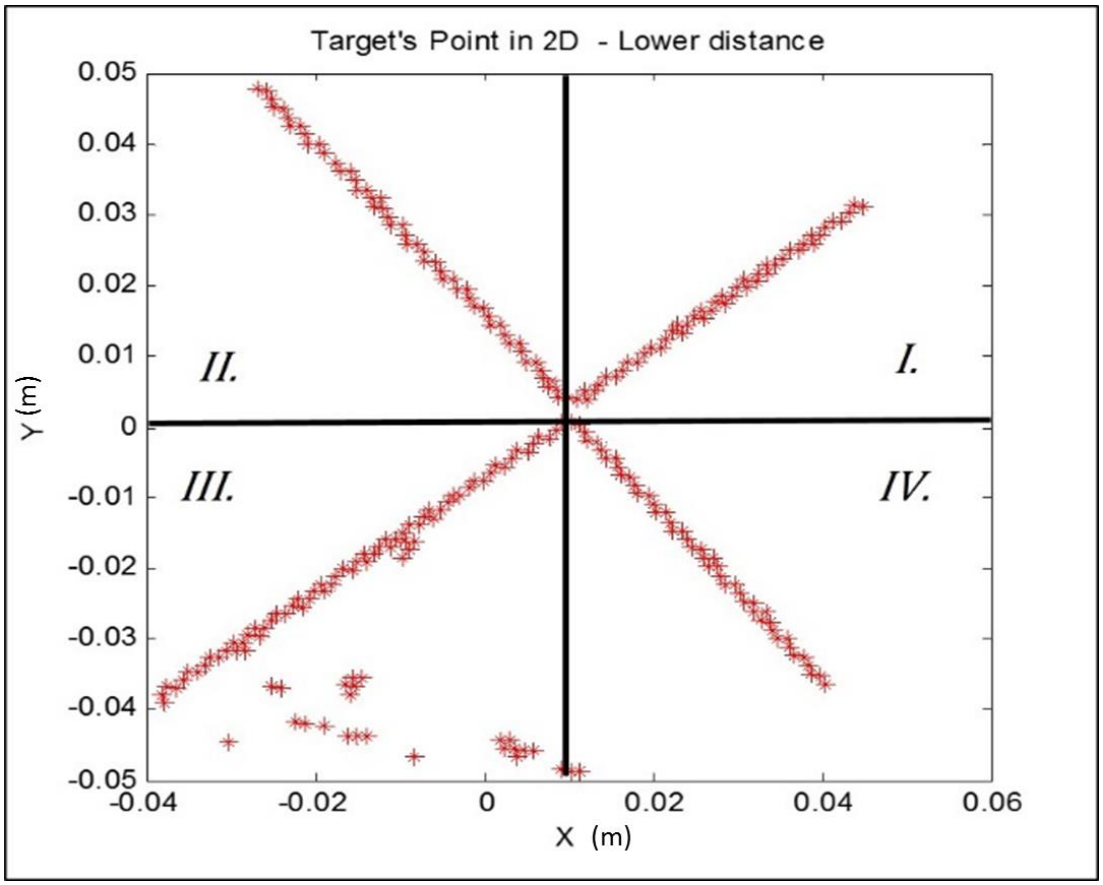

Figure 3.6 Point cloud in 2D system with some noise and its quadrants divided.

3.5 Influence of Incidence Angle

The precision of the target center identification depends on the identification algorithm, but also largely on the quality of the point cloud. As we know, the quality of the point cloud is derived based on the individual point precision per scan and the individual point signal to noise ratio (SNR) is affected by the incidence angle. There are several previous TLS studies (Kremen et al., 2006; Kaasalainen et al, 2005) which focus on the influence of the incidence angle in TLS. Soudarissanane et al. (2009 and 2011) reported that the incidence angle had a cosine effect on the precision of laser points and modeled the incidence angle contribution to the total error budget of a TLS. The most important conclusion from previous studies is that the received signal level of the measurements decreases with increasing incidence angles and the received signal level influences the precision of the distance measurement. Figure 3.7 shows the Leica HDS7000 scanner's theoretical signal deterioration in distance measurements when the incidence angle increases from 0° to 90° (Soudarissanane et al., 2009). Two main points can be found from Figure 3.7, (1) when the incidence angle is larger than 60° the error becomes obvious; (2) the error increases proportional to the distance measured.

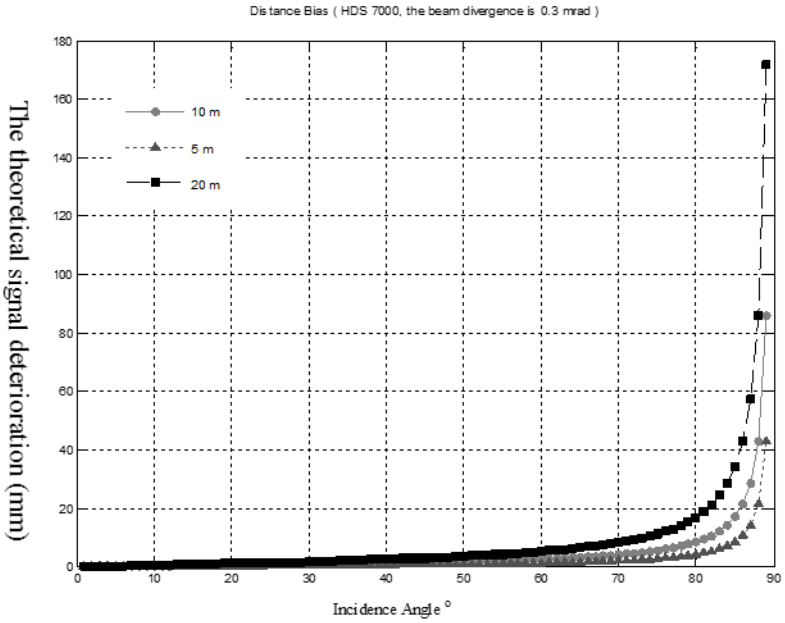

Figure 3.7 The theoretical signal deterioration influence of incidence angles.

In our proposed approach, the target center identification is derived based on the reflected intensity of the individual point. The increasing incidence angle does not only influence the precision of the distance measurement but also the reflected intensity. Figure 3.8 gives the distribution of the target's reflected intensity when the incidence angle increases from 10° to 70°. The first row shows the results scanned by high resolution and the second row those by super high resolution. Compared with Figure 3.3, it is obvious that the overall range of the reflected intensity is reduced and continues to decrease with increasing incidence angle. However, the most important conclusion from Figure 3.8 is that there still exists an MV of intensity when the incidence angle increases and the range of reflected intensity continues to decrease. Thus, when the target is not pointed directly normal to the scanner, we can choose suitable thresholds based on the approximate incidence angles to obtain an acceptable MV of intensity. It is clear that the situations in Fig. 3.3 and Fig. 3.8 directly relate to the reflection of the laser rays by the colors of targets. Thus an MV of intensity can always be detected when we are using a black and white planar quadrant target. The thresholds for choosing an MV of intensity can be found by identifying two peaks in the target's intensity histogram within the curve fitting method. Here we should note that longer distances measured by lower resolution may fail in any algorithm because of the extremely limited sampling. The last histogram in the first row in Figure 3.8 also shows this problem and has to be compared with the histogram in the bottom row of the same column where the MV of intensity can be clearly assessed because of increased resolution.

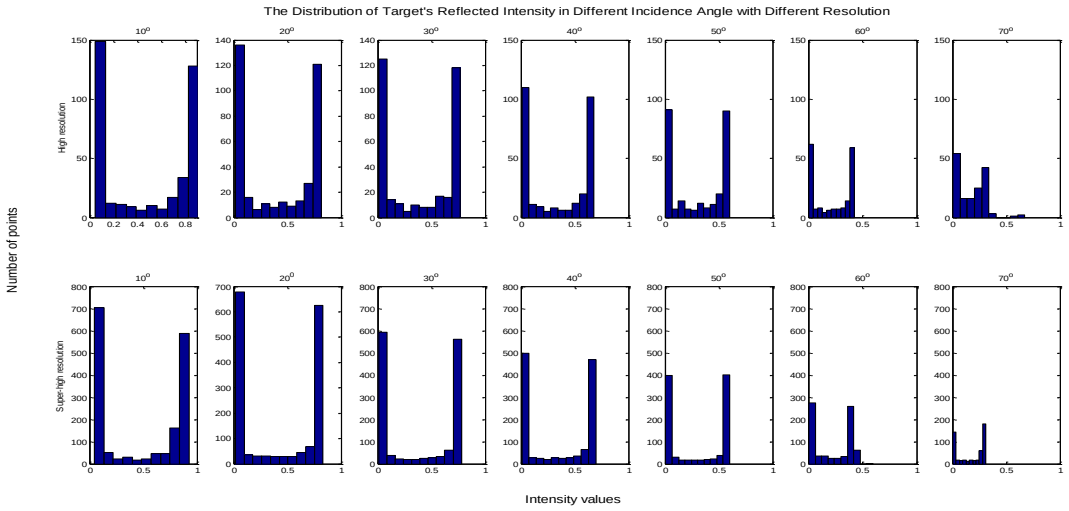

Figure 3.8 The distribution of target's reflected intensity for different incidence angles.

3.6 Application Examples

Experimental field and instruments

In this section, plane fitting and target center identification experiments are shown. The tests were performed in the geodetic laboratory at the Technical University of Munich (TUM), and the results were obtained using the TUM's Leica HDS7000 TLS and its standard black and white targets, together with its accompanying software, Cyclone. The range accuracy of HDS7000 from the specification is 1 mm in linearity error and 125 μrad in angular accuracy, both in horizontal and vertical directions. Three levels of resolution are tested: middle, high, and super-high levels that contain 5,000, 10,000, and 20,000 points in a 360^0 scan, respectively. In the tests for plane fitting, the TUM's Leica Laser Tracker AT901is employed to obtain reference planes and to assess the results by different methods. The coordinate component accuracy of the Laser Tracker is 0.01 mm, which is much higher than in the HDS7000. Four control points have been applied to set up the network. Because the accuracy of the Laser Tracker is much higher than the HDS7000, the errors in the data of the Laser Tracker can be neglected, and the propagation errors from coordinate transformation can be seen as observation errors from the HDS7000. In the tests of target center identification, 15 targets are distributed within a range of 21 meters on the calibration track line. The purpose of the experiments is to test the applicability of the proposed algorithm in the target identification and to compare the performance of the presented method with the accompanying software. More specifically, the results produced by the accompanying software with super-high resolution are accepted as the "true" value $\bar{\boldsymbol{x}}$ in the experiments. For the other results, we compute four residuals for each point: three coordinate components' residuals and one point residual, calculated as:

$$V_{P_i} = \sqrt{v_{x_i}^2 + v_{y_i}^2 + v_{z_i}^2} \tag{3.20}$$

then, directly compute the corresponding RMSE using the following formula:

$$RMSE = \sqrt{\frac{\sum_{i=1}^{i=m} (\hat{\boldsymbol{x}}_i - \bar{\boldsymbol{x}}_i)^T (\hat{\boldsymbol{x}}_i - \bar{\boldsymbol{x}}_i)}{m}} \tag{3.21}$$

where in Eq. (3.20) V_{p_i} is the i^{th} point residual and v_{x_i}, v_{y_i}, and v_{z_i} are corresponding coordinate component residuals. In Eq. (3.21), $\hat{\boldsymbol{x}}_i$ and $\bar{\boldsymbol{x}}_i$ respective denotes the i^{th} estimated and "true" target center coordinates and *m* is the number of points.

Experiment 1: Plane Fitting

Table 3.1 shows the results of parameter estimation of a target plane fitting by different instruments and methods. The results calculated by least squares (LS) and the proposed methods with TLS data are both compared with those calculated by the Laser Tracker data. In this case, the proposed method produces better results than the LS by 84%, 67%, and 84% corresponding to the unknown parameters *a*, *b*, and *c*, respectively. We keep the plane in target size, specifically, the ranges of the *x*- and *y*- axes are respectively between the minimum to maximum with a step of 5 mm. Three fitting planes can be established with calculated parameters, respectively,

$$z = a_1 x + \mathrm{b}_1 y + \mathrm{c}_1 \quad \text{Laser Tracker: Plane } \boldsymbol{Z_1} \tag{3.22a}$$

$$z = a_2 x + \mathrm{b}_2 y + \mathrm{c}_2 \quad \text{Scanner-LS: Plane } \boldsymbol{Z_2} \tag{3.22b}$$

$$z = a_3 x + \mathrm{b}_3 y + \mathrm{c}_3 \quad \text{Scanner-proposed: Plane } \boldsymbol{Z_3} \tag{3.22c}$$

Because the ranges in the *x*- and *y*-axes are approximately the same, we can directly compare the *z*-component to express the mutual positional relationship among the three planes,

$$f = \left|\mathbf{Z_1} - \mathbf{Z}_3\right| - \left|\mathbf{Z_1} - \mathbf{Z}_2\right| \tag{3.23}$$

where, $|\boldsymbol{Z_1} - \boldsymbol{Z}_3|$ and $|\boldsymbol{Z_1} - \boldsymbol{Z}_2|$ represent the vertical distances from $\boldsymbol{Z}_3$ to $\boldsymbol{Z_1}$ and from $\boldsymbol{Z}_3$ to $\boldsymbol{Z}_2$ respectively. So, if $f < 0$ means plane $\boldsymbol{Z_3}$ is closer to plane $\boldsymbol{Z_1}$ than plane $\boldsymbol{Z_2}$. Figure 3.9 shows the f values of the 1st target. From those Tables and the Figure, we can see that (1) the proposed method performs better than the classical method in plane fitting, in other words the proposed method is more robust and can obtain more reliable estimated parameters; (2) the fitting planes calculated by the presented method are mostly closer to the reference planes than that delivered by the LS, especially the middle part of the planes which is always closer to the reference planes by the proposed method, which will directly influence the accuracy of the following target center identification; (3) because the distance is limited to 3 m and scans with super-high resolution do not show the numerical difference of the results between the proposed

method and LS clearly in this case with a resolution of 0.1 mm, that difference will become obvious if the distance increases or the resolution decreases; but (4) there contain some parts with positive values, e.g., the red part in Figure 3.9, in the edge of target which are caused by the ductility of the plane and the intersection of planes, but have little influence in the center identification. Figure 3.10 displays one of the resulting planes by the proposed method.

Table 3.1 Estimated the plane parameters using LS and proposed methods.

Instrument-Method	a	b	c
Laser Tracker	-0.6793	- 0.0041	- 4.8550
Scanner-LS	-0.6830	-0.0032	-4.8626
Scanner-proposed	-0.6787	-0.0038	-4.8538
Improvement*	84%	67%	84%

* e.g.: improvement in a = $\left|\,|a_{tracker} - a_{LS}| - |a_{tracker} - a_{proposed}|\,\right| / |a_{tracker} - a_{LS}|$

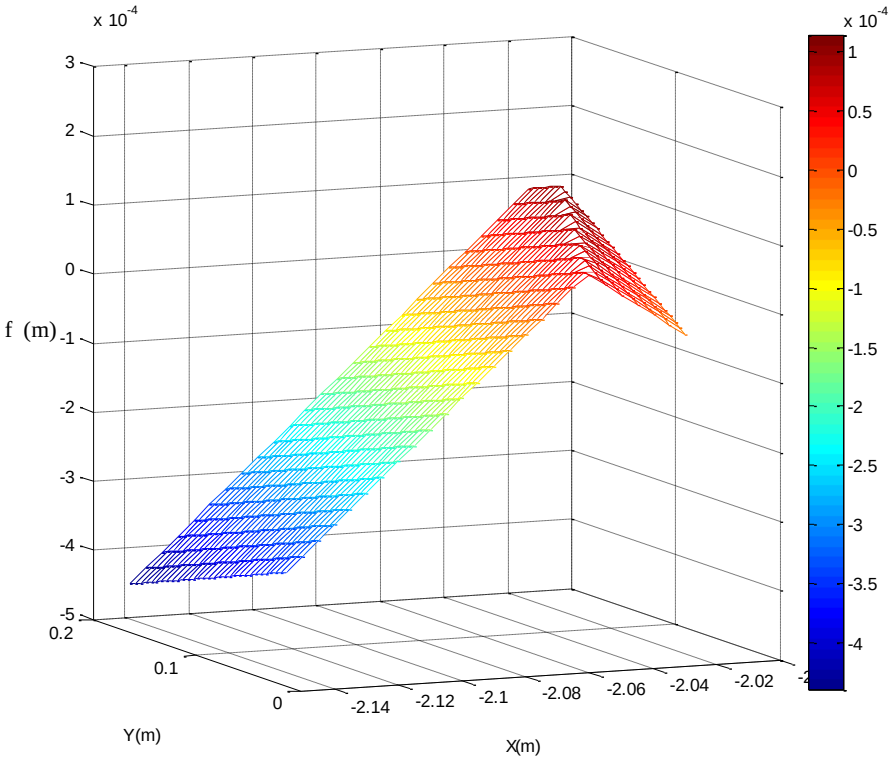

Figure 3.9 The difference in the plane fitting by the LS and proposed method

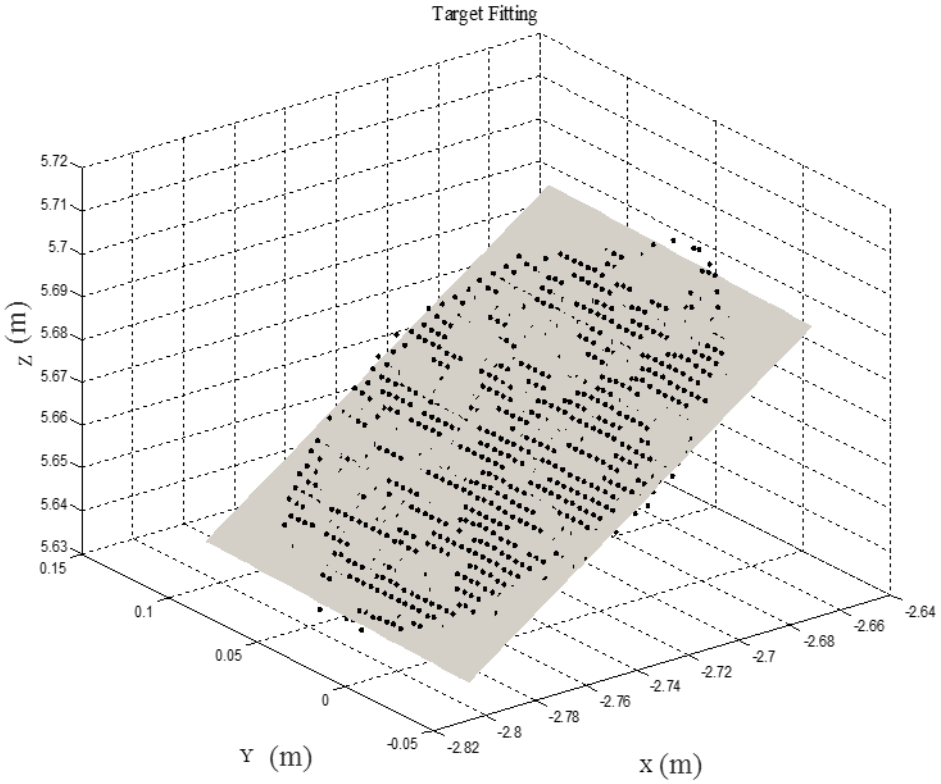

Figure 3.10 The resulting plane by proposed method

Experiment 2: Center Identification

We offer the Cyclone results and our method results in detail in the Table 3.4 and 3.5 respectively, in order to allow readers to check the experiments. We also supply the tested targets raw point clouds on demand for interested readers to repeat the identification experiments. With the super-high and high resolutions, all targets can be identified in our experiments, however, when the scanner uses the middle resolution, the targets in positions No. 13, 14, and 15 cannot be accurately found or even found at all. Table 3.2 presents the bias of each coordinate component and the corresponding position bias in detail, between the "true" values and the results by Cyclone with lower resolutions. According to Table 3.2, we can see that (1) the results by Cyclone with high resolution show just a little difference from the "true" values, and the biases are 1mm more or less. The RMSEs of each coordinate component are less than 1mm and those of the position are slightly larger than 1 mm, (2) the errors in the results by Cyclone with a middle resolution show an upward trend as the distance increases. The points from No.1 to No.5 contain errors at the same level with that obtained by the high model, while after point No.5 the errors noticeably increase. The average positional error for points from No.6 to No.9 is 3.28 mm and from No.10 to 12 is 5.35 mm. The RMSE of the position is 3.50 mm, which means the accuracy of the position decreases by about 178% compared with the high resolution value, which amounts to 1.26 mm.

Like the results by Cyclone, the targets from No.13 to 15 cannot be accurately found because of the limited number of points in the proposed method. Table 3.3 gives a comparison between the results of our proposed method with different resolutions and the “true” values. Based on Table 3.3, we can make the following observations. (1) With super-high resolution, the proposed method can obtain almost the same results as the “true” values. The RMSE of each coordinate component is 0.5 mm more or less, and the RMSE of the position is lower than 1 mm. In engineering measurement or even in precision engineering measurement, the results calculated by our proposed method can be accepted with the same accuracy level as “true” values. (2) With high resolution, the proposed method can also obtain reliable results, the RMSE of each coordinate component is also lower than 1mm, and the same index for the position is slightly larger than 1 mm. Moreover, these results perform almost at the same level as those obtained by Cyclone with the same resolution. (3) With a middle resolution, the proposed method can obtain reliable results in the first five points; from the No.6 point, the positional error becomes larger than 2 mm. The RMSE of position is 2.76 mm, which means the accuracy increases by 21.14%, compared with that index obtained by Cyclone with the same resolution.

Table 3.2 Biases of coordinate components and position respective with high and middle resolutions by Cyclone.

	High Resolution Model				**Middle Resolution Model**				
Target Number	**Coordinate Component**			**Point**	**Coordinate Component**			**Point**	**Distance (m)***
	Bias (mm) = true value – estiamted value								
	Δx	Δy	Δz	ΔP	Δx	Δy	Δz	ΔP	D
1	0	0	0	0.0	-1	0	0	1.0	1.8531
2	0	1	0	1.0	0	0	0	0.0	3.3967
3	0	0	0	0.0	0	0	-1	1.0	4.8625
4	0	0	0	0.0	0	0	-1	1.0	6.2961
5	0	0	0	0.0	0	0	0	0.0	7.8011
6	0	1	1	1.4	0	1	-3	3.2	9.3189
7	0	1	0	1.0	-2	-1	1	2.4	10.6149
8	1	0	0	1.0	-2	-1	-2	3.0	11.9215
9	0	0	-1	1.0	2	0	-4	4.5	13.2987
10	0	0	-1	1.0	4	2	-3	5.4	14.6879
11	1	0	0	1.0	1	-1	-7	7.1	16.3394
12	1	1	-1	1.7	3	1	-3	4.4	17.7700
13	-1	-1	2	2.4					19.0568
14	-1	-1	0	1.4					20.4610
15	1	0	-2	2.2					21.9748
RMSE	0.63	0.63	0.89	1.26	1.80	0.87	2.74	3.50	

***** Distance: from the scanner to the measured target.

Table 3.3 Biases of coordinate components and position respective with super high, high and middle resolutions by proposed method.

Super High Resolution Model					
Target Number	**Coordinate Component**			**Point**	**Distance (m)**
	Bias (mm) = true value – estiamted value				
	Δx	Δy	Δz	ΔP	D
1	0	0	0	0.0	1.8531
2	0	0	0	0.0	3.3967
3	0	0	0	0.0	4.8625
4	0	0	-1	1.0	6.2961
5	0	0	0	0.0	7.8011
6	0	1	0	1.0	9.3189
7	0	1	0	1.0	10.6149
8	0	0	0	0.0	11.9215
9	0	0	0	0.0	13.2987
10	0	0	0	0.0	14.6879
11	1	0	0	1.0	16.3394
12	0	0	-1	1.0	17.7700
13	0	1	1	1.4	19.0568
14	0	1	-1	1.4	20.4610
15	-1	0	0	1.0	21.9748
RMSE	0.37	0.51	0.52	0.81	
High Resolution Model					
Target Number	**Coordinate Component**			**Point**	**Distance (m)**
	Bias (mm) = true value – estiamted value				
	Δx	Δy	Δz	ΔP	D
1	0	0	0	0.0	1.8531
2	0	0	0	0.0	3.3967
3	0	0	-1	1.0	4.8625
4	0	0	0	0.0	6.2961
5	0	0	0	0.0	7.8011

6	0	0	-1	1.0	9.3189
7	0	1	0	1.0	10.6149
8	0	0	1	1.0	11.9215
9	0	0	0	0.0	13.2987
10	-1	1	-1	1.7	14.6879
11	1	1	1	1.7	16.3394
12	0	1	1	1.4	17.7700
13	0	0	1	1.0	19.0568
14	0	1	-1	1.4	20.4610
15	-1	1	1	1.7	21.9748
RMSE	0.45	0.63	0.77	1.09	
Middle Resolution Model					
Target Number	**Coordinate Component**			**Point**	**Distance (m)**
	Bias (mm) = true value – estiamted value				
	Δx	Δy	Δz	ΔP	D
1	0	0	0	0.0	1.8531
2	0	1	0	1.0	3.3967
3	0	0	0	0.0	4.8625
4	0	0	0	0.0	6.2961
5	-1	0	0	1.0	7.8011
6	-1	0	-2	2.2	9.3189
7	1	1	2	2.4	10.6149
8	-1	0	2	2.2	11.9215
9	0	0	-2	2.0	13.2987
10	0	1	3	3.2	14.6879
11	-4	-1	-2	4.6	16.3394
12	-5	-2	3	6.2	17.7700
RMSE	1.94	0.82	1.78	2.76	

Figure 3.11 displays four target centers of target No.8 captured by four methods in the *z-x* perspective. The grey dots represent the sample of target point clouds and were removed the center areas only for the visual purpose. The black and grey squares express the center obtained

by Cyclone and our proposed method, respectively. Obviously, these two squares are very close, almost overlapping. The black triangle represents the center obtained by the radiometric center of all returns (Lichti et al., 2000), and the grey triangle represents the center captured by MVC. Clearly, these two centers deviate from the "true" value of center.

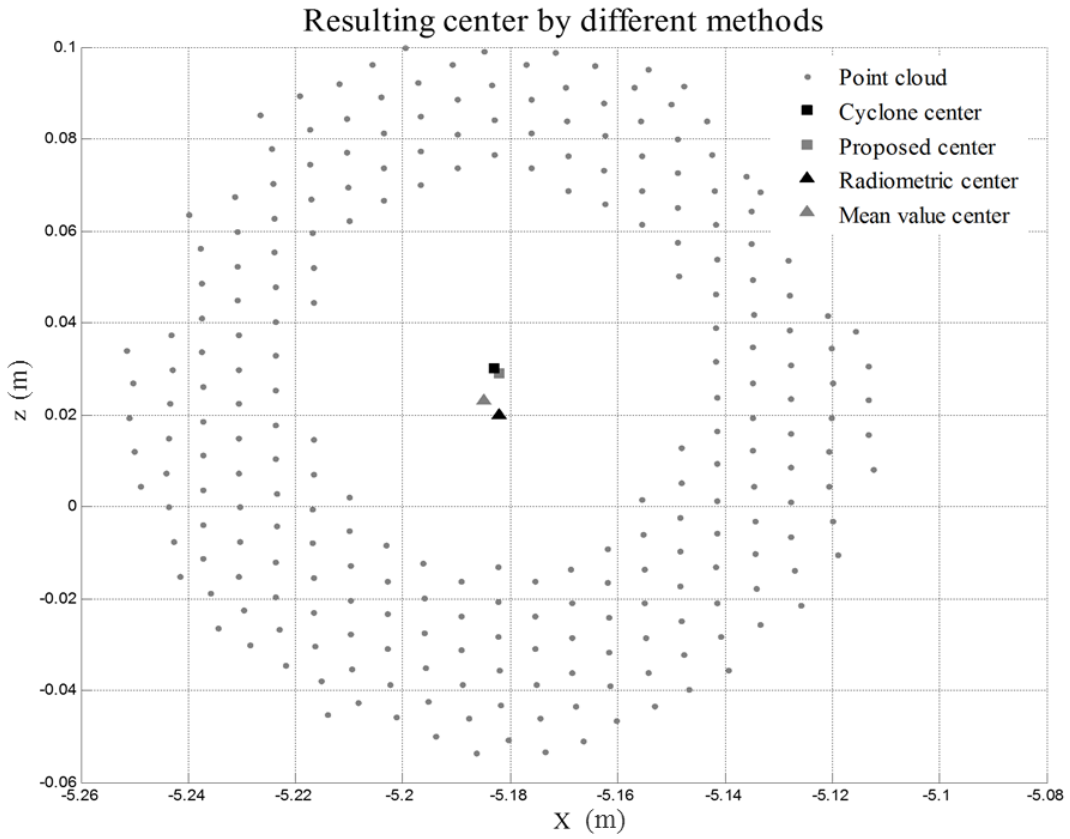

Figure 3.11 Four estimated target centers by different methods

3.7 Conclusions

In this work, we proposed an alternative method for target identification in TLS measurement. In the proposed method, the weighted total least squares method is employed to obtain an optimum fitting plane. The planarity condition of the plane is introduced in the plane fitting algorithm to control the accuracy of the resulting plane. After the first step, the characteristics of reflected intensity between different colors is applied to select appropriate points and then project them to the 2D coordinate system. Finally, through a robust iterative calculation, the target center can be successfully obtained.

The analysis of the experimental results demonstrates the applicability of the proposed method in target identification. From the case study results, we draw the following conclusions:

1. In my tests the accuracy of results by arbitrary accompanying software (in our case, Cyclone) is reduced due to lower resolution or increased distance. Considering the accuracy requirement and time-consumption in each engineering project, choosing the optimum resolution model is very important.
2. The method proposed here can obtain approximately the same accuracy level as that returned by the accompanying software within the range of the tests but just uses common information to complete the target identification process. This gives users increased scope to improve target identification.
3. Furthermore, this method is objectively equal for same manufacturer's instruments; thus, users can objectively compare different instruments' behavior with respect to target identification. It should be repeated that the quality of target identification directly influences registration quality and has high importance.

Table 3.4 Target Centers obtained by Cyclone with different resolutions.

Cyclone (m)												
No.	**Super High (True)**				**High**				**Middle**			
	x	***y***	***z***	**Point No.**	***x***	***y***	***z***	**Point No.**	***x***	***y***	***z***	**Point No.**
1	-0.806	1.670	0.028	52046	-0.806	1.670	0.028	13325	-0.805	1.670	0.028	3303
2	-1.476	3.060	0.028	16097	-1.476	3.059	0.028	3944	-1.476	3.060	0.028	963
3	-2.114	4.378	0.028	7847	-2.114	4.378	0.028	2063	-2.114	4.378	0.029	466
4	-2.737	5.669	0.028	4468	-2.737	5.669	0.028	1200	-2.737	5.669	0.029	323
5	-3.392	7.024	0.029	3134	-3.392	7.024	0.029	771	-3.392	7.024	0.029	187
6	-4.052	8.391	0.029	2150	-4.052	8.390	0.030	571	-4.052	8.390	0.032	138
7	-4.615	9.559	0.030	1707	-4.615	9.558	0.030	448	-4.613	9.560	0.029	111
8	-5.182	10.736	0.030	1323	-5.183	10.736	0.030	336	-5.180	10.737	0.032	91
9	-5.782	11.976	0.029	1058	-5.782	11.976	0.030	286	-5.784	11.974	0.033	73
10	-6.386	13.227	0.029	896	-6.386	13.227	0.030	256	-6.390	13.225	0.032	60
11	-7.104	14.714	0.031	729	-7.105	14.714	0.031	184	-7.105	14.715	0.038	49
12	-7.728	16.003	0.031	588	-7.729	16.002	0.032	162	-7.731	16.002	0.028	34
13	-8.283	17.154	0.033	548	-8.282	17.155	0.031	140				
14	-8.897	18.426	0.030	432	-8.896	18.427	0.030	116				
15	-9.555	19.790	0.032	372	-9.556	19.790	0.034	103				

Table 3.5 Target Centers obtained by proposed method with different resolutions.

Proposed Method (m)												
No.	**Super High**				**High**				**Middle**			
	x	**y**	**z**	**Point No.**	**x**	**y**	**z**	**Point No.**	**x**	**y**	**z**	**Point No.**
1	-0.806	1.670	0.028	52046	-0.806	1.670	0.028	13325	-0.806	1.670	0.028	3303
2	-1.476	3.060	0.028	16097	-1.476	3.060	0.028	3944	-1.476	3.059	0.028	963
3	-2.114	4.378	0.028	7847	-2.114	4.378	0.029	2063	-2.114	4.378	0.028	466
4	-2.737	5.669	0.029	4468	-2.737	5.669	0.028	1200	-2.737	5.669	0.028	323
5	-3.392	7.024	0.029	3134	-3.392	7.024	0.029	771	-3.391	7.024	0.029	187
6	-4.052	8.390	0.029	2150	-4.052	8.391	0.030	571	-4.051	8.391	0.031	138
7	-4.615	9.558	0.030	1707	-4.615	9.558	0.030	448	-4.616	9.558	0.028	111
8	-5.182	10.736	0.030	1323	-5.182	10.735	0.029	336	-5.181	10.737	0.028	91
9	-5.782	11.976	0.029	1058	-5.782	11.976	0.029	286	-5.782	11.976	0.031	73
10	-6.386	13.227	0.029	896	-6.385	13.226	0.030	256	-6.386	13.226	0.026	60
11	-7.105	14.714	0.031	729	-7.105	14.713	0.030	184	-7.100	14.715	0.033	49
12	-7.728	16.003	0.032	588	-7.728	16.002	0.030	162	-7.723	16.005	0.028	34
13	-8.283	17.153	0.032	548	-8.284	17.154	0.032	140				
14	-8.897	18.425	0.031	432	-8.897	18.425	0.031	116				
15	-9.554	19.790	0.032	372	-9.554	19.789	0.031	103				

Chapter 4

Configuration Requirements for Terrestrial Laser Scanner Calibration within a Point Field

Xuming Ge, A. Wieser, T. Wunderlich

IEEE Transactions on Geoscience and Remote Sensing. 2016. Under review.

(The text given here is a revised version)

4.1 Abstract

The goal of laser scanner calibration is to estimate the parameters of a deterministic model of scanner biases in order to mitigate these biases and their effect on the scanning results. In this paper, we focus on the prediction and planning of the quality of point-field based scanner calibration. First, we propose specific criteria for assessing whether the estimated calibration parameters ("additional parameters", APs) are accurate enough. We relate a statistical bound of the unknown deviation of the estimates to the standard deviations of the scanner's raw measurements. Second, we carry out an observability analysis individually for each AP, highlighting the required number and spatial distribution of scanned object points. We also identify parameters which can hardly be observed by this type of calibration and may have to be determined separately, e.g. by component calibration. Finally, we apply the criteria and configuration requirements as basic building blocks to the design of a point-field and scanner setup plan for determination of a frequently used subset of APs for (i) calibration in an indoor field with separately measured target coordinates, and (ii) for scanner self-calibration.

Keywords: Terrestrial laser scanner; Calibration; Point-field; Accuracy; Correlation; Prediction

4.2 Introduction

The accuracy of terrestrial laser scanning (TLS) results is limited by a variety of factors including uncompensated instrumental biases, target surface structure and material properties, atmospheric effects, residual deviations of point cloud registration, and others (Kaasalainen et al., 2010; Polo et al., 2012; Fang et al., 2015; Ge and Wunderlich, 2015, 2016). In order to exploit the accuracy potential of the instruments, scanners need to be calibrated such that the effect of instrumental biases is negligible compared to the other effects.

Scanners can be calibrated by component calibration or by system calibration. In component calibration, precise knowledge of the individual system components and their respective error contributions is required (Schulz, 2008). Assuming that the error of the entire system can be synthesized from the errors of the individual sub-systems, the latter are calibrated separately using different equipment and approaches. In system calibration, the parameters used to model and mitigate the deviations of TLS measurements are all determined together within one calibration process. If the necessary calibration parameters are actually observable by system calibration, it may even be possible to carry out a self-calibration determining the calibration parameters on the job, i.e. along with the wanted coordinates of the points in the point-cloud and with possibly required further (nuisance) parameters. This may be more economic than separate scanner calibration and is also attractive in terms of accuracy because the calibration is up-to date when used and the scanning results are therefore not affected by possibly outdated parameters from a prior calibration (Lichti, 2007).

TLS system calibration is based on a deterministic model of the deviations of distance and angle measurements. The result of the calibration are estimated values of the parameters of this model. Lichti (2007) has presented such a model. Its parameters have been called *additional parameters* (APs). Since then Lichti and others have published a series of papers on laser scanner self-calibration, discussing correlation sources and parameter de-correlation for both panoramic and hybrid scanners, (e.g., Lichti, 2007, 2009, 2010; Lichti and Licht, 2006; Lichti et al., 2011). Reshetyuk (2010) presented an approach in which all parameters in the model

were additionally treated as observations with suitably chosen prior weights. This allows including prior knowledge, reducing correlations, and increasing the precision of the estimated parameters – provided suitable prior values are available e.g. from a previous calibration. Using certain AP models and stochastic information about the parameters of external orientation (EOs) Reshetyuk (2010) succeeded in de-correlating APs and nuisance parameters even further. Another TLS system calibration methods can refer to Garcia-San-Miguel and Lerma (2013) and Chan et al. (2015).

The main goal of calibration is to estimate APs which significantly reduce the deviation between the scanner measurements and the corresponding true values when applied to the measurements output by the scanner. Lichti (2010) analyzed the influence of target distribution, size of target point field, and number of targets on the correlation and precision of the estimated parameters. Reshetyuk (2010) discussed possibly high correlation between APs and EOs, obtained with an essentially random distribution of the targets. However, so far no specific rules were given to predict and assess whether the accuracy of the APs as obtained with a particular calibration point field and setup of measurements is sufficient. Such rules would be of high value for (i) planning and establishing a calibration point field, (ii) assessing calibration results obtained from self-calibration or from an ad-hoc point field, and (iii)assessing which APs can be determined from scans of a (given) point field and which need to be determined from separate calibration.

The primary goal of this paper is to fill this gap by proposing a criterion for relating predictable quality indicators to application requirements and by deriving related configuration requirements of the point field and scanner setup. In a first step we derive criteria to judge whether the estimated APs are sufficiently accurate. The criteria are independent of the specific (estimated) values of the APs but related to the impact on the point cloud coordinates.

In a second step we analyze the relation between the spatial distribution of the object points (OPs) used for calibration and the related observability of the APs on an AP-per-AP basis. This is intended to enhance the understanding of how individual OPs or sets of OPs contribute to the estimated parameters and thus to facilitate derivation of both a suitable OP distribution and a suitable measurement plan for calibration involving an entire set of APs. We finally demonstrate the application of the criteria and of the geometric building blocks to the calibration of a scanner in an indoor calibration point field.

The OPs are points which can be identified either in more than one point cloud or in at least one point cloud and in the real scene. Within this paper we assume that they are represented by markers, e.g. a checkerboard pattern printed on a flat surface, such that their coordinates in the scanner coordinate system can be calculated from the points of the point cloud and their respective signal strength indicators, and that they can also be measured independently using e.g. a total station.

4.3 Mathematical model

We base our investigation on the AP model introduced by Lichti (2007). However, our approach can easily be applied to any other TLS error model, like those presented e.g. by Gordon and Lichti (2007), by Holst and Kuhlmann (2014), by Hartzell et al. (2015), or by Domingo-Perez et al., (2016). The deviations of the measured distances (ρ), and of the measured horziontal (θ) and vertical angles (α) are expressed as functions of these values and some auxiliary quantities as follows:

$$\delta\rho = a_0 + a_1\rho + a_2\sin(\alpha) + a_3\sin\left(\frac{4\pi}{U_1}\rho\right) + a_4\cos\left(\frac{4\pi}{U_1}\rho\right) + a_5\sin\left(\frac{4\pi}{U_2}\rho\right) + a_6\cos\left(\frac{4\pi}{U_2}\rho\right) + a_7\sin(4\theta) + a_8\cos(4\theta) \quad (4.1)$$

$$\delta\theta = b_1\sec(\alpha) + b_2\tan(\alpha) + b_3\sin(2\theta) + b_4\cos(2\theta) + b_5\theta + b_6\cos(3\theta) + b_7\sin(4\theta) \quad (4.2)$$

$$\delta\alpha = c_0 + c_1\alpha + c_2\sin(\alpha) + c_3\sin(3\alpha) + c_4\cos(3\alpha) \quad (4.3)$$

The a_i, b_i and c_i are the parameters of the model i.e., the APs, whereas the U_i are the first (finest) and second modulation wavelength of the distance measurement unit. As can be seen from (1) the terms with coefficients a_3 to a_6 only apply to phase-based scanners and will have to be omitted with scanners measuring the time-of-flight directly. The discussion in Lichti (2007) shows that some of the above APs are empirical, i.e. they were found to mitigate systematic effects detected within the measurement residuals of some scanners but not yet causally explained. So, only a subset of the above APs (and perhaps some additional ones) may be needed for a specific scanner, in particular, since the data output by the scanner has typically

been 'corrected' already within the instrument using the (undisclosed) functions and parameters determined by the manufacturer.

The calibration, i.e. the estimation of the AP values, is based on the relation between the coordinates of the object points expressed in a chosen external coordinate frame (target- or *t*-frame) and in the coordinate frame of the scanner which we consider to be different for each scan and scanner setup (*i*-frame for the *i*-th scan or setup). The transformation between these frames is described using six external orientation parameters (EOs) per scan namely the 3D translations $\Delta \boldsymbol{x}_i^t(\mathrm{x},\mathrm{y},\mathrm{z})$ and the three rotation angles resulting in the rotation matrix $\boldsymbol{R}_i^t(\omega,\varphi,\kappa)$. The coordinates $\mathbf{x}_j^i$ of the *j*-th OP expressed in the *i*-th scanner frame are a function of the polar elements $\boldsymbol{r}_j^i = \left[\rho_j^i, \theta_j^i, \alpha_j^i\right]$ already introduced above. However, the true values of these elements differ from the ones output by the scanner (or recalculated from $\mathbf{x}_j^i$) by the biases $\delta\rho_j^i$, $\delta\theta_j^i$ and $\delta\alpha_j^i$ and by zero-expectation random deviations $e_{\rho_j^i}, e_{\theta_j^i}, e_{\alpha_j^i}$. So, the condition

$$\tilde{\mathbf{x}}_j^t - \Delta\tilde{\mathbf{x}}_i^t - \tilde{\mathbf{R}}_i^t\tilde{\mathbf{x}}_j^i = \mathbf{0} \tag{4.4}$$

is fulfilled by the underlying true quantities (indicated by the tilde symbol) with:

$$\tilde{\mathbf{x}}_j^i = \tilde{\rho}_j^i \cdot \begin{bmatrix} \cos\tilde{\theta}_j^i \cos\tilde{\alpha}_j^i \\ \sin\tilde{\theta}_j^i \cos\tilde{\alpha}_j^i \\ \sin\tilde{\alpha}_j^i \end{bmatrix} \tag{4.5}$$

and

$$\tilde{\rho}_j^i = \rho_j^i + \delta\rho_j^i + \tilde{e}_{\rho_j^i},\ \tilde{\theta}_j^i = \theta_j^i + \delta\theta_j^i + \tilde{e}_{\theta_j^i},\ \tilde{\alpha}_j^i = \alpha_j^i + \delta\alpha_j^i + \tilde{e}_{\alpha_j^i} \tag{4.6}$$

Assuming that the biases are fully described by the deterministic model eqs. (4.1-4.3), we may use eqs. (4.4-4.6) together with (4.1-4.3) for estimating the unknown APs, EOs, and OPs. This can be achieved with a variety of different adjustment models. We have chosen to carry out all calculations within a Gauss-Helmert model starting from the non-linear condition equations (4.4). However, the criteria, results and conclusions derived in the remainder of this paper are independent of this choice and hold also if a Gauss-Markov model is used, as by Lichti (2007). Both approaches allow including further observations as needed e.g., OP coordinates measured

with an independent measurement system, all or certain EOs observed directly, or APs taken from a previous calibration. The starting point for the following analysis is the variance covariance matrix (VCM) of all APs and all other parameters jointly estimated.

4.4 Definition of criteria

The estimated APs need to be sufficiently accurate and sufficiently uncorrelated. The former assures that applying the estimated APs will actually improve the accuracy of the TLS measurements. The latter facilitates interpretation and comparison of the values (e.g. with respect to their stability over time) and is a prerequisite for successful application of the APs to scans beyond the ones from which they were estimated. We need criteria to check precision and correlation both for planning the calibration and for assessing the success of a calibration actually carried out. In this section we propose such criteria making sure that they are applicable to a variety of scanners and applications. Subsequently we use these criteria to derive proposed geometric configurations for point field based scanner calibration.

4.4.1 Precision

The estimated AP values differ from the underlying true values such that their application leaves a bias in the 'corrected' range and angle measurements and consequently in the coordinates of the point clouds. We will consider these biases negligible (and thus the accuracy of the estimated APs sufficient) if they are substantially lower than the standard deviations of the corresponding range and angle measurements. Assuming that the estimation of the APs is carried out robustly such that the results are most likely not affected by outliers and that there are no un-modeled systematic deviations the unknown bias[1] of the estimated APs can be assessed using their predicted precision. We demonstrate the derivation of the corresponding criteria for a few selected parameters and then list the results for all APs.

The deviation $\Delta\delta\rho_{(\hat{a}_0)}$ of $\delta\rho$ caused by the bias $\varepsilon_{\hat{a}_0}$ of $\hat{a}_0$ (hat indicates estimated quantities) i.e., its deviation from the corresponding true value, can be derived from eq. (4.1) as

[1] We denote the entire difference between estimated and unknown true value as *bias* henceforth, not referring to biased or unbiased estimation in the statistical sense.

$$\Delta\delta\rho_{\,(|\hat{a}_0|)} = \frac{\partial\delta\rho}{\partial a_0}\cdot\varepsilon_{\hat{a}_0} = \varepsilon_{\hat{a}_0} \tag{4.7}$$

which is strict in this case, because the range deviation δρ is a linear function of a_0.

We consider this bias to be negligible if

$$\left|\Delta\delta\rho_{\,(\hat{a}_0)}\right| \le \mu_\rho\sigma_\rho, \tag{4.8}$$

with a suitably chosen range negligibility factor $0 < \mu_\rho < 1$ and with σ_ρ representing the standard deviation of the range observations. We will assume henceforth that σ_ρ is constant, but extending the results to situations where it varies with distance would be easily possible. Since the actual bias is stochastic we cannot assure that eq. (4.8) is fulfilled. However, we can relax the criterion by associating it with a probability. We assume the bias as negligible if the inequality is fulfilled with a high, chosen probability of at least $1-\psi_\rho$ i.e., if

$$\mathcal{P}\left\{\left|\Delta\delta\rho_{\,(\hat{a}_0)}\right| \le \mu_\rho\sigma_\rho\right\} \ge 1-\psi_\rho. \tag{4.9}$$

On the other hand, assuming that the deviation of $\hat{a}_0$ is normally distributed as $\varepsilon_{\hat{a}_0} \sim N\left(0,\sigma_{\hat{a}_0}^2\right)$ and taking into account eq. (4.7) we have

$$\mathcal{P}\left\{-z_{1-\psi_\rho/2}\cdot\sigma_{\hat{a}_0} \le \Delta\delta\rho_{\,(\hat{a}_0)} \le z_{1-\psi_\rho/2}\cdot\sigma_{\hat{a}_0}\right\} = 1-\psi_\rho, \tag{4.10}$$

where Z_γ is the γ-quantile of the standard normal distribution. Thus, eq. (4.9) holds if

$$\sigma_{\hat{a}_0} \le \left(\sigma_{\hat{a}_0}\right)_{\max} := \frac{\mu_\rho\sigma_\rho}{z_{1-\psi_\rho/2}}. \tag{4.11}$$

So, we assume that the bias is negligible if the standard deviation of the estimated AP, as calculated from the VCM of the estimated parameters, does not exceed the threshold defined by eq. (4.11) with reasonably chosen negligibility factor and type 1 error probability ψ_ρ. In order to check whether a_0 will be or has been estimated with sufficient accuracy we then just need to check whether the criterion given in eq. (4.11) is fulfilled.

Using similar reasoning we can find equivalent criteria for all APs referring to range. Since the term on the right hand side of eq. (4.11) shows up in the corresponding calculations for each of these APs we introduce the symbol I_ρ as follows:

$$I_\rho := \frac{\mu_\rho \sigma_\rho}{z_{1-\psi_\rho/2}}. \tag{4.12}$$

However, eq. (4.7) shows that the bias of $\hat{a}_0$ has the same impact on all measured distances, and thus the resulting criterion is independent of the actually measured point. This is different for most of the other APs. Typically the impact of the bias of an AP depends on the distance and angles of the respective point. For determining the values of the criteria corresponding to eq. (4.11), we therefore take into account the respective worst effect depending on the distance and angle ranges of the scanner.

We demonstrate this exemplarily for a_3 which models a contribution to the cyclic distance deviation (see e.g., Rüeger, 1990). Following the same procedure as with eqs. (4.7–4.11) we find that the deviation of $\hat{a}_3$ is negligible if:

$$\sigma_{\hat{a}_3} \leq I_\rho \cdot \left(\left|\sin\left(\frac{4\rho}{U_1}\pi\right)\right|\right)^{-1}. \tag{4.13}$$

So, the maximum admissible standard deviation of the estimated AP does not only depend on the quantities chosen above (constituents of I_ρ as of eq. 4.12) but also on the respective range. In order to fulfill the criterion for all possible points within the point clouds obtained using this scanner, eq. (4.13) needs to hold also in the most stringent case i.e., the one where the right hand side is a minimum. This is achieved if

$$\sigma_{\hat{a}_3} \leq \left(\sigma_{\hat{a}_3}\right)_{max} := I_\rho \cdot \left(\left|\sin\left(\frac{4\rho^*}{U_1}\pi\right)\right|\right)^{-1} \tag{4.14}$$

with

$$\rho^* := \arg\max_\rho \left|\sin\left(\frac{4\rho}{U_1}\pi\right)\right|. \tag{4.15}$$

Of course, the minimum of the right hand side of eq. (4.14) is I_ρ and is obtained for all distances for which the magnitude of the sin-term is 1, i.e., for all

$$\rho = (2k+1)\frac{U_1}{8} \tag{4.16}$$

with $k \in \mathbf{N}$. Usually, many such distances are within the specified distance range of the scanner and we can arbitrarily choose any of them as ρ^* for evaluating eq. (4.14). This yields the criterion

$$\sigma_{\hat{a}_3} \leq I_\rho. \tag{4.17}$$

If we only want to use the estimated APs for a specific application with very limited range of distances it may be possible to slightly relax the criterion. In this case we may resort to eq. (4.14) with (4.15) in order to find the appropriate numeric value of the criterion.

Depending on the type of scanner, the observed angles and distances are within specific intervals (see Table 4.1). Table 4.2 lists the criteria for all range APs as resulting from an analysis as above. It also gives the simplified values of the criteria for panoramic and hybrid scanners assuming that the criteria should be fulfilled within the entire working range of the respective scanner.

Table 4.1 Range of observations available with scanners of different type.

	Scanner type	
	Panoramic	Hybrid
Distance	$\rho_{min} \leq \rho \leq \rho_{max}$	
Horizontal angle	$0^\circ \leq \theta \leq 180^\circ$	$0^\circ \leq \theta \leq 360^\circ$
Vertical angle	$-\alpha_0 \leq \alpha \leq 180^\circ + \alpha_0$	$-90^\circ < \alpha_{min} \leq \alpha \leq \alpha_{max} < 90^\circ$

Table 4.2 Criteria (maximum admissible standard deviations) for the range APs with I_ρ as of eq. (16); ρ^*, θ^*, α^* are distance, horizontal and vertical angle for which the respective criterion is a minimum. All APs and criteria are given in meters, except a_1 and its criterion which are dimensionless (m/m).

AP	General case	Panoramic scanner	Hybrid scanner
a_0	I_ρ	I_ρ	I_ρ
a_1	$I_\rho \cdot (\rho^*)^{-1}$	I_ρ/ρ_{max}	I_ρ/ρ_{max}
a_2	$I_\rho \cdot \lvert(\sin\alpha^*)^{-1}\rvert$	I_ρ	$I_\rho/\lvert\sin\alpha^*\rvert$, $\alpha^* = max(\lvert\alpha_{min}\rvert, \lvert\alpha_{max}\rvert)$
a_3	$I_\rho \cdot \left(\left\lvert\sin\frac{4\rho^*}{U_1}\pi\right\rvert\right)^{-1}$	I_ρ	I_ρ
a_4	$I_\rho \cdot \left(\left\lvert\cos\frac{4\rho^*}{U_1}\pi\right\rvert\right)^{-1}$	I_ρ	I_ρ
a_5	$I_\rho \cdot \left(\left\lvert\sin\frac{4\rho^*}{U_2}\pi\right\rvert\right)^{-1}$	I_ρ	I_ρ
a_6	$I_\rho \cdot \left(\left\lvert\cos\frac{4\rho^*}{U_2}\pi\right\rvert\right)^{-1}$	I_ρ	I_ρ
a_7	$I_\rho \cdot (\lvert\sin 4\theta^*\rvert)^{-1}$	I_ρ	I_ρ
a_8	$I_\rho \cdot (\lvert\cos 4\theta^*\rvert)^{-1}$	I_ρ	I_ρ

We obtain similar relations for the horizontal and vertical angles using the quantities

$$I_\theta := \frac{\mu_\theta \sigma_\theta}{z_{1-\psi_\theta/2}} \tag{4.18}$$

and

$$I_\alpha := \frac{\mu_\alpha \sigma_\alpha}{z_{1-\psi_\alpha/2}} \tag{4.19}$$

which account for the different units and standard deviations of the angle observations as

opposed to the distances, and allow using different negligibility factors and type 1 error probabilities, if needed. The results are summarized in Tables 4.3 and 4.4.

A special difficulty arises with b_1 and b_2. When following the above derivation of the criteria, we could never assess the accuracy of b_1 and b_2 as sufficient for application within the entire working range of the scanner. However, this is a wrong conclusion. It is due to the expression of the criteria with respect to polar coordinates and using linear variance propagation: the minimum value of the criterion is 0 if the scanner allows measuring points at α = 90 °i.e. in its vertical axis. We will therefore use a slightly different approach for these two APs.

It can be shown that the impact of a bias $\varepsilon_{\hat{b}_1}$ of $\hat{b}_1$ on the 3D position of the scanned points is bounded by ρ times $\varepsilon_{\hat{b}_1}$ and even less if α is very close to 90 °. Considering that their pact of random deviations of the measured angles on the 3D position is also proportional to ρ, we can give an acceptable cut-off for the vertical angle to assess b_1 based on the maximum measured range which is always limited in a typical indoor field. In our case, the maximum measured range is about 10 m and we choose $\alpha = 80°$ (and $100°$ for a panoramic scanner) as the cut-off. Therefore, the 3D position of the scanned points is bound by $1.7\varepsilon_{\hat{b}_1}$ which is small enough to assess a 3D position. Then we can yield the criterion

$$\sigma_{\hat{b}_1} \leq \left(\sigma_{\hat{b}_1}\right)_{max} = 0.17 \cdot I_\theta \tag{4.20}$$

The same applies to b_2.This has been taken into account in Table 4.3.

Table 4.3 Criteria (maximum admissible standard deviations) for the horizontal angle APs with I_θ as of eq. (18); ρ^*, θ^*, α^* are distance, horizontal and vertical angle for which the respective criterion is a minimum. All AP and criteria are given in degrees, except b_5 and its criterion which are dimensionless (deg/deg).

AP	General case	Panoramic scanner	Hybrid scanner
b_1	$I_\theta \cdot \lvert\cos\alpha^*\rvert$	$0.17 \cdot I_\theta$ $\alpha^* = 80^\circ$ or 100°	$0.17 \cdot I_\theta$ $\alpha^* = 80^\circ$
b_2	$I_\theta \cdot (\lvert\tan\alpha^*\rvert)^{-1}$	$0.18 \cdot I_\theta$ $\alpha^* = 80^\circ$ or 100°	$0.18 \cdot I_\theta$ $\alpha^* = 80^\circ$
b_3	$I_\theta \cdot (\lvert\sin 2\theta^*\rvert)^{-1}$	I_θ	I_θ
b_4	$I_\theta \cdot (\lvert\cos 2\theta^*\rvert)^{-1}$	I_θ	I_θ
b_5	$I_\theta \cdot (\theta^*)^{-1}$	$\frac{I_\theta}{180}\circ$	$\frac{I_\theta}{360}\circ$
b_6	$I_\theta \cdot (\lvert\cos 3\alpha^*\rvert)^{-1}$	I_θ	I_θ
b_7	$I_\theta \cdot (\lvert\sin 4\alpha^*\rvert)^{-1}$	I_θ	I_θ

Table 4.4 Criteria (maximum admissible standard deviations) for the vertical angle APs with I_α as of eq. (19); ρ^*, θ^*, α^* are distance, horizontal and vertical angle for which the respective criterion is a minimum. All AP and criteria are given in degrees, except c_1 and its criterion which are dimensionless (deg/deg).

AP	General case	Panoramic scanner	Hybrid scanner
c_0	I_α	I_α	I_α
c_1	$I_\alpha \cdot (\alpha^*)^{-1}$	I_α/α^*, $\alpha^* = 180^\circ + \alpha_0$	I_α/α^*, $\alpha^* = max(\lvert\alpha_{min}\rvert, \lvert\alpha_{max}\rvert)$
c_2	$I_\alpha \cdot (\sin\alpha^*)^{-1}$	I_α	$I_\alpha/\sin\alpha^*$, $\alpha^* = max(\lvert\alpha_{min}\rvert, \lvert\alpha_{max}\rvert)$
c_3	$I_\alpha \cdot (\sin 3\alpha^*)^{-1}$	I_α	I_α
c_4	$I_\alpha \cdot (\cos 3\alpha^*)^{-1}$	I_α	I_α

4.4.2 Correlation

Estimating the APs from laser scanner observations in a point field typically involves also estimating the external orientation EO of the individual scanner setups and possibly object point coordinates OP along with the APs. Use of the estimated AP values with other scans is only justified if the correlation between APs and the other parameters is negligible. Furthermore, also the correlation among the estimated APs should be low in order to allow assessing them separately, e.g. for studying the temporal stability of the calibration, and to justify application to points which were not used for the estimation. Detailed investigations are required to relate an appropriate threshold of maximum admissible correlation to known parameters of the scanner and of the scanner applications in a similar manner as above. This is beyond the scope of the present paper, so we chose a fixed threshold herein. Based on earlier studies of correlation among the parameters obtained within laser scanner self-calibration (Lichti and Franke, 2005; Lichti, 2007, 2009, 2010; Lichti et al. 2011; Reshetyuk 2009, 2010), we propose to use 0.3 as a threshold for correlations to be considered sufficiently low.

4.5 Configuration requirements

Using the criteria developed above we can investigate how the object points used for calibration need to be spatially distributed in relation to the scanner setup and orientation. We do this first assuming that only one AP or a small subset of APs is to be estimated and all other parameters including EOs and OPs are known. While this is not a realistic scenario for the real calibration, it yields valuable insight into the configuration requirements providing building blocks for the subsequent discussion of a realistic calibration setup. Furthermore this analysis will also show which parameters may not be observable with sufficient accuracy within a system calibration in a practically realizable point field and should rather be determined using a separate (component) calibration therefore.

We base the analysis on the assumption that the point field is established indoors, in a room with dimension 8 x 8 x 4 m^3 as such a room is available for us. However, we will also consider the potential benefits of less restricted spaces where appropriate. Furthermore, we assume that the scanner is operated approximately in an upright orientation and that only negligibly few targets can be located directly above or below the scanner. So we will not take into account

targets at vertical angles below -70 °(and above 250 °for panoramic scanners) or between 80 ° and 100 °even if the scanner is of the panoramic type.

We have chosen $\mu = 0.7$ for all negligibility factors because this means that the bias of the individual estimated AP will increase the mean-square error (MSE) of the corresponding range or angle observation by not more than 20%. We consider it justified to neglect biases of this order of magnitude[2]. Finally, we use a type 1 error probability ψ=5% for all three observation types, so we have

$$[I_\rho \quad I_\theta \quad I_\alpha] := 0.4 \cdot [\sigma_\rho \quad \sigma_\theta \quad \sigma_\alpha]. \tag{4.21}$$

4.5.1 Minimum configuration for individual APs

As before we will first demonstrate the analysis for a_0 and a few more APs in detail and then give the results for all APs.

From a geometric point of view a single OP at an arbitrary, known location within the working range of the scanner would be sufficient to estimatea_0. However, if the criterion given in Table 4.2 is to be met then $\sigma_{\hat{a}_0}$ must be less than $0.4\sigma_\rho$ and thus at least 7 independent TLS measurements to known OPs must be available ($\frac{1}{\sqrt{N}} < 0.4$ for $N \geq 7$).

The 7 measurements can be obtained by either identifying 7 different targets at arbitrary locations within one scan or by using less than 7 targets but at least some of them identified in more than one scan (obtained with equal or with different scanner positions and orientations).

Also when estimating only a_1 theoretically a single OP at an arbitrary, known location within the working range of the scanner would be sufficient. However, the precision of the scale estimate gets better with increased distance. So the OP should be as far as possible from the scanner. Furthermore, we need more than one OP in order to fulfill the requirement given in Table 4.2. If the maximum distance during calibration is 10 m (limited by the dimension of the hall) but the maximum range during later application of the scanner can be up to $\rho_{\max} = 180$ m (e.g.for a Leica HDS7000 scanner) we find numerically, that more than 2500 independent OP measurements would be required for sufficiently accurate estimation of a_1. This shows clearly

[2] For more stringent cases, see discussion in Sec. 4.4.2.

that it is not feasible to calibrate the scanner range scale factor in a typical indoor calibration point field if the estimated AP values are to be used for scans with much longer distances (e.g. outdoors) later on. If the maximum range during calibration is equal to the maximum range during later use of the APs, then at least 7 OP measurements at this maximum range would be needed for sufficiently accurate determination of $\hat{a}_1$. Typically, however, the scale factor will have to be determined separately and introduced as a known or directly observed quantity during the calibration of the other APs within the point field. In this sense, scale factor determination can be carried out using a dedicated scale calibration procedure as established for conventional electronic distance measurement equipment or a dedicated (outdoor) point field with long distances. Highly accurate meteorological corrections will also be needed in the latter case.

Some of the APs come in pairs of sine and cosine terms with the same argument, e.g. a_3 and a_4 or b_3 and b_4. This is a convenient form of representing sinusoidal terms with amplitude and phase to be determined. So, the APs coming in such pairs need to be taken into account simultaneously when assessing their observability. Theoretically, to estimate e.g. a_3 and a_4 with known EOs it is sufficient to have two OPs at different known locations provided that at least the sine values of the two arguments or the cosine values are different and no more than one sine value and one cosine value is 0. So, the distances from the scanner to these two OPs must not differ by an integer multiple of $U_1/2$. The predicted standard deviations of a_3 and a_4 are independent of the horizontal and vertical angles of the targets in this case. The distances slightly influence the quality of the estimates of a_3 and a_4, but this influence is small if they do not differ by approximately an integer multiple of $U_1/2$. Again, in order to achieve sufficient precision fulfilling the criteria given in Table 4.2 we need more than 2 OPs. In fact, at least 14 independent TLS range measurements to OPs with known coordinates must be available to ensure that the errors in the estimated values of a_3 and a_4 are negligible.

When establishing and using a calibration point field, it may be very difficult to distribute a large number of targets exactly at predefined distances from the scanner or at least avoid certain distances. By using slightly more targets, sufficiently accurate estimation of the parameters can also be achieved using targets which are quasi-randomly distributed, i.e. not located at carefully planned distances from the scanner. We carried out a Monte Carlo simulation (using $M = 1000$ runs), assuming that the targets are located at distances uniformly distributed within $[r_{\min}, r_{\max}]$ with $r_{\min}$ and $r_{\max}$ determined by the dimensions of the hall or environment where the calibration is carried out, and $\rho_{\min} \leq r_{\min} \leq r_{\max} \leq \rho_{\max}$. We found out that the resulting

standard deviations of a_3 and a_4 were lower than the threshold of Table 4.2 in 95% of the cases using 22 targets (instead of 14) with distances randomly distributed up to $r_{\max} = 5$ m, 20 targets with distances of up to $r_{\max} = 10$ m (see Figure 4.1).

We have correspondingly analyzed also the individual configuration requirements of all other APs, or pairs of APs where appropriate, from the purely geometric perspective and additionally taking the criteria of Tables 4.2–4.4 into account. The results are given in Tables 4.5-4.7. Where a particular spatial distribution of the OPs is required which cannot easily be assured in a real calibration setup, the results of the MC simulation, also reported in Tables 4.5-4.7, indicate how many OP measurements to points uniformly distributed in range and angles within the volume of the hall are needed to fulfill the requirements with a probability of 95%.

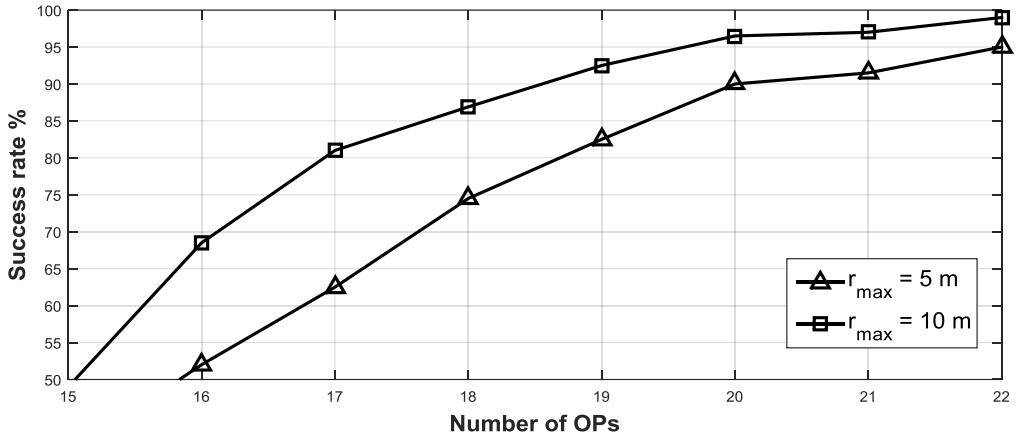

Figure 4.1 Success rates (percentage of simulation runs where the results fulfilled the criteria of Table 2) for a_3 and a_4 with random distribution of OPs for two different maximum ranges (MC simulations with M=1000 runs per number of OPs).

Table 4.5 Minimum configuration requirements for the range APs according to the scenarios discussed in the text (EO known, OP coordinates known, same OP observed in more than one scan counts separately for each scan).

AP	Theoretical requirement	Requirement for sufficiently accurate estimation	95% success rate with quasi-random OP distribution with r_{max}=10 m
a_0	1 OP at arbitrary position	7 OPs at arbitrary positions (distances)	7 OPs
a_1	1 OP at arbitrary position	7 OPs at the maximum range of the scanner	>300 OPs[3]
a_2	1 OP at arbitrary position above or below the scanner's horizon	7 OPs at maximum angular separation from the scanner's horizon	21 OPs
a_3&a_4	2 OPs at arbitrary positions but without distances for which s_1=s_2 and c_1=c_2[4] simultaneously, or for which s_1=s_2=0 or c_1= c_2=0.	14 OPs at distinct distances within $\rho = \frac{2K+1}{8} \cdot U_1$m, $K = 0,1 \ldots .6$ [5]	20 OPs
a_5&a_6	2OPs at arbitrary positions but without distances for whichs_1=$s_2$and c_1=c_2 simultaneously, or for whichs_1=s_2=0 or c_1= c_2=0	14 OPs at distinct distances within $\rho = \frac{2K+1}{8} \cdot U_2$m, $K = 0,1 \ldots .6$	22 OPs
a_7&a_8	2 OPs at arbitrary positions but without horizontal angles for which s_1=s_2 and c_1=c_2 simultaneously, or for which s_1=s_2=0 or c_1= c_2=0	14 OPs at distinct horizontal angles differing by $180°/74$	19 OPs

[3] My simulations terminated with 300 OPs which were still not enough.

[4] Sine (s) and cosine (c) term of first and second point, e.g. s_1=$\sin\left(\frac{2\pi}{U}\rho_1\right)$ for a_3

[5] For pair of a_3 and a_4 the maximum measured range in calibration filed should arrive $1.625 \cdot U_1$m.

Table 4.6 The minimum configuration requirements for the horizontal angle APs according to the scenarios discussed in the text (EO known, OP coordinates known, same OP observed in more than one scan counts separately for each scan).

AP	Theoretical requirement	Requirement for sufficiently accurate estimation	95% success rate with quasi-random OP distribution with r_{max}=10 m
b_1	1 OP at arbitrary position except $\alpha = 90°$	7 OPs at $\alpha = 80°$ (and $100°$ for a panoramic scanner)	>300 OPs[3]
b_2	1 OP at arbitrary position except $\alpha = 90°$	7 OPs at $\alpha = 80°$ (and $100°$ for a panoramic scanner)	>300 OPs[3]
$b_3 \& b_4$	2OPs at arbitrary positions but without horizontal angles for which $s_1=s_2$ and $c_1=c_2$ simultaneously or for which $s_1=s_2=0$ or $c_1= c_2=0$	14 OPs at distinct horizontal angles differing by $180°/74$	20 OPs
b_5	1 OP at arbitrary position except $\theta = 0°$	7 OPs at maximum horizontal angle	>300 OPs[3]
$b_6 \& b_7$	2OPs at arbitrary positions but without vertical angles for which $s_1=s_2$ and $c_1=c_2$ simultaneously or for which $s_1=s_2=0$ or $c_1= c_2=0$	20 OPs of which 31 OPs at $\theta = 64.2857°$ or $115.7142°$ and 14 OPs at $\theta = 38.5714°$ or $141.4285°$ [6]	18 OPs

[6] The sine and cosine terms with b_6 and b_7 have different arguments i.e. 3θ and 4θ. The required number of OPs therefore differs from the one (14) for the other pairs.

Table 4.7 The minimum configuration requirements for the vertical angle APs according to the scenarios discussed in the text (EO known, OP coordinates known, same OP observed in more than one scan counts separately for each scan).

AP	Theoretical requirement	Requirement for sufficiently accurate estimation	95% success rate with quasi-random OP distribution with r_{max}=10 m
c_0	1 OP at arbitrary position	7 OPs at arbitrary positions	7 OPs
c_1	1 OP at arbitrary position except $\alpha = 0°$	7 OPs at $\alpha = 80°$ (or $250°$ for a panoramic scanner)	>300 OPs[3]
c_2	1 OP at arbitrary position except $\alpha = 0°$	7 OPs at $\alpha = 80°$ (and $100°$ for a panoramic scanner)	22 OPs
c_3&c_4	2OPs at arbitrary positions but without vertical angles for which $s_1=s_2$ and $c_1=c_2$ simultaneously or for which $s_1=s_2=0$ or $c_1= c_2=0$	14 OPs at distinct horizontal angles differing by $180°/74$	20 OPs

4.5.2 Minimum configuration for a set of APs

Starting from the previous analysis we will now derive point field configurations for estimating a *set* of APs rather than just an individual one. We will do this for $\{a_0, b_1, b_2, c_0\}$ which is a frequently used subset of the above APs (e.g., Lichti, 2009, 2010; Lichti et al., 2011; Reshetyuk, 2009, 2010). After an initial discussion still assuming known EOs and OPs these assumptions will finally be dropped thus arriving at a realistic calibration scenario and finally at the self-calibration scenario.

From the AP-per-AP analysis above we know that we need

- 7 independent distance measurements to OPs at arbitrary locations for a_0,
- 7 independent vertical angle measurements to OPs at arbitrary locations for c_0,
- 7 independent horizontal angle measurements to OPs at large vertical angle separation from the scanner's horizon but not in the zenith or nadir for b_1, and
- 7 independent horizontal angle measurements to OPs at large vertical angle separation from the scanner's horizon but not in the zenith or nadir for b_2.

This suggests that 14 OPs (7 for a_0, c_0 and b_1, and another 7 for b_2) scanned from a single scanner location and orientation would be sufficient if they are located such that all vertical angles are far from the horizon, e.g. all at about $\alpha = 80^\circ$[7]. However, there are a mathematical and a practical problem requiring some modifications of this starting point. From a mathematical point of view the coefficients of b_1 and b_2 would be (approximately) constant in the parameter estimation model if all vertical angles are (approximately) equal. Consequently, the adjustment model would be rank deficient or poorly conditioned, and b_1 and b_2 could not be separated. From a practical point of view only a limited number of targets can be placed within a certain space, depending on the size of targets. So, for instance assuming that the targets have a diameter of W_t and the ceiling is at a height Δh_{sc} above the scanner, only

$$N_t = \left\lfloor \frac{2\pi \cdot \Delta h_{sc} \cdot \tan(90^\circ - \alpha)}{W_t} \right\rfloor \tag{4.22}$$

targets can be placed along a circle at the ceiling corresponding to a vertical angle α, where $\lfloor . \rfloor$ denotes rounding towards the nearest integer lower or equal to the argument. Both problems

[7] If the scanner is a panoramic scanner, for each vertical angle α mentioned explicitly in this chapter, the corresponding angle $180^\circ - \alpha$ is also meant even if omitted for simplicity.

are solved by placing the OPs at different vertical angles. This comes at the cost of precision and thus we will see that we typically require more than 14 OPs or more than one scan.

Taking into account the practical relevance we subsequently discuss three calibration cases:

(1) The calibration is carried out within a dedicated and permanently established field of OPs with known coordinates, and scanning from pillars with known coordinates such that only the APs and the scanner orientation angles (i.e., 3 of the 6 EOs per scanner setup) are unknown. Optionally, the scanner tilt can be introduced by inclination measurements if the scanner provides them.

(2) The calibration is carried out within a point field as above but the scanner is set up on a tripod for each scan and thus all 6 EOs per scan are unknown.

(3) The calibration is carried out as a self-calibration with all OPs unknown, in addition to the unknown APs and the 6 EOs per scan. In this case, the OPs will likely not even be represented by artificial markers placed within the scene but by feature points which can be identified in several scans.

4.4.5.1 Case (1)

Taking into account the results summarized in Table 4.3 and the above discussion that we cannot place all targets at the same high vertical angle, we expect that the precision and correlation goals can be met if we place slightly more than 14 targets such that some of them are significantly above and some significantly below the horizon. Assuming that points at vertical angles lower than -70 °cannot be measured by the scanner we place the OPs preferably at the intersection of the ceiling and floor with conic shells defined by vertical angles of 80 ° and -70 °. The targets measured by the scanner far away from the horizon will contribute more to low standard deviations of b_1 and b_2 (and thus to keeping the number of OPs low) than the points close to the horizon. However, locating the points at different vertical angles is required to achieve low correlation between APs and EOs and thus to separate them. From early publications some prior knowledge can be exploited to decrease correlations between APs and EOs, and APs and APs, e.g. distributing the targets symmetrically in terms of vertical angle can help to decrease the correlation between b_1 and b_2. Apart from significantly improving the precision of the estimated parameters, adding additional scans also helps to de-correlate the unknown parameters. Discussions of de-correlation strategies can be found in Lichti (2007, 2009, 2010), Lichti et al. (2011) and Reshetyuk (2010).

By numeric simulations we found that the minimum number of OPs allowing to fulfill the precision and correlation criteria at the same time for case (1) is 18. These OPs have to be scanned twice from the same scanner location and with the same scanner orientation, where the scanner should be set up with its secondary rotation axis vertical within $\pm 1^{\circ}$. The configuration is depicted in Figure 4.2. Three of the points are located at a vertical angle of 80 °, 8 at -70 °, 2

at -62 °, and 5 at the horizon. The maximum correlation coefficient is 0.30 (between b_2 and φ) (see Tables 4.10-4.11). The coordinates of the OPs are known and assumed to be measured independently using an instrument with standard deviations of 0.5 mm for distances and 1'' for angles. If the coordinates of the OPs are measured by an instrument with even higher accuracy (e.g. laser tracker) the standard deviations of the given OP coordinates are negligible and the necessary number of OPs can be slightly reduced.

We also carried out an analysis $\mu = 0.3$, i.e. more stringent requirements corresponding to only 5% increase of MSE due to biases of the estimated APs. However, we found that it is hardly feasible to find a point field full filling the requirements and being practically feasible: in this case the analysis showed that 202 OPs and 6 scans are required to meet the criteria.

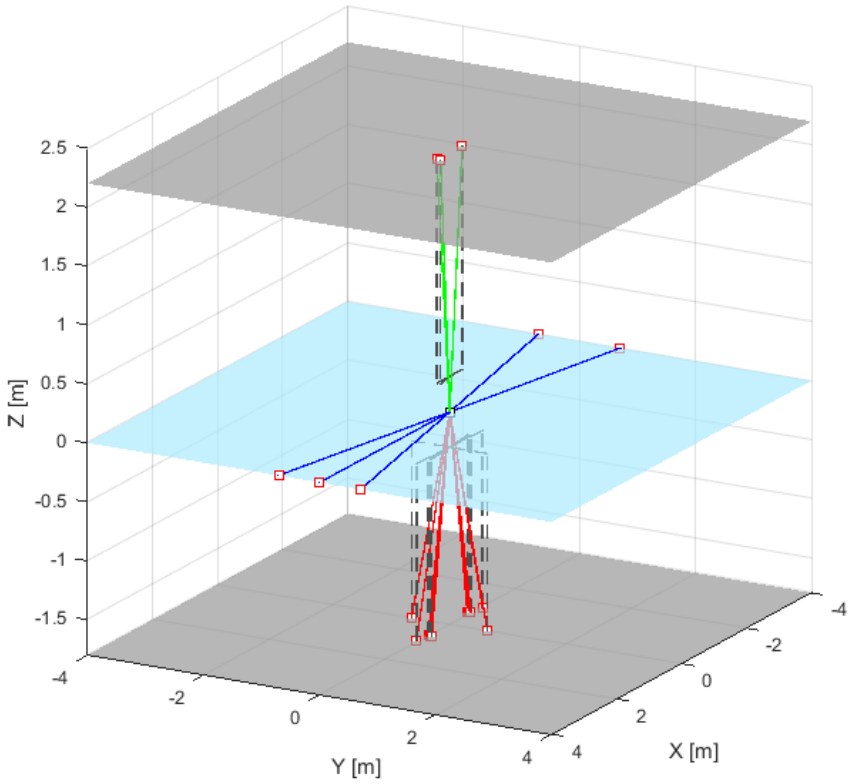

Figure 4.2 Spatial distribution of 18 known OPs (red squares) allowing to estimate the 4APs subset with 2 scans as outlined in the text; scanner assumed 1.8 m (blue plane) above floor, ceiling assumed 4 m above floor; green and red lines represent the laser rays above and below the horizon respectively (colors used for visual purposes only).

4.4.5.2 Case (2)

If the EOs of the scanner, i.e. its position and orientation, are not known beforehand they have to be estimated as further parameters along with the APs. It is to be expected that the configuration depicted in Figures 4.2 will not be sufficient in this case. The precision of the estimated APs will decrease if more parameters are to be estimated using the same observations,

and there may be strong correlations between certain APs and EOs. In addition to the aforementioned strategies for de-correlating parameters, we found that there is the correlation between scanner coordinates and APs, can also be mitigated by adding targets close to the horizon but as far as possible from the scanner.

By numeric simulations we found that the minimum number of OPs allowing to fulfill the precision and correlation criteria at the same time in this case is 23, which are scanned twice from the same scanner location and with the same orientation, using the scanner in the upright position as in case 1. In order to satisfy the precision requirement, we have to move 2 targets (as compared to case 1) from -62 ° to -68 °, install 4 additional ones at -68 ° and 1 more at the horizon. The configuration is characterized in Table 4.8. The maximum correlation coefficient of 0.30, appears between b_1 and x, and between b_2 and ω. More information can be found in Tables 4.10-4.11.

When establishing and using a calibration point field, it may be very difficult to distribute targets exactly at predefined positions from the scanner e.g. because of limited centering capabilities, difficulties to measure or establish a certain instrument height and inclination of the scanner. To account for these uncertainties we again carried out a MC simulation with M = 5000 to find the success rate when we allowed the position of the installed targets to differ slightly from the above theoretical configuration. We modelled the deviations as normally distributed with standard deviations σ_x, σ_y and σ_z. When σ_x and σ_y are both less than 1 mm and σ_z is less than 2 mm we obtain a success rate of 95% using the same configuration as above. Taking into account that particularly the correlations among the parameters are sensitive with respect to the positions of the targets, we relaxed the correlation criterion slightly by allowing correlations up to 0.315 instead of 0.30, and then repeated the MC simulation. In this case, we obtained a success rate of 95% already if σ_x and σ_y are both less than 4 mm; σ_z can even be larger. The calculations showed that vertical deviations (σ_z) have less impact than horizontal ones, see Figure 4.3.

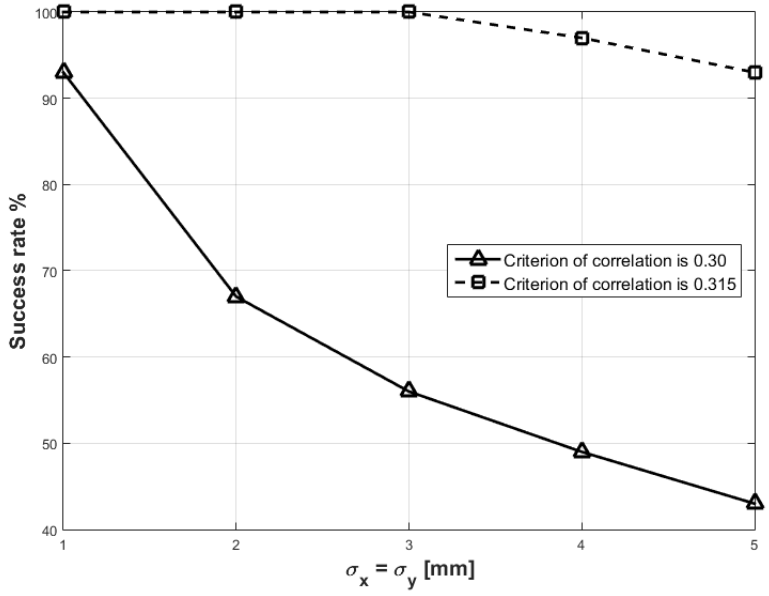

Figure 4.3 Success rates (percentage of simulation runs where the results fulfilled the criteria of Table 2) for target distribution according to table 4.8 but with a certain standard deviation of OP coordinates (MC simulations with M=5000 runs; σ_z= 3 mm).

Table 4.8 Summary of the proposed configuration for case 2.

unknown parameters	$a_0\ b_1\ b_2\ c_0\ \omega_i\ \varphi_i\ \kappa_i\ \ x_i\ y_i\ z_i\ (i = 1,2)$	
OP coordinates	measured independently with standard deviations 0.5mm / 1″	
number of scans	2	
scanner setup 1	location = (0,0,0)	inclination: $\omega = 1^o, \varphi = -1^o$ tertiary rotation angle: $\kappa = 0^o$
scanner setup 2	equal to setup 1	
Number of OPs	23	

4.4.5.3 Case (3)

Finally, we have extended the analysis to a self-calibration scenario where the OP coordinates are treated as unknown parameters which can only be estimated from the laser scans, not supported by independent measurements. One scan will be used to define the geodetic datum and therefore at least 2 scans are required for self-calibration. Taking into account the extraordinary growth in the number of unknown parameters we expect that far more OPs and very likely additional scans are required to assure meeting the criteria set out in sec. 3.

By numeric simulations we found that the minimum number of OPs allowing to fulfill the precision and correlation criteria at the same time is 22, which are scanned 4 times from the same scanner location, with rotation of the scanner about its vertical axis between the scans. In

comparison with case 2 we reduce 1 target at the vertical angle of 80 ° and move the targets from -68 ° close to the horizon which reduces the correlation. In order to keep the precision of the estimated APs and de-correlate the parameters additional scans are carried out. The first and second scans are made without changing the scanner EOs, and the third and fourth scans are taken with the scanner rotated by approximately 180 ° at the same location as before. Like in the previous cases the scanner does not need to be perfectly levelled during the scans. With this configuration the maximum correlation coefficient of 0.3 appears between APs and EOs, in particular between b_1 and b_2, and b_2 and κ (see Tables 4.10-4.11). The configuration is depicted in Figure 4.4 and the full information regarding this configuration is displayed in Table 4.9.

Lichti (2007, 2009) point out that additional inclination observations can mitigate the correlations between scanner orientation (EO angles) and APs. We have carried out extensive numerical simulations assuming a wide range of different standard deviations of the inclination measurements to find out, how strongly they contribute to reducing the calibration effort. However, since we define the datum of the point field – arbitrarily – by the first scan, there is no datum related rank deficiency and the additional inclination observations do not have as significant effects with our configuration assumptions than in Lichti's experiments. Figure 4.5 shows the correlations between APs and inclination after calculation with independent tilt angle observations of various precision. The case "(∞)" corresponds to absence of tilt angle observations. The figure shows that the correlations decrease only with precision of the inclination observations much better than 0.01 °. Scanners currently available do not typically provide inclination measurements of such precision, and, it is hardly feasible to measure the inclination using external sensors. However, these measurements are not needed if a configuration like in Figure 4.4 can be found.

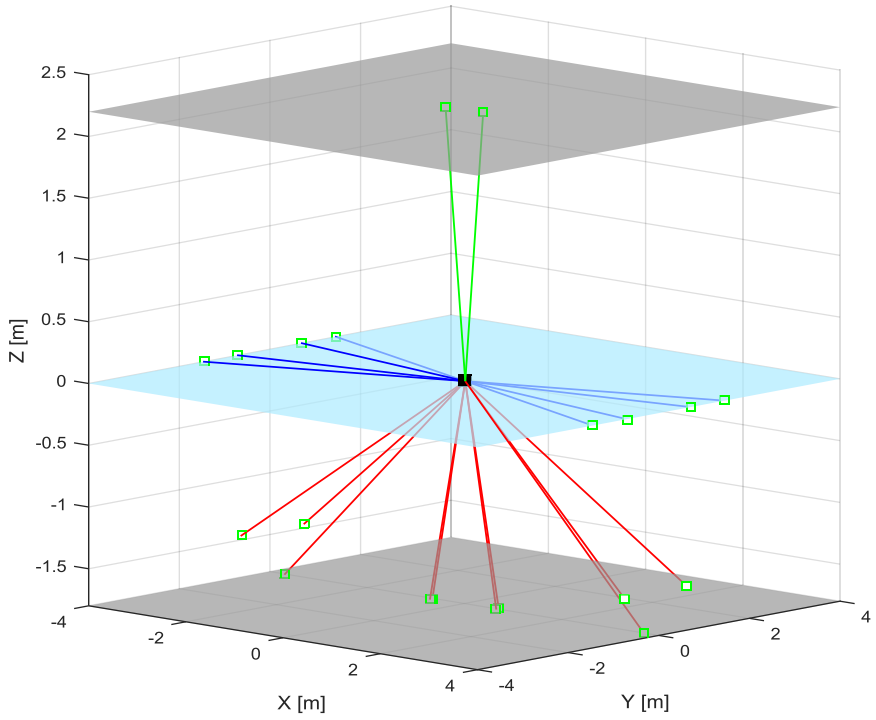

Figure 4.4 Spatial distribution of 22 unknown OPs (green squares) allowing to estimate the 4APs subset with 4 scans from the same positions; scanner assumed 1.8 m (blue plane) above floor, ceiling assumed 4 m above floor; green and red lines represent the laser rays above and below the horizon respectively (colors used for visual purposes only).

Table 4.9 Summary of the proposed configuration for case 3.

unknown parameters	$a_0\ b_1\ b_2\ c_0\ \omega_i\ \varphi_i\ \kappa_i\ \ x_i\ y_i\ z_i\ (i = 1,2,3,4)$	
OP coordinates	unknown	
number of scans	4	
scanner setup 1	location = (0,0,0)	inclination: $\omega = 1^o$, $\varphi = -1^o$ the tertiary rotation angle: $\kappa = 0^o$
scanner setup 2	equal to setup 1	
scanner setup 3	location = (0,0,0)	inclination: $\omega = -1^o$, $\varphi = 1^o$ tertiary rotation angle: $\kappa = 180^o$
scanner setup 4	equal to setup 3	
Number of OPs	22	

Table 4.10 The expected precision of the estimated APs in three cases.

Parameters	case 1	case 2	case 3
a_0	0.2 mm	0.2 mm	0.1 mm
b_1	1.4″	1.5″	1.4″
b_2	1.7″	1.6″	1.7″
c_0	4.3″	4.2″	3.4″

Table 4.11 The highest correlations in three cases.

Case	***Correlation coefficients***
1	$b_2 -$ φ: 0.30 $b_1 - b_2$: 0.25 $b_2 -$ κ: 0.24
2	$b_1 -$ x: 0.30 $b_2 -$ ω: 0.30 $b_2 -$ κ: 0.26 $c_0 -$ φ: 0.21
3	$b_2 -$ κ: 0.30 $b_1 - b_2$: 0.30 $a_0 -$ z: 0.28 $b_1 -$ ω: 0.21

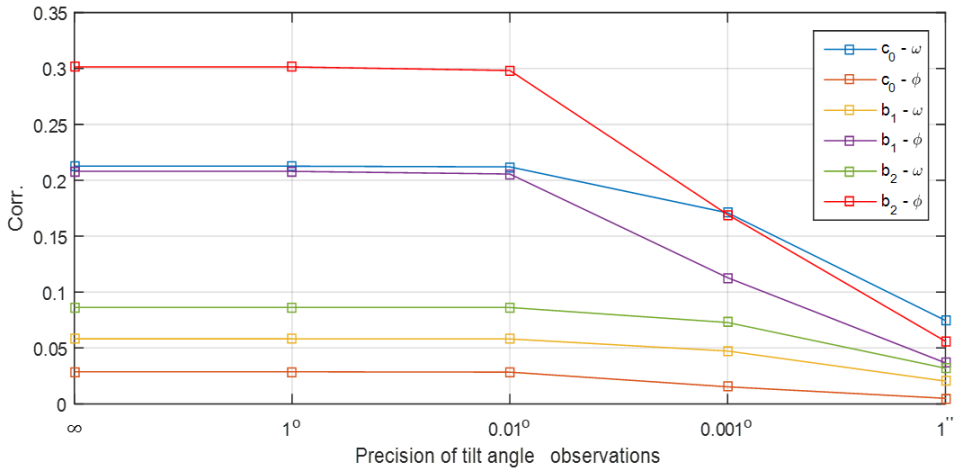

Figure 4.5 Correlations between APs and inclination when using independently observed scanner inclinations.

4.6 Conclusions

The goal of TLS calibration is to obtain parameters (APs) of a deterministic model for improving the quality of the laser scanner measurements by reducing the biases of these measurements. While zero-expectation noise may be further reduced by point-cloud processing e.g. by fitting parametric surfaces to parts of the point clouds or by spatial filtering, uncompensated biases or biases introduced by inappropriate values of APs are not mitigated by such measures. It is necessary, therefore, to achieve highly accurate and sufficiently uncorrelated APs during scanner calibration.

We have derived criteria to predict and assess the quality of the estimated APs by comparing their standard deviations to thresholds derived from the standard deviations of the distance and angle measurements of the scanner and from the (intended) working range of the scanner. Additionally we have proposed a threshold for correlation among the APs and between the APs and any other parameters.

An AP-per-AP analysis has revealed that a fairly high number of TLS measurements and thus object points to be identified within the point clouds is required to estimate the individual parameters sufficiently accurately (7 measurements per AP with ideal point location and more under practical constraints using a specific choice of negligibility factors and probabilities as discussed in section 3). The results have then been used to derive suitable point-field configurations and scanner setups for calibration with a popular subset of 4 APs.

The scenarios covered scanner calibration within an established point field and scanner self-calibration. The proposed configurations are suitable but not necessarily optimum in the sense of calibration effort or accuracy. Future work will thus focus on calibration setup optimization and further practical aspects taking into account larger AP subsets than the one treated herein.

Chapter 5

Surface-based matching of 3D point cloud with variable coordinates in source and target system

Xuming Ge, T. Wunderlich

ISPRS Journal of Photogrammetry and Remote Sensing 111 (2016) 1–12

(The text given here is a revised version)

5.1 Abstract

The automatic co-registration of point clouds, representing three-dimensional (3D) surfaces, is an important technique in 3D reconstruction and is widely applied in many different disciplines. An alternative approach is proposed here that estimates the transformation parameters of one or more 3D search surfaces with respect to a 3D template surface. The approach uses the nonlinear Gauss–Helmert model, minimizing the quadratically constrained least squares problem. This approach has the ability, in terms of separately consider different properties from each surface, to match arbitrarily oriented 3D surfaces captured from a number of different sensors, and at different resolutions. In addition to the 3D surface-matching paths, the mathematical model allows the precision of the point clouds to be assessed after adjustment. The error behavior of surfaces can also be investigated based on the proposed approach. Some practical examples are presented and the results are compared with the iterative closest point and the linear least-squares approaches to demonstrate the performance and benefits of the proposed technique.

Keywords**:** 3D surface matching; surface registration; point cloud; laser scanning

5.2. Introduction

Surface registration is an intermediate, but crucial, step in the three-dimensional (3D) reconstruction of real objects. The terrestrial laser scanning technique is now widely applied in surveying engineering, photogrammetry, and other disciplines as its performance capabilities are advancing rapidly (Ebeling et al., 2011; Gordon and Lichti, 2007). Hundreds of different laser scanners with a great variety of measurement systems are now available; in the current fast-paced laser scanning market, these are updated almost every year. Even products of the same brand may have totally different specifications between different series, e.g. different sensors, different resolutions, different scales and different degrees of precision. An alternative approach to surface registration is therefore required with the ability to handle these different types of sensors, at different resolutions and at different degrees of precision. It is also necessary to analyze the error behavior of surfaces and to assess the registered observations after adjustment.

A cloud of point samples from the surface of an object is typically obtained from two or more points of view in different reference frames. Registration consists of the alignment of the search point set with the template point set by estimating the transformations between the datasets. The registration strategy may differ depending on whether the targets are used to provide the reference points in two clouds of point sets. In terms of whether initial information is required, registration techniques can be classified as either coarse or fine registration. In coarse registration, the main goal is to compute an initial estimate of the rigid motion between two corresponding clouds of 3D points; in fine registration, the goal is to obtain the most accurate solution possible. In fine registration, a higher-quality initial estimate is always required before the calculation. The scope of this paper will be limited to non-target fine registration.

Non-target fine registration is achieved by using a sufficient overlap of the point clouds in different datasets and minimizing the sum of the squares of the distance between the temporarily corresponding points in each iteration. A well-known approach to solving the problem is the iterative closest point (ICP) method (Besl and McKay, 1992; Zhang, 1994; Chen and Medioni, 1991, 1992). The implementation of the ICP method is based on the point-to-point or point-to-plane searching techniques and an estimation of the rigid transformation that aligns the pairs of nearest points in the two datasets. Although the ICP method is a powerful algorithm for non-target registration, it has obvious shortcomings e.g. low time efficiency and easily fall into a local minimum (Fusiello et al., 2002; Gruen and Akca, 2005; Salvi et al., 2007). Several variations and improvements have been introduced to the original version of the ICP concept to improve the algorithm in terms of the transformation accuracy, the convergence properties and the computational cost (Masuda and Yokoya, 1995; Trucco et al., 1999; Greenspan and Godin, 2001; Sharp et al., 2002; Zinsser et al., 2003; Low, 2004; Grant et al., 2012).

Another powerful approach used to complete 3D surface matching originates from the least-squares matching (LSM) technique (Gruen, 1984, 1985a; Ackermann, 1984; Pertl, 1984). Surface patch matching in photogrammetry was first resolved by Gruen (1985a) using this technique. Multiple patch matching with two-dimensional (2D) images using the LSM technique has also been demonstrated by Gruen (1985b). Gruen and Akca (2005) reported a least-squares 3D (LS3D) surface matching approach. This approach was designed for arbitrary 3D surface data and is an extension of 2D least-squares image matching. Akca (2010) enhanced the LS3D approach in terms of the computational cost. However, as Grant et al. (2012) pointed out, the stochastic properties of the normal to the local surface are neglected in the LS3D approach. Gruen and Akca (2005) and Akca (2010) used the LS3D approach based on the generalized Gauss–Markoff model to estimate the transformation parameters with the assumptions that the measurement errors have a simple stochastic character without bias and that only the components of the *target* surface are affected by these errors. The stochastic quantities of the *source* surface were neglected; the effect of these is minor if the *target* and *source* surfaces are generated by the same sensor or method with the same measurement error pattern. However, the principal hypothesis of a particular model matrix in the Gauss–Markoff model is not necessarily satisfied in all applications.

We present here a new approach, an extension of the LS3D approach, to match two arbitrary 3D surfaces. Our proposed approach estimates the rigid-body transformation parameters between two corresponding point clouds using the nonlinear Gauss–Helmert (GH) model. We therefore called the proposed approach the GH-LS3D approach. In this GH-LS3D approach, the nonlinear GH model is introduced to address the so-called weighted total least-squares problem. The iteratively linearized GH model proposed by Pope (1972) was used to adjust error-in-variables (EIV) model problems in arbitrary 3D surface matching problems. By solving the least-squares problem within the GH model, we obtained the solution to the underlying nonlinear problem with a reasonable approximation and some of the potential pitfalls in the iterative adjustment of nonlinear problems were avoided (Pope, 1972). This provided an opportunity to analyze the error behavior of both surfaces and to assess the co-registered surfaces after adjustment.

Section 3 briefly defines the problems of registration and presents the mathematical formulation of the GH-LS3D approach, as well as describing the computational implementation of the proposed approach. Section 4 presents some experimental results based on the non-target fine registration of the point clouds of a terrestrial laser scanner to demonstrate the capabilities of the proposed approach. Some conclusions and further extensions are given in Section 5.

5.3 GH-LS3D surface matching

5.3.1 Statement of the problem and definition

This work concentrated on the pairwise alignment of two meshes, although multi-view registration (Pulli et al., 1997; Pulli, 1999) should also benefit from the approach described here. Let *target* and *source* refer to two partially overlapping scans (surfaces) in two different local coordinate frames. The task of registration is to estimate the transformation parameters that, when applied to the *target* points, best align the *source* and the *target*. Alignment is measured by an error function – for example, the minimization of the sum of the squares of the Euclidean distance. To measure the Euclidean distance, we need to select the correspondence between the *source* and the *target.* The ICP algorithm and its variants provide different schemes for choosing the corresponding points between the *source* and the *target*; they then use the correspondences to calculate the transformation parameters based on a rigid-body transformation. Thus the registration algorithms mainly consist of two steps: (1) matching and selection; and (2) computation of the transformation parameters. In the rest of this paper, we label these two steps *M* and *C*, respectively.

To start the registration algorithm, the program runs the *M*-step to update the *target* by approximations of the transformation parameters and selects the new version of the correspondences from the *source*. Then, in the *C*-step, the program estimates the updated transformation parameters using the correspondences from the last *M*-step. If the estimated transformation parameters do not change significantly in the *C*-step, or if the results reach a termination condition, the iteration will be terminated; otherwise the iteration returns to the *M*-step and uses the last updated transformation parameters instead of the previous values. The schemes to find ideal correspondences in the *M*-step can be applied in parallel in the ICP series and the LS3D approach. In the T-step in the ICP method, the goal function that minimizes the Euclidean distance by least squares is obtained indirectly by estimating and applying rigid transformations. In contrast, the LS3D approach formulates the goal function directly in a generalized Gauss–Markoff model (Gruen and Akca, 2005). The GH-LS3D approach is an extension of the LS3D approach; the main improvement in the proposed approach is in terms of the T-step.

5.3.2 Mathematical model

The *source* and *target* refer to two partially overlapping scans that are digitized point by point in the two different local coordinate frames of the same object. Let $f(x, y, z)$ and $g(x, y, z)$ denote overlapping regions of the object in the *source* surface and the *target* surface, respectively. The problem of 3D surface matching based on the LSM statement is estimating

the transformation parameters to align the target surface $g(x, y, z)$ with the source surface $f(x, y, z)$. If a matching is established between $f(x, y, z)$ and $g(x, y, z)$ then following equation holds:

$$f(x, y, z) = g(x, y, z) \tag{5.1}$$

According to Equation (5.1), the *source* surface elements have corresponding elements in the *target* surface and vice versa. If we then assume that $e(x, y, z)$ is a true error vector between the two surfaces, then we can derive:

$$f(x, y, z) + e(x, y, z) = g(x, y, z) \tag{5.2}$$

Equation (5.2) is the observation equation for LS3D. In GH-LS3D, the error vector $e(x, y, z)$ is divided into $e_f(x, y, z)$ and $e_g(x, y, z)$, which represent the error stemming from the *source* surface and *target* surface, respectively. Thus the observation equation for GH-LS3D is:

$$f(x, y, z) + e_f(x, y, z) = g\{(x, y, z) + e_g(x, y, z)\} \tag{5.3}$$

Equation (5.3) is the condition equation with the measurement errors in all observations. Then the matching problem is to solve the following least squares problem:

$$\sum \left(\| e_f \|^2 + \| g\{e_g\} \|^2 \right) = min \tag{5.4}$$

It is known that, in the Gauss–Markoff model, only the components of the observation vector are affected by the measurement errors and these are calculated by the least-squares technique with a certain design matrix in a normal equation. A standard EIV model is a Gauss–Markoff model with an uncertain design matrix in a normal equation from a geodesy perspective (Fuller, 1987; Fang, 2013). Least-squares within an EIV model is called the total least-squares technique because of its symmetrical adjustment (Fang, 2013). The total least-squares technique within an EIV model can be identified as a special least-squares problem within the nonlinear GH model (Neitzel, 2010). Treating a model as an EIV model rather than a GH model only makes sense if the model is linear – that is, if the design matrix is independent of the estimated parameters in a normal equation and thus is not obtained by linearization. Solving the EIV model using the total least-squares technique rather than treating it as a special GH model only

has a clear advantage if the measurement errors in two kinds of observations are independent and identically distributed. In Equation (5.3), the transformation parameters of the *target* surface $g(x,y,z)$ are obviously variables to be estimated. $g(x,y,z)$ is nonlinear and is related to the estimated parameters; in other words, the function should be linearized and the design matrix should be updated by the estimated parameters. Thus Equation (5.3) will be treated as a special least-squares problem within the nonlinear GH model. It is linearized by Taylor series expansion:

$$g(x,y,z) = g^0(x,y,z) + \frac{\partial g^0(x,y,z)}{\partial x}dx + \frac{\partial g^0(x,y,z)}{\partial y}dy + \frac{\partial g^0(x,y,z)}{\partial z}dz \tag{5.5}$$

with the notation

$$g_x = \frac{\partial g^0(x,y,z)}{\partial x}\,,\; g_y = \frac{\partial g^0(x,y,z)}{\partial y}\,,\; g_z = \frac{\partial g^0(x,y,z)}{\partial z} \tag{5.6}$$

where the terms g_x, g_y and g_z are the values of the first derivatives of the function $g(x,y,z)$ (i.e. the correspond to the three components of the local surface normal, respectively) and $g^0(x,y,z)$ is a roughly aligned search surface. The variables (x,y,z) in $g(x,y,z)$ are functions of the transformation parameters $(t_x\ t_y\ t_z\ \ \omega\ \ \varphi\ \ k)$, which represent the translation vector and the Euler rotation angles. If necessary, a scale parameter can be introduced to change the six-parameter 3D similarity transformation to a seven-parameter 3D similarity transformation. The geometric relationship is established with a six-parameter 3D similarity transformation, differentiation of which gives:

$$\begin{bmatrix} dx \\ dy \\ dz \end{bmatrix} = \begin{bmatrix} dt_x \\ dt_y \\ dt_z \end{bmatrix} + \begin{bmatrix} a_{11} & a_{12} & a_{13} \\ a_{21} & a_{22} & a_{23} \\ a_{31} & a_{32} & a_{33} \end{bmatrix} \begin{bmatrix} d\omega \\ d\varphi \\ dk \end{bmatrix} \tag{5.7}$$

where a_{ij} are the coefficient terms, the expansions of which are given in Akca (2007). We denote the corrections to the parameters by $dp = [dt_x\ dt_y\ dt_z\ d\omega\ d\varphi\ dk]$. We then have:

$$\left.\frac{\partial g}{\partial p}\right|_{g^0,p^0} = [g_x \quad g_y \quad g_z] \begin{bmatrix} dt_x \\ dt_y \\ dt_z \end{bmatrix} + [g_x \quad g_y \quad g_z] \begin{bmatrix} a_{11} & a_{12} & a_{13} \\ a_{21} & a_{22} & a_{23} \\ a_{31} & a_{32} & a_{33} \end{bmatrix} \begin{bmatrix} d\omega \\ d\varphi \\ dk \end{bmatrix} \tag{5.8}$$

where $g\{e_g(x,y,z)\}$ is the error vector from the *target* surface $g(x,y,z)$ and can also be linearized by the Taylor series:

$$g\{e_g(x,y,z)\} = g\{e_g{}^0(x,y,z)\} + \frac{\partial g\{e_g{}^0(x,y,z)\}}{\partial p} \tag{5.9}$$

$g\{e_g(x,y,z)\}$ is the error element, so $\frac{\partial g\{e_g{}^0(x,y,z)\}}{\partial p}$ is a smaller second-order quantity in the calculation and is omitted in the adjustment.

Equation (5.3) can be rewritten as:

$$\Phi(\boldsymbol{e},\boldsymbol{\xi}) = g\{(x,y,z) + e_g(x,y,z)\} - f(x,y,z) - e_f(x,y,z) = 0 \tag{5.10}$$

where $\boldsymbol{\xi}$ represents the unknown parameter vector. Based on the nonlinear GH model (Lenzmann and Lenzmann, 2004) and introducing appropriate approximate values of $\boldsymbol{e}^0$ and $\boldsymbol{\xi}^0$, we obtain the linearized condition equations:

$$\Phi(\boldsymbol{e},\boldsymbol{\xi}) \approx \boldsymbol{B}(\boldsymbol{e}-\boldsymbol{e}^0) + \boldsymbol{A}(\boldsymbol{\xi}-\boldsymbol{\xi}^0) + \Phi^0(\boldsymbol{e},\boldsymbol{\xi}) \tag{5.11}$$

where $\boldsymbol{e} = [\boldsymbol{e_g}, \boldsymbol{e_f}]$, involving the matrices of partial derivatives:

$$\boldsymbol{A} \coloneqq \left.\frac{\partial \Phi}{\partial \xi}\right|_{\boldsymbol{e^0},\boldsymbol{\xi^0}} = \left[\begin{bmatrix} g_x & g_y & g_z \end{bmatrix} \begin{bmatrix} g_x & g_y & g_z \end{bmatrix} \begin{bmatrix} a_{11} & a_{12} & a_{13} \\ a_{21} & a_{22} & a_{23} \\ a_{31} & a_{32} & a_{33} \end{bmatrix}\right] \tag{5.12}$$

$$\boldsymbol{B} \coloneqq \left.\frac{\partial \Phi}{\partial e}\right|_{\boldsymbol{e^0},\boldsymbol{\xi^0}} = \left.\begin{bmatrix} \frac{\partial \Phi}{\partial e_g} & \frac{\partial \Phi}{\partial e_f} \end{bmatrix}\right|_{\boldsymbol{e^0},\boldsymbol{\xi^0}} = [\boldsymbol{B_1} \quad \boldsymbol{B_2}] \tag{5.13}$$

and $\boldsymbol{B_1} = \begin{bmatrix} \boldsymbol{R} & \cdots & \boldsymbol{0} \\ \vdots & \ddots & \vdots \\ \boldsymbol{0} & \cdots & \boldsymbol{R} \end{bmatrix}, \boldsymbol{B_2} = \begin{bmatrix} -\boldsymbol{I} & \cdots & \boldsymbol{0} \\ \vdots & \ddots & \vdots \\ \boldsymbol{0} & \cdots & -\boldsymbol{I} \end{bmatrix}$ where $\boldsymbol{I}$=$\boldsymbol{3 \times 3}$ represents an identity matrix and **R** represents the orthogonal rotation matrix within the Euler angles i.e. $\boldsymbol{R(\omega,\varphi,\kappa)} = \boldsymbol{R_\omega \cdot R_\varphi \cdot R_\kappa}$.

It is then possible to obtain the estimates for the unknowns from the solution of the linear equations system:

$$\begin{bmatrix} \boldsymbol{B_1 Q_g B_1^{\mathrm{T}}} + \boldsymbol{B_2 Q_f B_2^{\mathrm{T}}} & \boldsymbol{A} \\ \boldsymbol{A}^{\mathrm{T}} & 0 \end{bmatrix} \begin{bmatrix} \hat{\boldsymbol{\lambda}} \\ d\hat{\boldsymbol{\xi}} \end{bmatrix} + \begin{bmatrix} \boldsymbol{w} \\ 0 \end{bmatrix} = 0 \tag{5.14}$$

where $\hat{\boldsymbol{\lambda}}$ is a vector of auxiliary "Lagrange multipliers" and the "hats" indicate estimates. $\boldsymbol{Q_g}$ and $\boldsymbol{Q_f}$ represent the cofactor matrices of the *target* surface and the *source* surface, respectively. We will elaborate how to make up those cofactor matrices in the next chapter. In Equation (5.14), $\boldsymbol{w} = -\boldsymbol{B}\boldsymbol{e}^0 + \Phi^0(\boldsymbol{e}^0,\boldsymbol{\xi}^0)$ is the misclosure term, which is calculated from the approximations of the unknowns and residuals and updates them with their corrections.

The residual vector follows from:

$$\begin{bmatrix} \boldsymbol{e}_g \\ \boldsymbol{e}_f \end{bmatrix} = \begin{bmatrix} \boldsymbol{Q}_g \boldsymbol{B}_1^{\mathrm{T}} \\ \boldsymbol{Q}_f \boldsymbol{B}_2^{\mathrm{T}} \end{bmatrix} \hat{\boldsymbol{\lambda}} \tag{5.15}$$

The iteration stops if the corrections to the parameters $d\hat{\boldsymbol{\xi}}$ fall below a certain limit. To stop the *T*-step iteration in GH-LS3D, we respectively select the criteria as 1.0e–4 (m) and 1.0e–5 (rad) for the translations and rotation angles in the later experiments. Here we should point out that the termination criteria of the translation parameters are especially dependent on the nature of the data, e.g., airborne laser scanning data or terrestrial laser scanning data, thus the values of criteria can be self-tuning in the GH-LS3D approach.

5.3.3 Stochastic model

The stochastic model is a crucial part of every weighted least-squares adjustment. The *source* surface and the *target* surface are both obtained from sensors and have their own stochastic model. Contributions to the precision of an individual laser point come from various factors, e.g. the instrument's precision, geometric factors and environmental factors (Bae, 2006; Romsek, 2008). In our later experiments, we only considered the influence from the instrument's precision and the incidence angle of an individual laser point.

The instrument's precision can be obtained from its specification. In our experiments, the data were obtained from laser scanners and prior information is given in the form of the spherical coordinates. Thus the stochastic model should propagate to the Cartesian coordinate system through Jacobian matrices. The covariance matrix of a point can be calculated by error propagation (Mikhail and Ackermann, 1976, p.278ff).

Soudarissanane et al. (2011) showed that the incidence angle, which can take values from 0 to 90°, had a cosine effect on the range precision of the laser points (Ge and Wunderlich, 2015). The incidence angle α of a point can be calculated as:

$$\cos(\alpha) = \frac{\boldsymbol{v} \times \vec{\boldsymbol{n}}}{\|\boldsymbol{v}\| \cdot \|\vec{\boldsymbol{n}}\|} \tag{5.16}$$

where $\boldsymbol{v}$ is laser beam vector and $\vec{\boldsymbol{n}}$ represents a local surface normal vector at a corresponding point. Therefore we considered the effect of the incidence angle in the range precision as:

$$\sigma_r' = \frac{\sigma_r}{\cos(\alpha)} \tag{5.17}$$

where σ_r represents the standard range measurement precision of the instrument and σ_r' represents the corrected precision with the function α.

After the iteration has converged, we obtain:

$$\hat{\sigma}_{0_g} = \sqrt{\frac{\boldsymbol{e}_g^T \boldsymbol{Q}_g^{-1} \boldsymbol{e}_g}{r_g}} \text{ and } \hat{\sigma}_{0_f} = \sqrt{\frac{\boldsymbol{e}_f^T \boldsymbol{Q}_f^{-1} \boldsymbol{e}_f}{r_f}} \tag{5.18}$$

where $\hat{\sigma}_{0_g}$ and $\hat{\sigma}_{0_f}$ are the estimated standard variance factors of the *source* surface and the *target* surface, respectively, and r_g and r_f are the corresponding number of redundancies (Niemeier 2008, p. 324). Then we can further assess the precision of the two registered point clouds:

$$\hat{\sigma}_g^2 = \hat{\sigma}_{0_g} \widehat{\boldsymbol{Q}}_g \text{ and } \hat{\sigma}_f^2 = \hat{\sigma}_{0_f} \widehat{\boldsymbol{Q}}_f \tag{5.19}$$

with

$$\begin{bmatrix} \widehat{\boldsymbol{Q}}_g & \\ & \widehat{\boldsymbol{Q}}_f \end{bmatrix} = \begin{bmatrix} \boldsymbol{Q}_g & \\ & \boldsymbol{Q}_f \end{bmatrix} - \begin{bmatrix} \boldsymbol{Q}_g & \\ & \boldsymbol{Q}_f \end{bmatrix} \cdot \boldsymbol{B}^{\mathrm{T}} \cdot \boldsymbol{Q}_{kk} \cdot \boldsymbol{B} \cdot \begin{bmatrix} \boldsymbol{Q}_g & \\ & \boldsymbol{Q}_f \end{bmatrix} \tag{5.20}$$

$$\boldsymbol{Q}_{kk} = \boldsymbol{N_{bb}}^{-1} - \boldsymbol{N_{bb}}^{-1} \cdot \boldsymbol{A} \cdot \boldsymbol{Q}_{\hat{\xi}\hat{\xi}} \cdot \boldsymbol{A}^{\mathrm{T}} \cdot \boldsymbol{N_{bb}}^{-1} \tag{5.21}$$

$$\boldsymbol{N_{bb}} = \boldsymbol{B} \begin{bmatrix} \boldsymbol{Q}_g & \\ & \boldsymbol{Q}_f \end{bmatrix} \boldsymbol{B}^{\mathrm{T}} \tag{5.22}$$

$$\boldsymbol{Q}_{\hat{\xi}\hat{\xi}} = \boldsymbol{A}^{\mathrm{T}} \cdot \boldsymbol{N_{bb}}^{-1} \cdot \boldsymbol{A} \tag{5.23}$$

where $\widehat{\boldsymbol{Q}}_g$ and $\widehat{\boldsymbol{Q}}_f$ represent posterior cofactors of the *source* surface and the *target* surface. Note that the assessments of the registered point clouds are only carried out with the correspondences between two surfaces after transformation adjustment.

5.3.4 Correspondence search and false detection

The *source* surface and *target* surface are both represented by data points. As in any other registration technique, the corresponding relationship between the *source* surface and the *target* surface will be established in the *M*-step and updated using the last estimated transformation parameters. The methods most often used to find correspondences are the K-nearest neighborhood (Altman, 1992) technique and its variants, e.g. the approximate nearest neighborhood (Arya et al., 1998) technique. To accelerate the searching speed and improve the matching accuracy, more feature information of the objects (e.g. the normalized, intensity, veins, color, curvature and other attributes; Godin et al., 1994, 2001; Godin and Boulanger, 1995; Chua and Jarvis, 1996; Soucy and Ferrie, 1997; Johnson and Kang, 1997; Yang and Allen, 1998) and the sensor acquisition geometry (Park and Subbarao, 2003) are applied in the process of searching correspondence. Based on the different searching schemes, researchers have provided many different variants of the ICP method to complete the point clouds registration. The effect of the searching correspondence strategy is parallel for all the registration techniques in the *M*-

steps because the choosing strategy is expected to favor both the ICP variants and the LS3D variants equally. Thus in this work we did not particularly focus on the consequents from the different searching correspondence strategies and we used the same searching method in both the reference registration methods and the GH-LS3D approach in the later comparative experiments.

The original ICP method always encounters local optimization problems or non-convergence problems. One of the main reasons for this is the appearance of false correspondences in the *M*-step. To address these problems, variants of the ICP method have introduced different strategies to detect outliers. Trucco et al. (1999) implemented a robust ICP (RICP) method that made use of the least median of squares approach. The correspondences with a residual $>2.5\sigma$ were removed and the transformation between both views was computed using only the remaining points; σ was estimated using a robust standard deviation (Rousseeuw and Leroy, 1987, p. 21ff). Zinsser et al. (2003) proposed an RICP method based on outlier thresholding known as the Picky ICP (PICP) algorithm. In the PICP algorithm, only the pairs of correspondences with the smallest distances are used in the motion computation at every iteration. As mentioned earlier, the effects in the searching strategies are parallel in all the registration techniques, so we applied the same robust strategy in both the reference registration methods and the GH-LS3D approach in the comparative experiments.

5.3.5 Computation

The aspect of the GH-LS3D approach that consumes the most computational effort is the search for the correspondences of the *source* surface and the *target* surface. The *T*-step in the GH-LS3D approach is a nonlinear iterative process. In this case, the iteration can be started with initial approximations and can be terminated by a criterion. In fine registration, the initial approximations can be obtained from the results of coarse registration. It is known that the ICP method requires fairly good approximations and that with the LS3D approach this requirement is even stronger (Gruen and Akca, 2005). With the GH-LS3D approach, there is the same requirement for good initial approximations. The values of the first derivatives of the surface in Equation (5.8) can be calculated as the normal vector of a point on the surface. In the iteration, the normal vectors on the *target* surface in Equation (5.8) can be replaced by the corresponding normal vectors on the *source* surface. This alternative has two major advantages. First, the normal vectors on the *source* surface are only calculated once in the first iteration and the same values are then used in the following iterations, whereas the normal vector on the *target* surface should be rotated in each iteration using the last estimated rotation parameters (Gruen and Akca, 2005). Second, the normal vectors on the *source* surface can be regarded as the ultimate directions of the corresponding normal vectors on the *target* surface; therefore using the normal vector on the *source* surface to replace that on the *target* surface can immediately accelerate the convergence rate and improve the registration accuracy.

In the current laser scanner market, terrestrial laser scanners always have high scanning resolutions, which makes it possible to capture more than one million points in one time-scanning point cloud dataset. To accelerate the computation and to avoid memory problems in computer programs resulting from limited random access memory (RAM), we down-sampled the huge raw point cloud using a voxel grid filter. The whole scan volume was divided into a regular 3D voxel grid, and only one point per voxel, computed as the centroid of the points inside a grid cell, was retained.

5.3.6 Implementation

We implemented the GH-LS3D model in *C++*, making use of the open source Point Cloud Library (PCL; Rusu and Cousins, 2011). The reference registration methods, ICP and the linear least-squares (LLS) (Low, 2004), and the proposed GH-LS3D approach were integrated into the PCL environment. The initial values to begin the fine registration and optimized strategies used in the M-step were equal for all the approaches. The point clouds used to test the GH-LS3D approach were all obtained from real scanner sensors (Leica HDS7000 and RIEGL VZ400). The range accuracy of the HDS7000 sensor according to the specification was ≤1 mm in linearity error and the range noise was also ≤1mm when the measurement range was <25 m. The range accuracy of the VZ400 sensor was 5 mm and the precision was 3 mm. More detailed information about the two instruments can be obtained from the manufacturers.

We used two criteria to judge whether convergence had been achieved: (1) if the change in the root mean square error (RMSE) value between successive iterations fell below a threshold of 10^{-4} m; and (2) if the changes in the transformation parameters – namely, the translation vector and the rotation matrix – between successive iterations fell below 10^{-4} m and 10^{-5} rad, respectively. The final RMSE will be calculated by using the same strategy after registration i.e. calculating the distances of the correspondences from the source and transformed target point clouds and then to obtain RMSE of those distances. If convergence had not been achieved after 20 iterations, the registration was terminated. Once the iteration had successfully converged, we used the final estimated transformation parameters to transform the *target* surface to the *source* surface and then compared the overlapping regions between the two point clouds using the 3D Compare module of the Geomagic Studio 2014 software.

5.4 Experimental results and analysis

5.4.1 Indoor application

The first example of an indoor application is the registration of the Karl-Max von Bauernfeind statue in the Geodetic Laboratory of the Technische Universität München. The data were

obtained using the Leica HDS7000 scanner from two different perspectives. For each scan, the scanner was positioned at a distance of 3–4 m from the statue to allow strong overlap (about 90% overlapping regions; see Figure 5.1). The *source* surface and the *target* surface contained 69,889 and 69,741 data points, respectively. The initial approximations in our experiments were calculated from a coarse registration which has been carried out manually by selection of three corresponding point pairs in Geomagic 2014. The ICP model tended to converge after 20 iterations with an RMSE of 2.1041 mm and used 7.1610 s of CPU time. The LLS model performed better than the ICP method in this application in terms of the convergence rate, the registration accuracy and the computational cost. The LLS approach arrived at convergence after seven iterations and used only 2.1550 s of CPU time. The RMSE after matching with the LLS approach was 1.1017 mm. The GH-LS3D approach outperformed the LLS approach in terms of accuracy and speed. With respect to speed, the GH-LS3D approach gave a slightly better convergence rate (six iterations) and CPU time (2.0520 s). The RMSE increased by 38.8% and 68.0% after GH-LS3D matching compared with the RMSE obtained with the LLS and ICP methods, respectively (Table 5.1). Figure 5.2 shows that the RMSE decreased even faster using the GH-LS3D approach. Our registration algorithm worked very well in this experiment, as can be seen from the error images and the residuals histograms in Figures 5.1, 5.3 and 5.4. There was no systematic or dependency pattern in our algorithm. The results obtained with 3D Compare using the ICP, LLS and GH-LS3D matching point clouds are shown in Figures 5.5, 5.6 and 5.7, respectively. The color bar is in meter units. The GH-LS3D approach clearly gave a better 3D Compare result than the other two methods. The differences in the overlapping regions between the *source* surface and the registered *target* surface were mostly <0.5 mm in the GH-LS3D approach, <1.5 mm in the LLS approach and even poorer in the ICP method. Figure 5.8 shows the posterior precision of the *source* surface (left) and the registered *target* surface (right) after adjustment. The color bar represents the posterior standard deviation ($\hat{\sigma}$) in units of millimeters. From Figure 5.8 we can see that, because the scans are indoor and the scanning distances are short (3–4 m), the precision was mostly <1 mm after adjustment, which was comparable with the precision of the original data. The registered *target* surface had a slightly lower posterior precision than the *source* surface and this can be interpreted in terms of the incidence angle and the error propagation in the adjustment.

Table 5.1 Results for the three methods with an indoor example.

Point cloud (Number of points)	algorithms	No. of iterations	RMSE at the final iteration (mm)	Time (s)
Source surface: 69,889 Target surface: 69,741	ICP	20	2.1041	7.1610
	LLS	7	1.1017	2.1550
	GH–LS3D	6	0.6742	2.0520

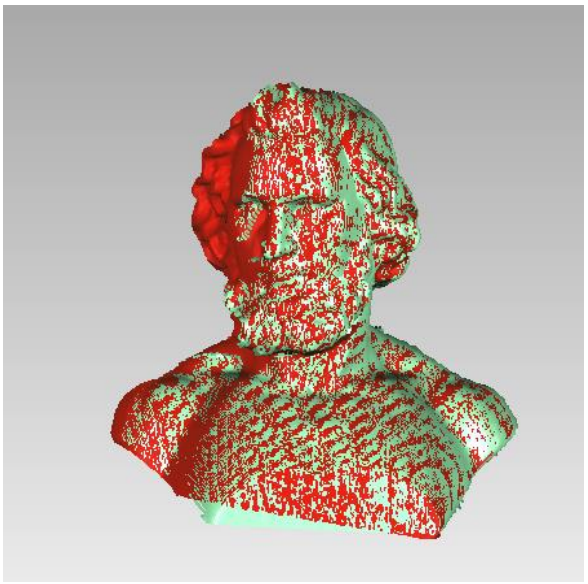

Figure 5.1 View of the final composite surface after matching using the GH-LS3D approach. The source surface is shown in red and the transformed target surface is shown in green.

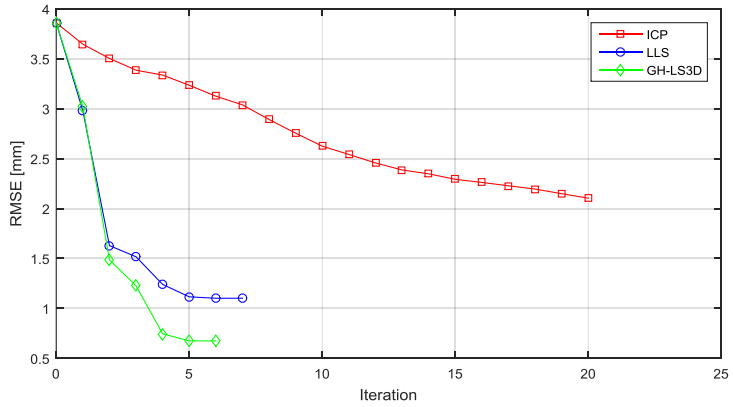

Figure 5.2 Comparison of the rate of convergence for the three different algorithms.

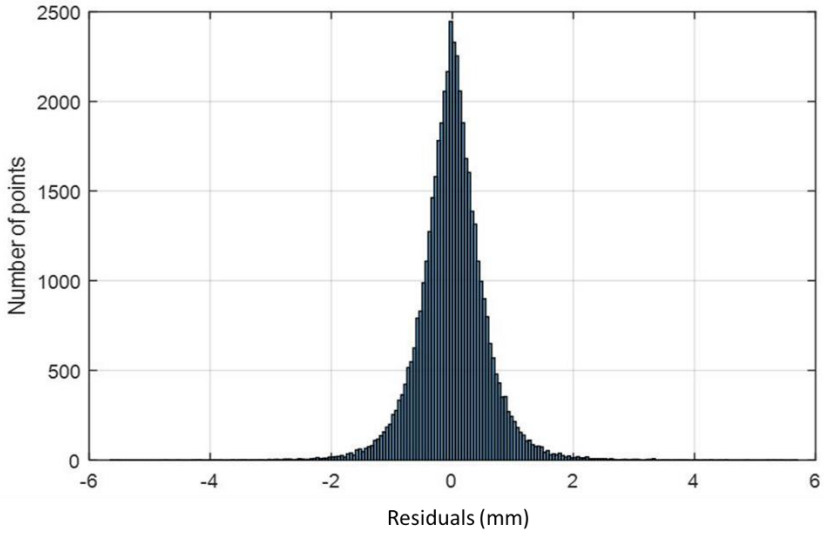

Figure 5.3 Residuals histogram of the target surface in units of millimeters.

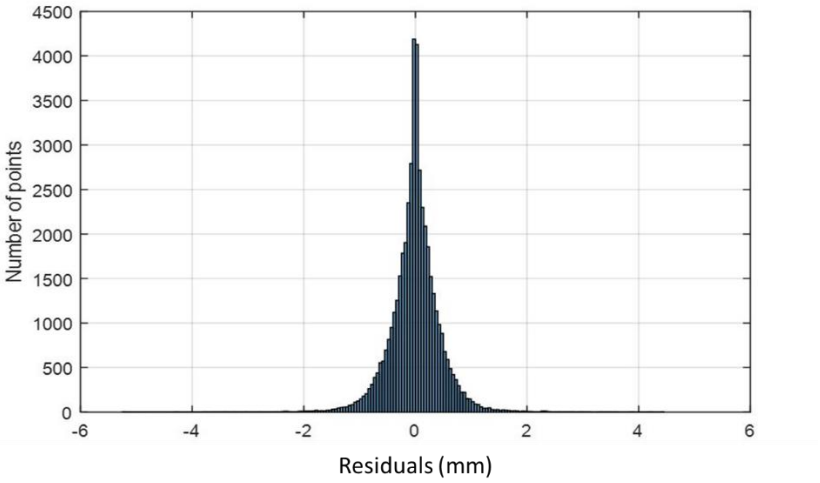

Figure 5.4 Residuals histogram of the source surface in units of millimeters.

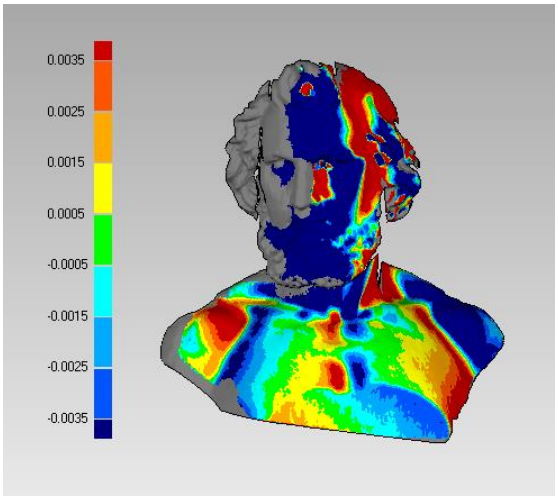

Figure 5.5 Colored residuals between the source surface and the target surface after matching with the ICP method.

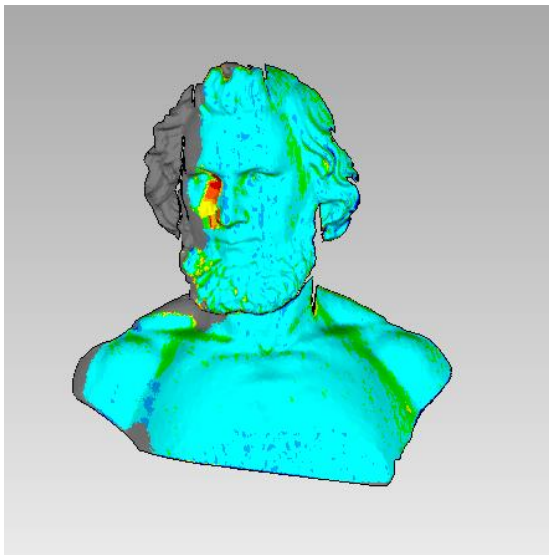

Figure 5.6 Colored residuals between the source surface and the target surface after matching with the LLS approach.

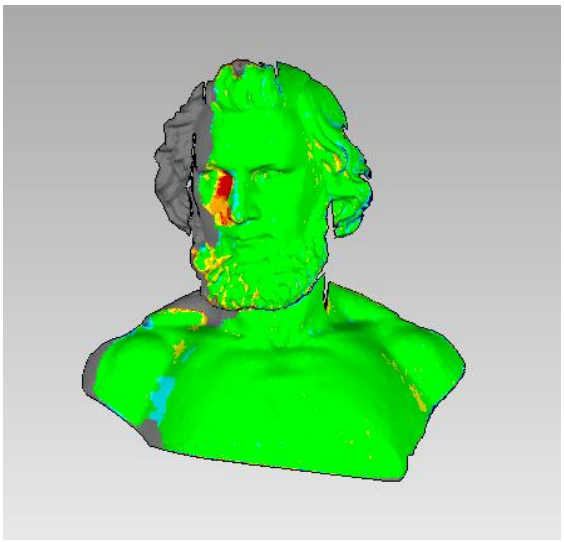

Figure 5.7 Colored residuals between the source surface and the target surface after matching with the GH-LS3D approach.

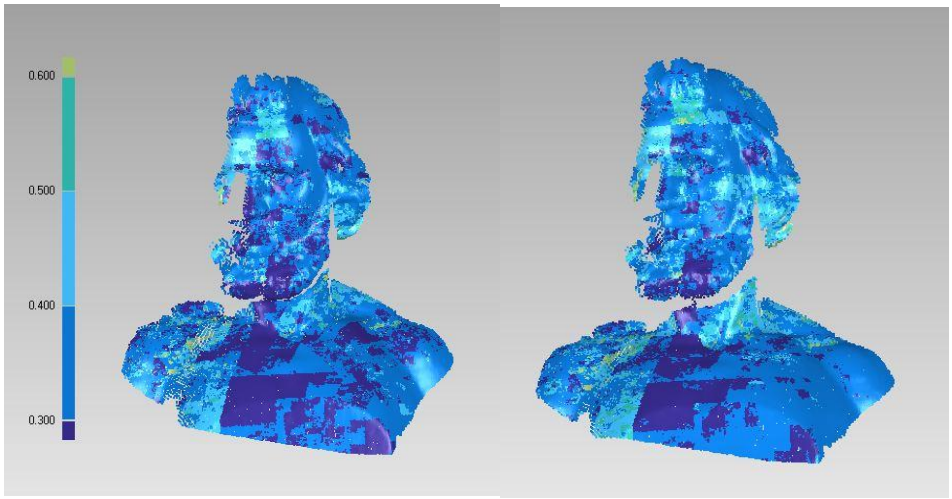

Figure 5.8 Colored posterior precision of the source surface (left) and the target surface (right) after matching with the GH-LS3D.

5.4.2 Outdoor application

The second example is the registration of a corner of the Alte Pinakothek. The volume of the scanned building was about 14×12×18 m. The data were captured from different perspectives using the HDS7000 and VZ400 sensors and contained about 80% overlapping regions (Figure 5.9). For each scan, the scanner was positioned at a distance of 15–20 m from the building to ensure that the points on the top of the building contained acceptable incidence angles. The point clouds captured from the HDS7000 and VZ400 sensor had 5,445,303 and 6,170,071 data points, respectively. Because these data were scanned outside, there were some outliers in the

raw datasets. Thus we removed the same outliers from the raw point clouds before registration for all three methods in the PCL environment. The scans were carried out at high resolution so the raw point clouds were very large. We used a voxel grid size of $\rho = 10$ mm to down-sample the point cloud (Table 5.2). The GH-LS3D approach clearly outperformed the ICP and LLS approaches in terms of the convergence rate and accuracy, in addition to the computational time (Table 5.2). The convergence rate and the computational time of the LLS approach were both about half those required for the ICP method (ten iterations in 306 s in the LLS approach and 20 iterations in 586 s in the ICP method). The GH-LS3D approach was even better than the LLS approach in terms of speed – about seven iterations in 255 s, an increase of about 30 and 16.7%, respectively (Table 5.2). The resulting registrations were too inaccurate using the ICP method, with an RMSE of 27.6971 mm. The LLS approach achieved a considerably higher geometrical registration accuracy, with an RMSE about four times lower (7.1690 mm) than that of the ICP method. The GH-LS3D approach gave a slightly better RMSE at convergence of 6.9603 mm (Table 5.2). Figure 10 shows that, in this experiment, the GH-LS3D approach had a faster convergence rate than other two methods and that the ICP method seemed to meet a local optimization problem after ten iterations.

Figure 5.11, 5.12 and 5.13 show the results with an error color bar [–1 cm, 1 cm] after using 3D Compare with the GH-LS3D, LLS, and ICP matching point clouds, respectively. From Figure 5.11 and 5.12 we can see that on the smooth surfaces of the building the registered errors were both less than ± 1 cm using the GH-LS3D and LLS approaches. Additionally, compared with Figure 5.11 and 5.12 we can find that the LLS approach gave a slightly lower accuracy registration than the GH-LS3D approach. The ICP method gave a registration that was too inaccurate to be used i.e. more than ± 1 cm on most regions of the smooth surface of the building (Figure 5.13). Specifically, when the range of the error color bar was increased to [–15 cm, 15 cm] we can find that the registered errors on the smooth surface of the building were up to ± 8 cm (see Figure 5.15, which uses the same error color bar as Figure 5.14). In addition, the lower walls had a better registered accuracy than the upper walls. This was because the points contained good incidence angles on the lower walls.

On the edges and corners of the building, the registered accuracies were lower (more than ± 1cm) than on the smooth surfaces. This is because the points on the edges and corners did not have such a high quality as those on the plane (Hebert and Krotkov, 1992; Mills and Barber, 2003). When the range of the error color bar was increased to [–15 cm, 15 cm], we can find that the registered errors were less than ± 4.5 cm on the corners and less than ± 11.5 cm on most of the edges using the GH-LS3D approach (Figure 5.14) but which were even better than the LLS approach obtained. Figure 5.15 reflects the fact that the ICP matching results in this experiment were only at the centimeter level and the registered errors on the most regions of the corners and edges were up to ± 15 cm.

Figure 5.16 and 5.17 respective displays the residuals histograms of the VZ400 captured (*source*) surface and Figure 5.17 shows the HDS7000 captured (*target*) surface. The distributions of the residuals on the two surfaces are comparable with the precision of the instruments and the inflection caused by the incidence angles. Figures 5.18 and 5.19 show the histograms for the cosines of the incidence angles of the VZ400-captured surface and the HDS7000-captured surface, respectively. It can be seen that the points had higher-quality incidence angles in the HDS7000 dataset. Figure 5.20 shows the histogram of the posterior standard deviations of two surfaces. Figure 5.20 shows that the HDS7000 captured point cloud had a higher posterior precision, although there were some errors from error propagation (e.g. a down-sampling technique within a voxel grid. As a result of the outside scanning application and relatively long scanning distances, the posterior precision was clearly lower than that of the indoor application. The posterior standard deviations of the HDS7000 sensor were more concentrated in the range 2–6 mm and those of the VZ400 sensor were in the range 4–8 mm (Figures 5.20 and 5.21).

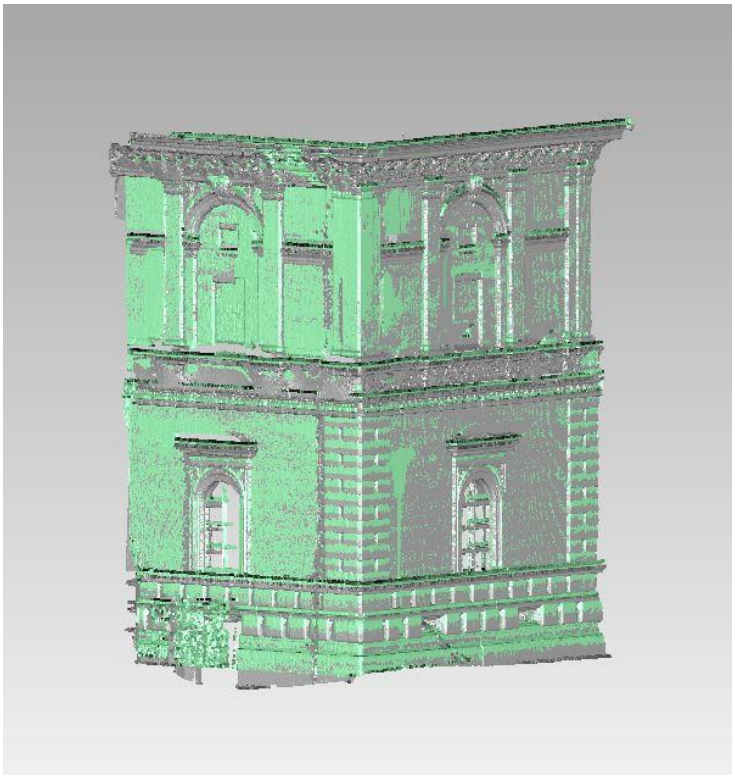

Figure 5.9 View of the final composite surface after matching using the GH-LS3D approach. The source surface is shown as silver and the transformed target surface is shown as green.

Table 5.2 Outdoor example results of the three algorithms.

Point cloud (Numbers of points)	Voxel grid (ρ = 10 mm) (Numbers of points)	Algorithm	No. of iterations	RMSE at the final iteration (mm)	Time (s)
HDS7000: 5,445,303 **VZ400**: 6,170,071	**HDS7000**: 2,918,669 **VZ400**: 3,101,338	ICP	20	27.6971	586.2220
		LLS	10	7.1690	306.2010
		GH–LS3D	7	6.9603	255.3640

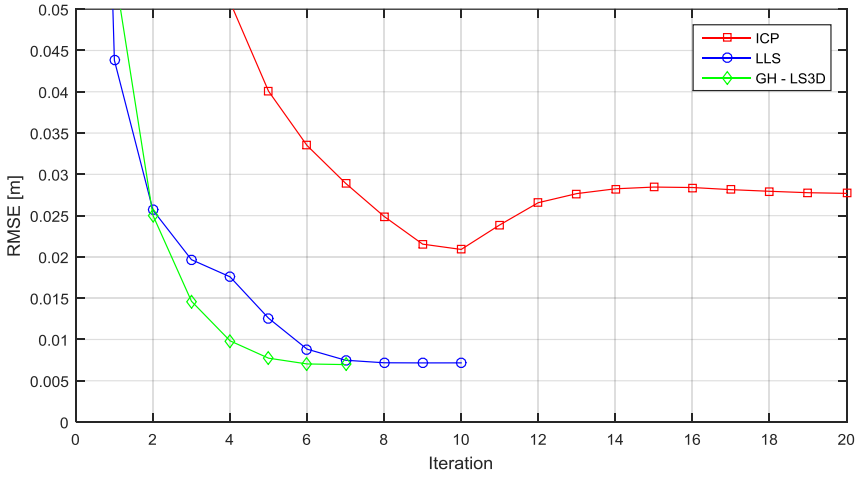

Figure 5.10 Comparison of the rate of convergence for the three different algorithms.

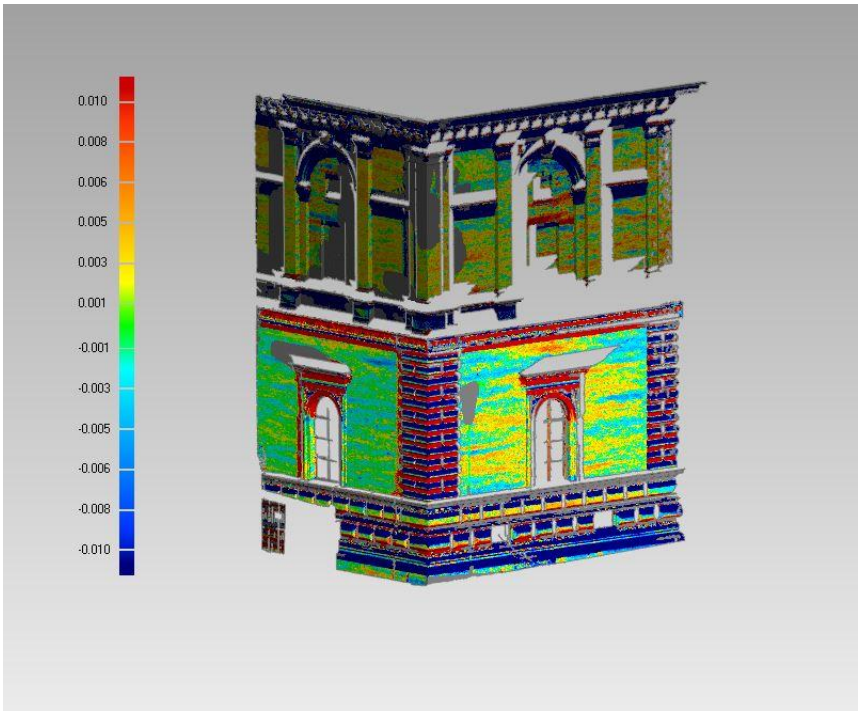

Figure 5.11 Colored residuals between the VZ400-captured surface and the HDS7000-captured surface after matching with the GH-LS3D approach (error color bar range ±1 cm).

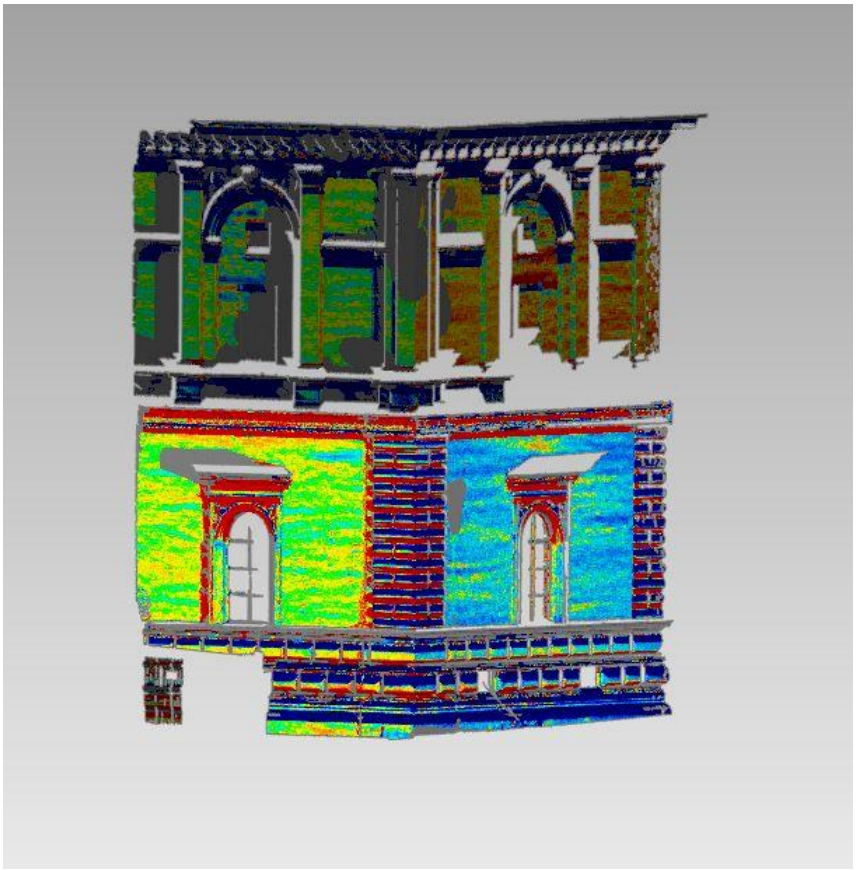

Figure 5.12 Colored residuals between the VZ400-captured surface and the HDS7000-captured surface after matching with the LLS approach (error color bar range ±1 cm).

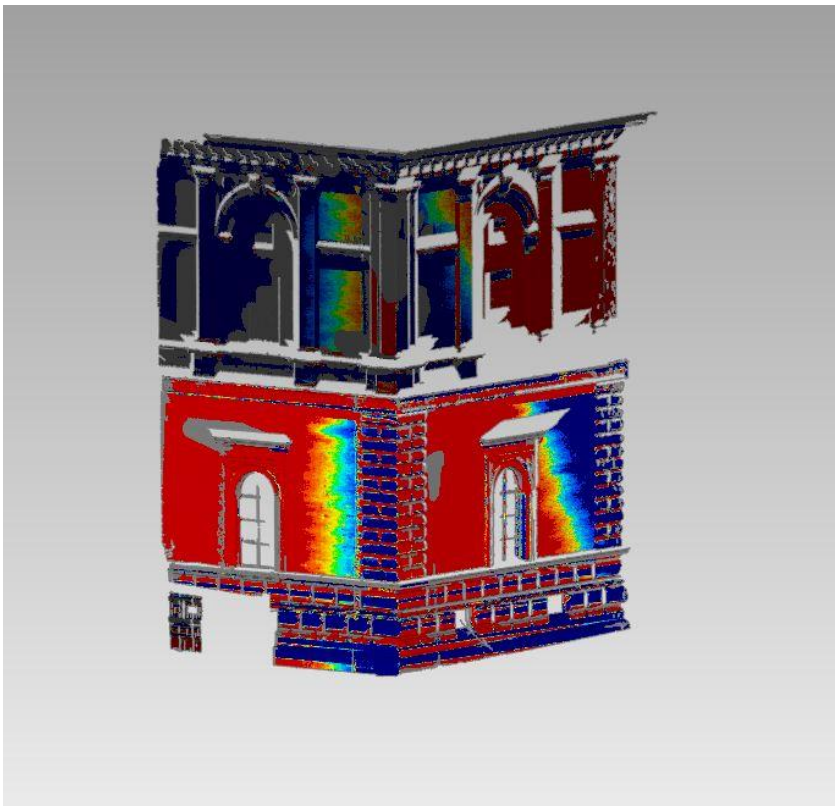

Figure 5.13 Colored residuals between the VZ400-captured surface and the HDS7000-captured surface after matching with the ICP method (error color bar range ±1 cm).

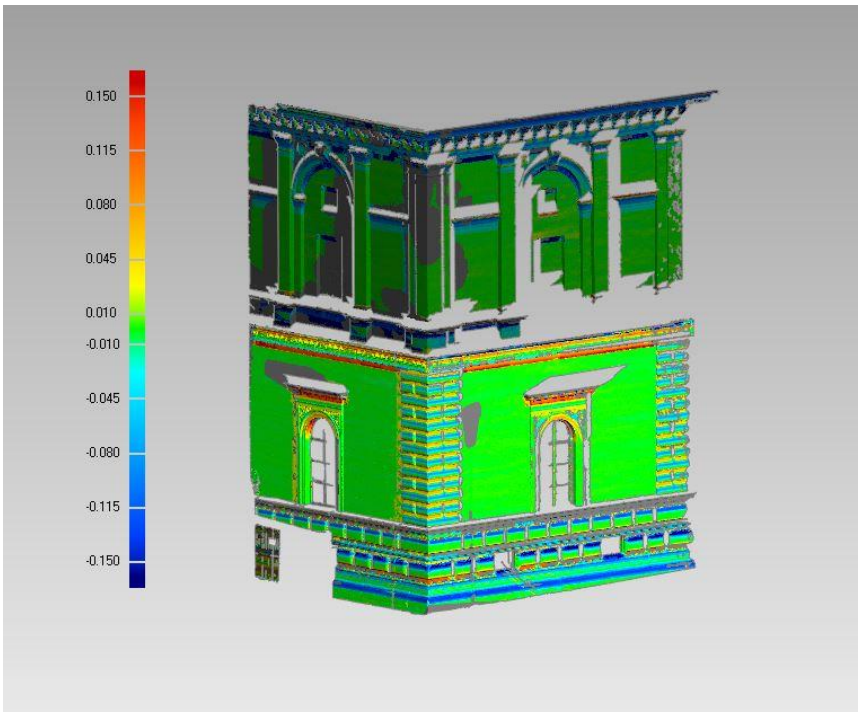

Figure 5.14 Colored residuals between the VZ400-captured surface and the HDS7000-captured surface after matching with the GH-LS3D approach (error color bar range ±15 cm).

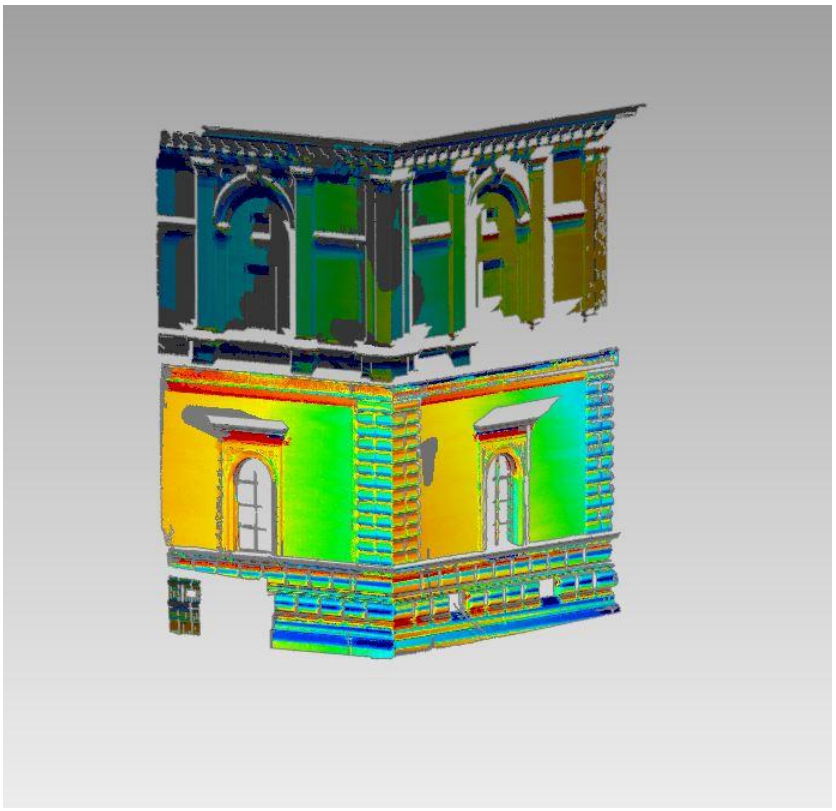

Figure 5.15 Colored residuals between the VZ400-captured surface and the HDS7000-captured surface after matching with the ICP method (error color bar range $\pm$15 cm).

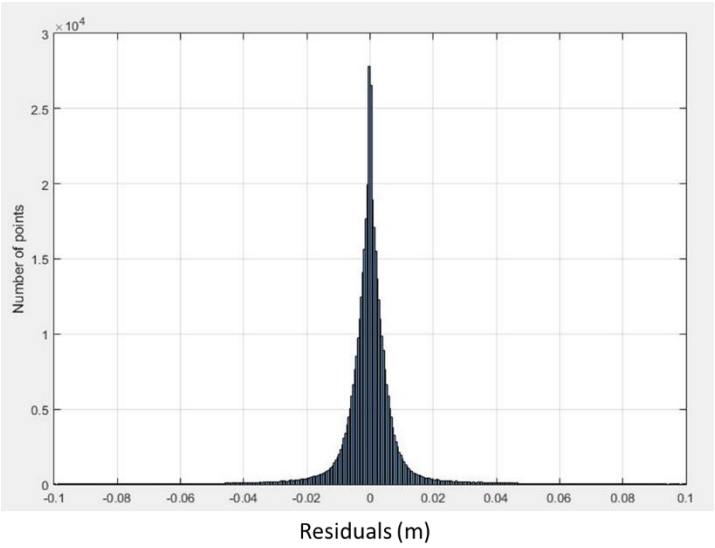

Figure 5.16 Residuals histogram of the VZ400-captured surface in units of meters.

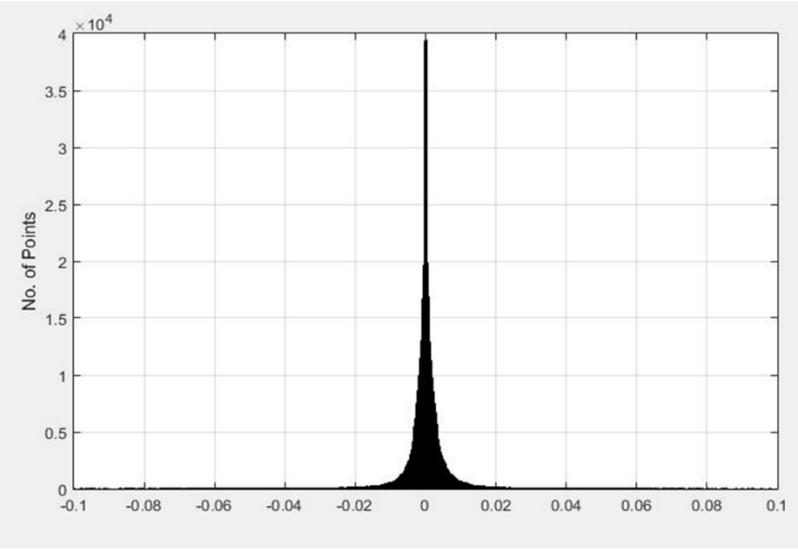

Figure 5.17 Residuals histogram of the HDS7000-captured surface in units of meters.

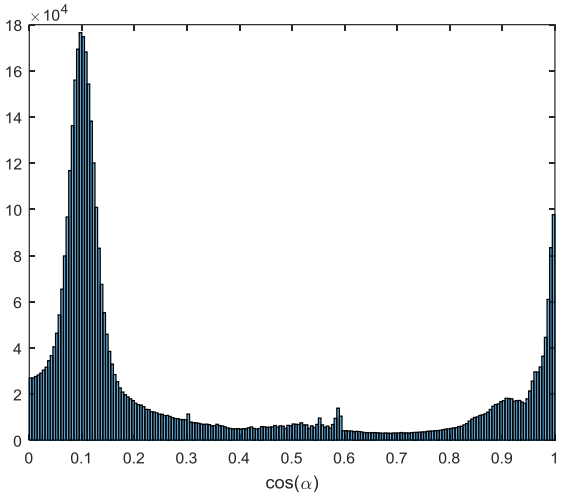

Figure 5.18 Cosine of the incidence angles of the VZ400-captured surface.

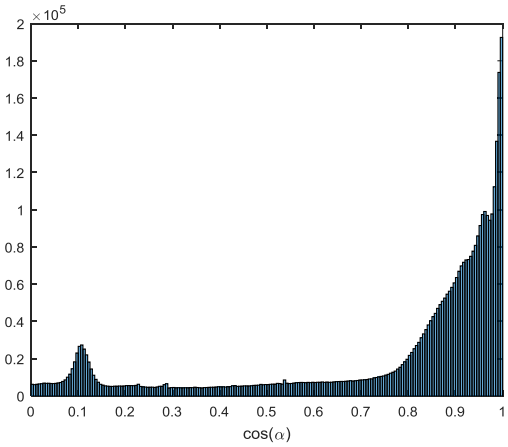

Figure 5.19 Cosines of the incidence angles of the HDS7000-captured surface.

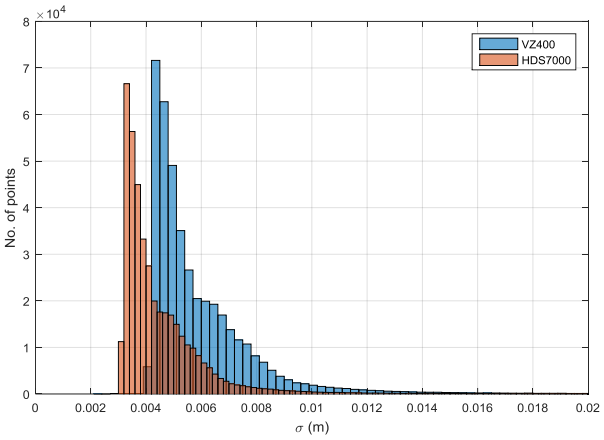

Figure 5.20 The distribution of posterior precision of the two surfaces after adjustment.

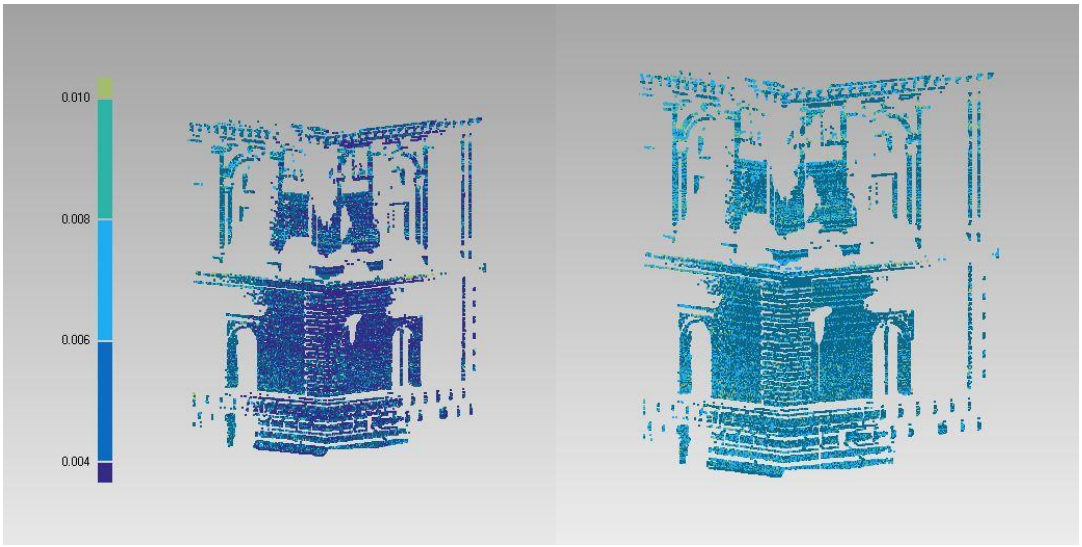

Figure 5.21 Colored posterior precision of the source surface (left) and target surface (right) after matching with the GH-LS3D approach.

5.5 Conclusions and future work

We have paid particular attention to the so-called non-target fine registration and have proposed an alternative approach, the GH-LS3D approach, to match two arbitrary 3D surfaces. The GH-LS3D approach is capable of handling datasets in registration with different degrees of precision, from different sensors and from different perspectives. Different stochastic models can be introduced into the calculation of the GH-LS3D approach and, furthermore, the error behavior of each surface can be independently analyzed using statistical analysis tools after adjustment. The technique can be applied to a great variety of data co-registration problems. It

provides high flexibility for any kind of 3D surface matching, not only in remote sensing and photogrammetry, but also in monitoring and deformation analysis in engineering and industrial measurements. Moreover, based on the power of the GH-LS3D approach numerous applications of the multi-source data fusion can be envisaged in the current measurement data processing.

We have demonstrated the capability of the GH-LS3D approach using indoor and outdoor datasets. In both cases, our results were very positive. The GH-LS3D approach performed better than the ICP and LLS approaches in terms of the convergence rate, registered accuracy and computational time. There are a number of ways to refine and extend the GH-LS3D approach in both the *M*-step and the *C*-step and these will be investigated in further studies.

Chapter 6

Non-rigid registration of 3D point clouds under isometric deformation

Xuming Ge

Journal of ISPRS Journal of Photogrammetry and Remote Sensing 121 (2016) 192–202

(The text given here is a revised version)

6.1 Abstract

An algorithm for pairwise non-rigid registration of 3D point clouds is presented. Specifically, we particularly interest in isometric deformation. Additionally, take into account the inevitable measurement errors in captured point clouds we extend the provided approach to handle more general cases i.e. approximately isometric deformation. The critical step is registration of point clouds at different epochs captured from an isometric deformation surface within overlapping regions. Based on invariant characteristics under isometric deformation, a variant of the four-point congruent sets algorithm is carried out to generate correspondences between two deformed point clouds and subsequently a RANSAC framework is used to complete cluster extraction in preparation for global optimal alignment. Finally, some examples are presented and the results are compared with existed approaches to demonstrate two main contributions of the proposed technique i.e. the success rate for generating true correspondences is up to 90% and the RMSE after the final registration is 2–3 mm.

Keywords: point clouds; non-rigid registration; surface reconstruction; isometric deformation; 4PCS

6.2 Introduction

In addition to its applications to computer vision and computational geometry, three-dimensional (3D) point cloud registration is used in survey engineering, remote sensing and photogrammetry. To date, most registration algorithms have focused on rigid registration, i.e. under the assumption that two (or more) 3D point clouds are related by a rigid transformation. However, with the use of 3D data having become an efficient approach to the representation of different models in a variety of fields, the issue of registration is no longer limited to rigid-body transformations. For example, deformable shape matching has attracted much interest. One application of this is to find the deformation of one object in different epochs. Hence, there is a need to develop non-rigid registration techniques to handle the growing number of 3D registration problems. This paper focus on isometric deformation cases, however, considering the scanning results is limited by a variety of factors (Fang et al., 2015; Ge and Wunderlich, 2015), we extend the proposed method to handle more general cases i.e. approximately isometric deformation.

The dominant algorithms for rigid registration are the iterative closest point (ICP) method (Besl and McKay, 1992; Zhang, 1994; Chen and Medioni, 1991, 1992) and its variants e.g. the robust ICP and the Levenberg-Marquardt ICP (Masuda and Yokoya, 1995; Low, 2004; Grant et al., 2012). Another powerful approach that has been used to achieve rigid registration is the least-squares matching technique (Gruen, 1984) and its extensions (Akca, 2010; Gruen and Akca, 2005; Ge and Wunderlich 2016).

Although there have been considerable advances in rigid registration, the development of non-rigid registration has been relatively tardy. Compared with rigid registration, non-rigid registration faces additional difficulties resulting from the need to account for deformations of the scanned objects at different epochs. There are two key challenges in the non-rigid case: (1) how to establish meaningful and natural correspondences; (2) how to choose an appropriate representation for the deformation and then carry out an optimization. One of the main purposes of this paper is to address these challenges.

We present a novel framework to perform automatic non-rigid registration under (approximately) isometric deformation. An intrinsic geometric approach is adopted in which geodesic distance is exploited as the key factor to establish stable correspondences between two scans. A variant of the four-point congruent set algorithm (4PCS, Aiger et al., 2008) is presented and is applied to the calculations involved in establishing correspondences. With stable correspondences established, we identify the components of the deformation and perform an optimization within a random sample consensus (RANSAC) framework. In order to assess the results of implementing the proposed method, experiments are performed using the TOSCA high-resolution dataset (Bronstein, A.M. et al., 2008).

In summary, our specific contributions include the following:

- Based on geodesic distance, a variant of 4PCS is presented to generate stable correspondences in non-rigid cases.
- A RANSAC framework is designed to extract the rigid body and in preparation for optimization.
- The proposed technique can automatically deal with arbitrary (approximately) isometric deformation registration.

6.3 Related work

The topic of isometric deformation in non-rigid cases is currently attracting great interest both in computer vision and computational geometry. In isometric deformation cases, the geodesic distance is one of the most frequently used intrinsic geometric properties in the search for point correspondences. Berretti et al. (2006) developed a method based on iso-geodesic stripes in which a compact representation was constructed to represent these stripes and quantitatively determine their spatial relationships. Similarly, Mpiperis et al. (2007) used a geodesic polar representation in which each point on the face was characterized by the geodesic distance from the pole (nose tip) and the polar angle. According to the consistency, Huang et al. (2008) generated robust correspondences by calculating the geodesic distances from point to point on the surface. However, one of the shortcomings of using the geodesic distance on point clouds is clearly i.e. instability from topological noise. Landmarks were used to alleviate such problems in Pauly's (Pauly et al., 2005) and Bronstein's (Bronstein et al., 2008) experiments. Tevs et al. (2009) designed a RANSAC framework to find a robust subset of geodesics and then to verify isometric consistency. Interested readers can find further information regarding this topic in Ovsjanikov et al. (2010), Bronstein et al. (2010) and Smeets et al. (2012).

Following the generation of correspondences, different strategies can be adopted to transform two-point clouds and achieve an optimized result. Chang and Zwicker (2008) transformed the clouds using different rigid sub-parts of clusters. Huang et al. (2008) adopted a forward search method (Fleishman et al. 2005) to iteratively combine neighboring clusters until a quality threshold was reached, after which they carried out an energy optimization. Zhang et al. (2008) formulated potential correspondences in a tree and performed a global optimal tree search. A tangent-space technique was used in Tevs et al. (2009) to perform optimization and the authors introduced an intrinsic shape to reduce the sampling cost in three years later (Tevs et al., 2012). At the same year, Sahillioglu and Yemez (2012) used an expectation maximization approach formulated the establishment of shape correspondences as a combinatorial optimization problem. More details of recent developments in non-rigid registration can be found in a comprehensive survey paper by Tam et al. (2013).

Recently using point clouds to handle deformation projects is becoming more and more frequently in the field of geodetic engineering. Gordon and Lichti (2007) developed a modeling strategy to measure vertical deflections of deforming beams by using terrestrial laser scanner observations. The researchers attempted to extract exact positions from a vast of cloud points and then to carry out their calculation. However, information from scanners is always expressed by a huge point cloud of 3D coordinates with a relatively random distribution on the object's surface, preventing a one-to-one correspondence from spots to points. Monserrat and Crosetto (2008) used a rigid registration method to detect the deformation of objects and a similar strategy was also developed by Wujanz et al. (2013). But, only limited information (i.e. orientation and translation of overall structure) can be gained from rigid registration. More information of point clouds application for deformation monitoring of structures in the field of geodetic engineering can be found in Mukupa et al. (2016).

6.4 Methodology

6.4.1 Overview

As scanning resolutions are becoming higher and higher, and input raw point clouds potentially consist of millions of points, it is required to down-sample huge raw point clouds before registration (Klein et al., 2010; Diez et al., 2012). The proposed method consists of three key steps. First, we start the algorithm by extracting feature points. The feature point subset should represent as much as possible of the 3D information about the object, especially the deformed part. Based on the generated feature point subset, we can further find four stable correspondences on both clouds in preparation for the later calculation. Second, we compute geodesic distances from the feature points to the four key points on each surface. After obtaining all the required geodesic distances, we use a variant of the 4PCS method to establish correspondences between the two clouds. In order to ensure the reliability of the correspondences, incorrect correspondences need to be removed by some robust strategies, which we develop subsequently. Next, we put all the obtained correspondences into a RANSAC framework to find independent rigid clusters between two point clouds and then to implement a rigid registration for each corresponding clusters. After this procedure, the method executes a further strategy to detect whether there remains potential rigid corresponding regions that are not in any clusters. The framework of the proposed method is illustrated in Fig. 6.1.

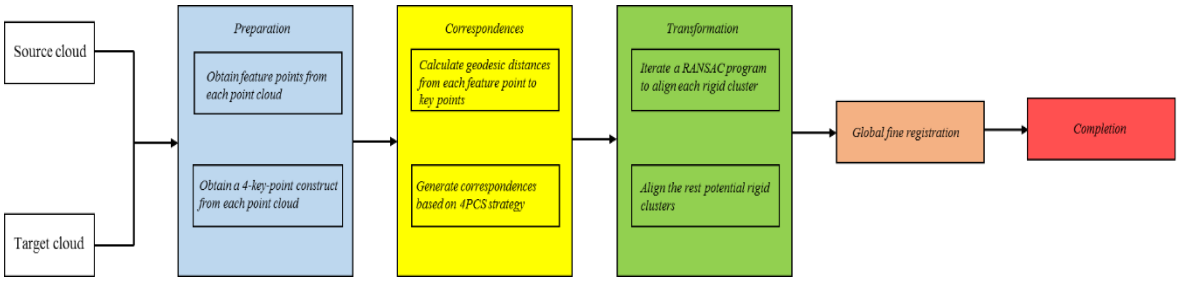

Figure 6.1 Overview diagram of the proposed framework for non-rigid registration.

6.4.2 Feature Extraction

Theoretically, any feature extraction technique can be employed in this step, for example intrinsic shape signature (ISS) (Zhong, 2009), heat kernel signature (HKS) (Sun et al., 2009), spectral feature (Hu and Hua, 2009) or fast point feature histograms (FPFH) (Rusu et al., 2009). Here we use a multilevel ISS method to obtain the feature points subsets on the source cloud (P_s) and the target cloud (P_t). The different search levels are based on the density ρ of the point cloud. The goal of this step is to generate feature points necessary to represent as much as possible of the 3D information about the scanned object. We can then obtain the corresponding subsets $\widehat{P_s}$ and $\widehat{P_t}$ for the source and target clouds, respectively. Figure 6.2 shows the feature extraction results on two Cat datasets, where we have used two levels (1ρ and 0.5ρ) to perform the ISS algorithm.

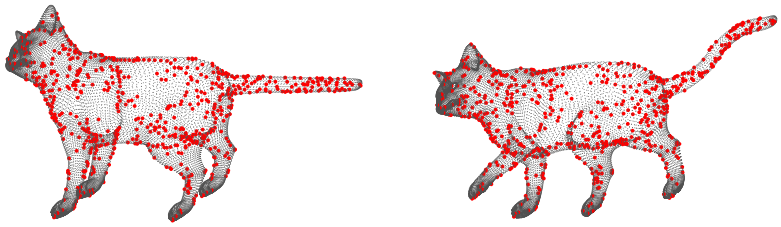

Figure 6.2 Feature points extraction results on two Cat datasets with different poses.

After generating the two subsets $\widehat{P_s}$ and $\widehat{P_t}$, we need to calculate the four key corresponding points from the two point clouds. In this paper, we adopt the HKS algorithm to obtain these points (see Fig. 6.3). The goal of this process is to prepare for the later search for correspondences, so we will discuss these four key corresponding points in the next section.

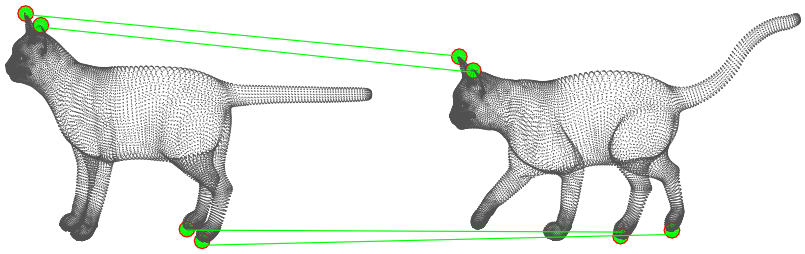

Figure 6.3 The four key corresponding points on the two Cat datasets with different poses.

6.4.3 Correspondence computation

The **geodesic distance** between two points in a curved space is the distance along the shortest path that can be found between these points and is invariant under an isometric deformation (Tenenbaum et al., 2000). Our algorithm makes heavy use of geodesic distances on the scanned surface to generate stable correspondences between P_s and P_t. As the data of point clouds are discrete, we usually need to generate a triangulation mesh on the scanned object using discrete coordinates. After obtaining this mesh, we employ the improved Dijkstra algorithm (Deng et al., 2012) to calculate the geodesic distances from the feature points to the four key points on each surface. We thus obtain four geodesic distance subsets $\{\mathcal{L}_s^1, \mathcal{L}_s^2, \mathcal{L}_s^3, \mathcal{L}_s^4\}$ on P_s and four subsets $\{\mathcal{L}_t^1, \mathcal{L}_t^2, \mathcal{L}_t^3, \mathcal{L}_t^4\}$ on P_t. The superscripts here indicate the key points and the subscripts indicate the point clouds; for example, $\mathcal{L}_s^1$ represents the subset comprising the geodesic distances from all the feature points to the first key point on the source cloud.

4PCS (Aiger et al., 2008) is a global rigid registration algorithm for 3D point sets. The goal of 4PCS is to find the transformation that provides the best alignment as measured by the greatest amount of overlap between the source point cloud and the target point cloud. The algorithm is based on finding a set of four-point bases in the source cloud that are congruent to a four-point base selected from the target cloud. Letting $X = \{\boldsymbol{a}, \boldsymbol{b}, \boldsymbol{c}, \boldsymbol{d}\}$ be four coplanar points selected from the target cloud, if those four points are not all collinear, then the line $\boldsymbol{ab}$ intersects the line $\boldsymbol{cd}$ at an intermediate point $\boldsymbol{e}$. Two ratios can then be defined when we have a four-point base constructed from two intersecting pairs:

$$r_1 = \|\boldsymbol{a} - \boldsymbol{e}\| / \|\boldsymbol{a} - \boldsymbol{b}\|$$

$$r_2 = \|\boldsymbol{c} - \boldsymbol{e}\| / \|\boldsymbol{c} - \boldsymbol{d}\| \tag{6.1}$$

These ratios are invariant under affine transformations (Huttenlocher, 1991) and therefore act as invariants constraining the search for congruent four-point bases in the source cloud. More details about the properties of 4PCS and its application to rigid registration can be found in Aiger et al. (2008), Theiler et al. (2014), Mellado et al. (2014) and Mohamad et al. (2014, 2015).

We will develop a variant of 4PCS (i.e. 4PCS based on geodetic distances, GD-4PSC) to find correspondences in non-rigid registration. In the non-rigid case, we first need to find a four-point construct on both point clouds by feature extraction (see Fig. 6.2). In order to apply our algorithm, one condition must be satisfied, namely that the pair of four key points be corresponding points (i.e. the first key point on P_s must be the point corresponding to the first key point on P_t). To ensure that the condition is satisfied, we will verify the geodesic distances between each pair of points. Once four such key points on both P_s and P_t have been obtained, we can connect each feature point to the four key points by a geodesic path on its own surface, thereby obtaining the corresponding subsets $\{\mathcal{L}_s^1, \mathcal{L}_s^2, \mathcal{L}_s^3, \mathcal{L}_s^4\}$ and $\{\mathcal{L}_t^1, \mathcal{L}_t^2, \mathcal{L}_t^3, \mathcal{L}_t^4\}$. Now, we can treat each feature point as an intermediate point in the corresponding construct formed from the four key points connected by geodesic paths. In order to distinguish this from the rigid case, we shall henceforth designate these intermediate points as geodesic intermediates. Two four-key-point constructs, $X_t = \{\boldsymbol{a}_1, \boldsymbol{b}_1, \boldsymbol{c}_1, \boldsymbol{d}_1\}$ and $X_s = \{\boldsymbol{a}_2, \boldsymbol{b}_2, \boldsymbol{c}_2, \boldsymbol{d}_2\}$, are established on P_t and P_s, respectively (see Fig. 6.3). Given a point $\boldsymbol{e}_1$ as a geodesic intermediate on P_t (see Fig. 6.4), four geodesic distances and two ratios can be defined as follows:

$$d_{a_1}^t = \|\boldsymbol{a}_1 - \boldsymbol{e}_1\|_g$$

$$d_{b_1}^t = \|\boldsymbol{b}_1 - \boldsymbol{e}_1\|_g$$

$$d_{c_1}^t = \|\boldsymbol{c}_1 - \boldsymbol{e}_1\|_g$$

$$d_{d_1}^t = \|\boldsymbol{d}_1 - \boldsymbol{e}_1\|_g$$

$$r_1^t = d_{a_1}^t / d_{b_1}^t$$

$$r_2^t = d_{c_1}^t / d_{d_1}^t \tag{6.2}$$

where $\|.\|_g$ represents the geodesic distance. These geodesic distances and ratios are preserved under isometric deformation and therefore act as invariants to constrain the search for a point $\boldsymbol{e}_2$ in P_s (see Fig. 6.4). If the selected point $\boldsymbol{e}_2$ satisfies

$$\left\|d_{i_1}^t - d_{i_2}^s\right\| \leq \varepsilon_d, \quad i = a, b, c, d$$

$$\left\| r_j^t - r_j^s \right\| \leq \varepsilon_r, \quad j = 1, 2 \tag{6.3}$$

where ε_d and ε_r are given thresholds, then we will put it into the correspondence candidate subset of $\boldsymbol{e}_1$. Now, for each candidate, we can compute four root mean square errors (RMSE) for geodesic distances and two RMSE for ratios and then perform a separate normalization on each kind of RMSE. After that, we can combine the two kinds of RMSE to finally obtain a total RMSE, $\mathcal{T}_{RMSE}$. For each candidate, a weight can be defined using its corresponding $\mathcal{T}_{RMSE}$, i.e.

$$\mathcal{W}_i = \exp\left(-\frac{(\alpha \mathcal{T}_{RMSE})^2}{2\sigma^2}\right) \tag{6.4}$$

where α is a significance factor. Finally, we select the candidate with highest weight as the corresponding point of $\boldsymbol{e}_1$. Based on the proposed algorithm, we can establish stable corresponding relationships between P_t and P_s. Figure 6.5 shows the results of a correspondence computation for different poses.

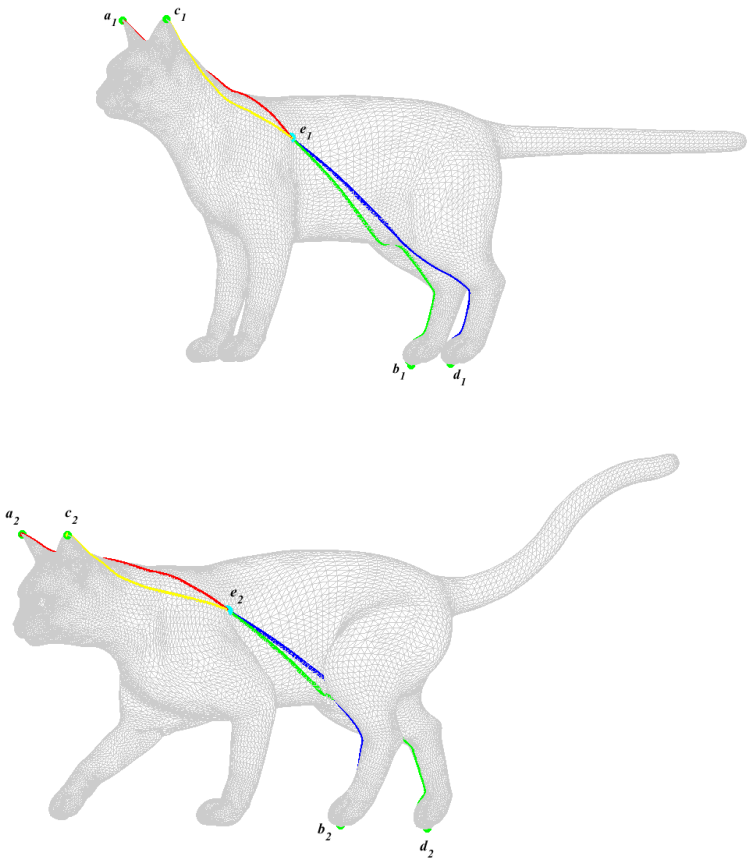

Figure 6.4 Finding correspondences using a variant of 4PCS in a non-rigid case.

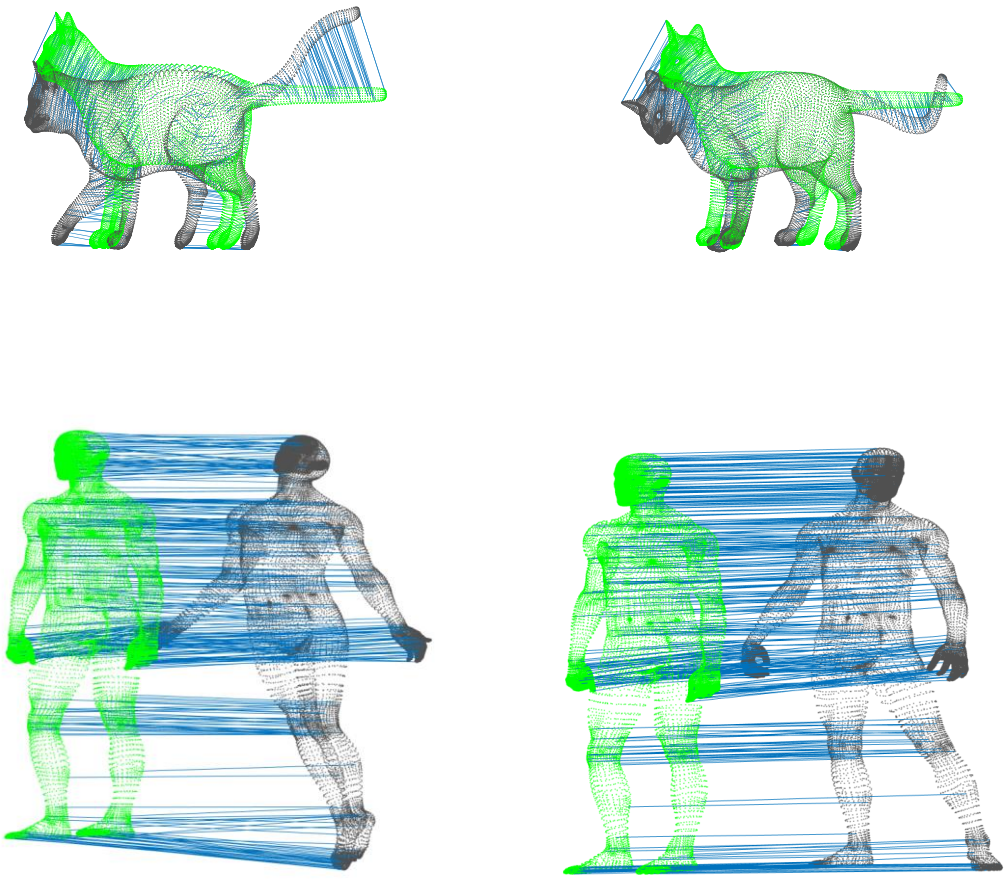

Figure 6.5 Correspondence computation using the proposed algorithm.

Topological noise is one of the main factors making geodesic distances unreliable (Tevs et al. 2009) and thereby causing the correspondence process to fail. Two key factors that influence topological relations are the qualities of the point clouds and of the triangulation mesh. We shall not go into detail about these two issues here, and when executing our algorithm, we shall assume that the point clouds and the triangulation mesh are both of acceptable quality. However, white noise is inevitably present in all scanning programs and may also influence the stability of geodesic distances. If geodesic distances are not globally stable, we can split the point cloud into different subsets and subsequently carry out separate non-rigid registrations. The two color maps in Fig. 6.6 show the differences between geodesic distances from the same point to all other cloud points with different poses. It can be seen from the color coding that we can segment each point cloud into different regions based on geodesic distance. The dashed red boxes in Fig. 6.6 give an example of the corresponding segmentations. After generating the corresponding segmentations, we can implement the proposed algorithm independently on each segmentation.

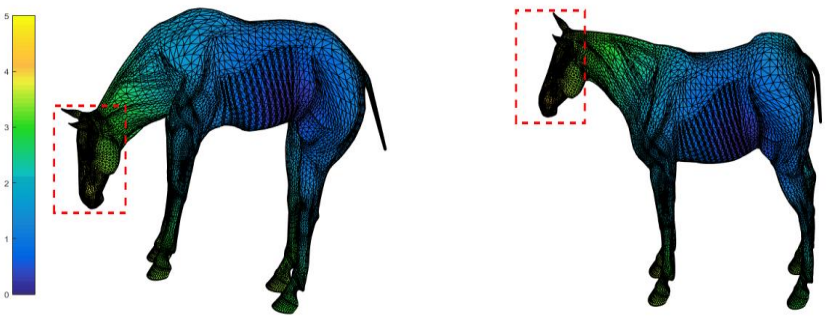

Figure 6.6 Geodesic distance color maps and corresponding segmentations.

Constraints are usually used to detect and remove outliers in both rigid and non-rigid registration. When (geodesic) distance is used as an invariant characteristic to generate correspondences, the symmetry problem arises (Aiger et al., 2008). In our proposed algorithm, we exploit the following strategy to improve the success rate of correspondence computation. Let us assume that a point $\boldsymbol{q}_t$ is selected from an area of symmetry in P_t and that we search for a corresponding point in P_s. We generate *n* candidates $\{\boldsymbol{q}_s^1, \boldsymbol{q}_s^2, \boldsymbol{q}_s^3, \dots, \boldsymbol{q}_s^n\}$ from P_s and list them in descending order according to $\mathcal{T}_{RMSE}$. We use a fuzzy C-means algorithm to segment these candidates and then obtain clusters and their centers. If $\boldsymbol{q}_t$ is in an area of symmetry in P_t, then the corresponding candidates will also appear in an area of symmetry in P_s; hence, there will be at least two symmetric clusters in the candidate subset. After generating the symmetric clusters and their centers, we search for the nearest point $\boldsymbol{g}_t$ to $\boldsymbol{q}_t$ in P_t; this point will already have a corresponding point $\boldsymbol{g}_s$ in P_s. We can now compare the distance $\boldsymbol{g}_t\boldsymbol{q}_t$ with the distances from $\boldsymbol{g}_s$ to each center. The corresponding point for $\boldsymbol{q}_t$ exists in the cluster with the smallest gap.

6.4.4 Transformation and optimization

6.4.4.1 RANSAC extraction and transformation

After obtaining correspondences from P_t and P_s, we need to handle the second key challenge i.e. to calculate the transformation parameters to align P_t to P_s. In non-rigid cases, a single set of transformation parameters is not sufficient to handle registration by finding and segmenting rigid subsets from the global area to independently complete the individual registrations. In the proposed algorithm, we have designed a RANSAC (Fischler and Bolles, 1981) framework to complete this process. RANSAC is a robust algorithm for fitting models in the presence of many outliers (Strutz, 2016) and is an appropriate approach to deal with our situation. A correspondence dataset $\{(\mathcal{C}_t, \mathcal{C}_s) | (\boldsymbol{c}_t^1, \boldsymbol{c}_s^1), (\boldsymbol{c}_t^2, \boldsymbol{c}_s^2), (\boldsymbol{c}_t^3, \boldsymbol{c}_s^3), \dots, (\boldsymbol{c}_t^k, \boldsymbol{c}_s^k)\}$ is generated using this method. Here $\mathcal{C}_t$ and $\mathcal{C}_s$ represent the selected point subsets from P_t and P_s, respectively, and $(\boldsymbol{c}_t^i, \boldsymbol{c}_s^i)$ is the *i*th correspondence, where $\boldsymbol{c}_t^i$ is from $\mathcal{C}_t$ and $\boldsymbol{c}_s^i$ is from $\mathcal{C}_s$. We now introduce this correspondence dataset into RANSAC. In each iteration, we obtain a subset $(\mathcal{C}_t^i, \mathcal{C}_s^i)$ from $(\mathcal{C}_t, \mathcal{C}_s)$. Each subset $(\mathcal{C}_t^i, \mathcal{C}_s^i)$ contains m ($m \geq 3$) correspondences,

namely $\{(\mathcal{C}_t^i, \mathcal{C}_s^i) | \ (\boldsymbol{c}_t^{k_1}, \boldsymbol{c}_s^{k_1}), (\boldsymbol{c}_t^{k_2}, \boldsymbol{c}_t^{k_2}), \dots, (\boldsymbol{c}_t^{k_m}, \boldsymbol{c}_t^{k_m})\}$, and these m correspondences satisfy the given conditions for a rigid-body transformation. At the same time, a set of rigid-body transformation parameters T_i can be obtained. Next, we use T_i to transform P_t to a new position to obtain P_t^i and then we reverse-search correspondences from P_s to P_t^i. We store a new correspondence if the correspondence distance is less than a given threshold. When all the points in P_s have a reliable corresponding point, we terminate the iteration; otherwise, we remove $(\mathcal{C}_t^i, \mathcal{C}_s^i)$ from $(\mathcal{C}_t, \mathcal{C}_s)$ and perform the next step of the iteration.

If there are still some correspondences that do not belong to any correspondence subsets after RANSAC, then we execute a local optimization strategy. Let us assume that the correspondence $(\boldsymbol{c}_t^j, \boldsymbol{c}_s^j)$ does not belong to any subset. Then we use the *K*-nearest neighborhood algorithm to search for the three nearest non-collinear points to $\boldsymbol{c}_t^j$ (i.e. $\{(\mathcal{N}_t^j) | \ \boldsymbol{c}_t^j, \boldsymbol{n}_t^{j_1}, \boldsymbol{n}_t^{j_2}\}$) in P_t and carry out the same operation in P_s to find $\{(\mathcal{N}_s^j) | \ \boldsymbol{c}_s^j, \boldsymbol{n}_s^{j_1}, \boldsymbol{n}_s^{j_2} \dots \boldsymbol{n}_s^{j_k}, \ k > 2\}$. Here we need to make the hypothesis that there exists a very small area (e.g. $\mathcal{N}_t^j$) in which there is no deformation. We can now find three points in $\mathcal{N}_s^j$ that result from an (approximately) rigid-body transformation from $\mathcal{N}_t^j$.

6.4.4.2 Global fine registration and surface fitting

The results of the algorithm give the initial positions for each cluster, and now we need to find the best alignment for each of them and finally generate the best global alignment. For this purpose, ICP or a variant can be employed on each cluster, after which a fine registration algorithm can be performed again on all points within each point cloud to arrive at a global optimization. More details of the fine registration procedure can be found in Besl and McKay (1992), Zhang (1994), Chen and Medioni (1991, 1992), Low (2004), Akca (2010) and Ge and Wunderlich (2016).

6.5 Experimental results and analysis

6.5.1 Implementation

We implemented the proposed non-rigid registration algorithm in C++, making use of the open-source Point Cloud Library (PCL) (Rusu and Cousins, 2011). Before the non-rigid registration, we first needed to remove outliers and carry out down-sampling. These two steps can be completed either in the PCL environment itself or independently in third-party software, such as Geomagic Studio 2014. We performed fine registration within an improved ICP, i.e. using linear least squares (Low, 2004). Once the iteration had successfully converged, we used the RM-LS fitting strategy to generate a deformed surface from the deformed discrete point cloud.

In the experiments, we used the TOSCA high-resolution dataset, which is constructed with ground truth correspondences, and we were therefore able to achieve a satisfactory correspondence rate using the proposed variant 4PCS strategy; moreover, we were able to calculate the RMSE after global optimization. In a real registration procedure, it is not necessary to achieve 100% correspondences for P_s in the process described in Section 6.3.4.1, since the subsequent optimization can compensate for the missing parts. In our experiments, we terminated the search process when the correspondence rate reached 80%. After having obtained the deformed surface, we compared the regions of overlap between the source and the deformed surfaces using the 3D comparison module of Geomagic Studio 2014 software and determined the mean values of the 3D bias.

6.5.2 Experiments

Figures 6.7–6.11 show non-registration cases with different datasets from TOSCA. The silver and red models in these figures represent the source and target point cloud surfaces, respectively. The green models show the point cloud surfaces resulting from the transformation from the deformed target point cloud surfaces to the corresponding source point cloud surfaces. The 3D color maps in Figs. 6.7–6.11 allow a comparison to be made between the transformed surfaces and the source surfaces. Table 6.1 gives more detailed information on the numerical results. From the first two images in each of Figs. 6.7–6.11, we can see that the proposed algorithm can perform well in non-rigid cases. Moreover, as can be seen from Table 6.2, the proposed GD-4PCS method gives a success rate for establishing true correspondences of at least 85%. The RMSE in the numerical examples shows a rigid fine registration level of about 2–3 mm. For the Horse dataset, the geodesic distances are affected by topological noise. The neck exhibits significant stretching that causes the geodesic distances from the back to the head to be unreliable. In this case, we divided the whole area into different corresponding segments and then carried out the proposed algorithm on each segment individually. The success rate for correspondences was improved from 85% to 96% and the RMSE was reduced from 3.65 mm to 2.95 mm. The color maps in Figs. 6.7–6.11 confirm that the proposed algorithm can be of use in surface reconstruction. The two color maps (from 1 to 2) in the Horse case (Fig. 6.9) reflect the improvement obtained by applying the segmentation. Moreover, the histograms in each color map show that the residuals in all the cases are normally distributed, which means there are no systematic errors in our proposed algorithm and provides further evidence of its reliability.

Table 6.1 Numerical results: test datasets, number of points, number of feature points, success rate of correspondences with the variant 4PCS method, RMSE after fine registration and 3D comparison biases using fitting surfaces.

Dataset		Points	Feature points	Success rate[a] of correspondences	RMSE (mm)	3D bias (mm)
cat	pose1 – pose2	27 894	678	90%	1.33	1.94
	pose1 – pose3	27 894	658	94%	0.99	0.70
Horse	whole	19 248	898	85%	3.65	5.03
	segments	19 248	898	96%	2.95(max)	2.06
Michael	pose1 – pose2	52 565	1241	95%	2.66	1.54
	pose1 – pose3	52 565	1199	94%	2.88	1.60

[a] The success rate here refers only to a point recorded in the target cloud finding its true corresponding point in the source cloud. However, this does not mean that the remaining correspondences are incorrect results.

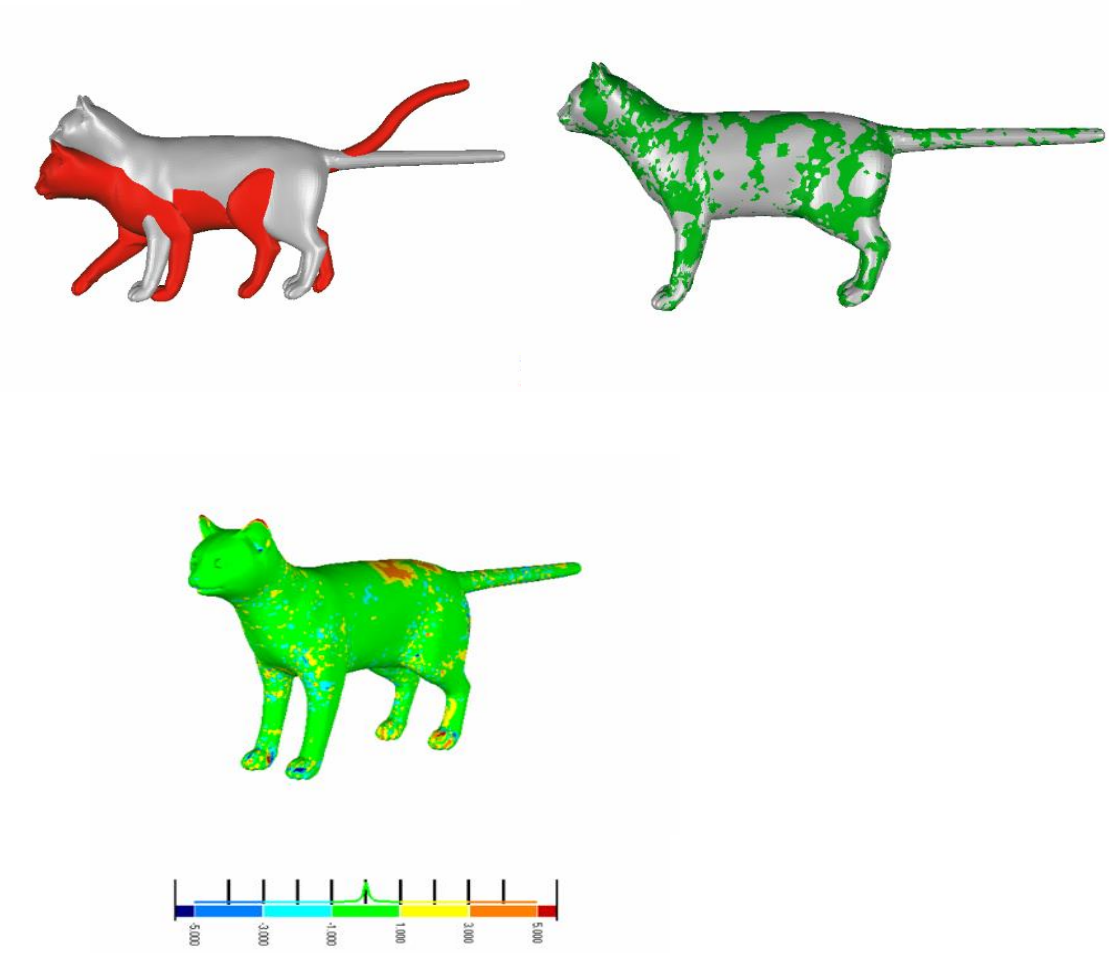

Figure 6.7 Non-rigid registration for Cat dataset with pose1 and pose2 (color bar in mm).

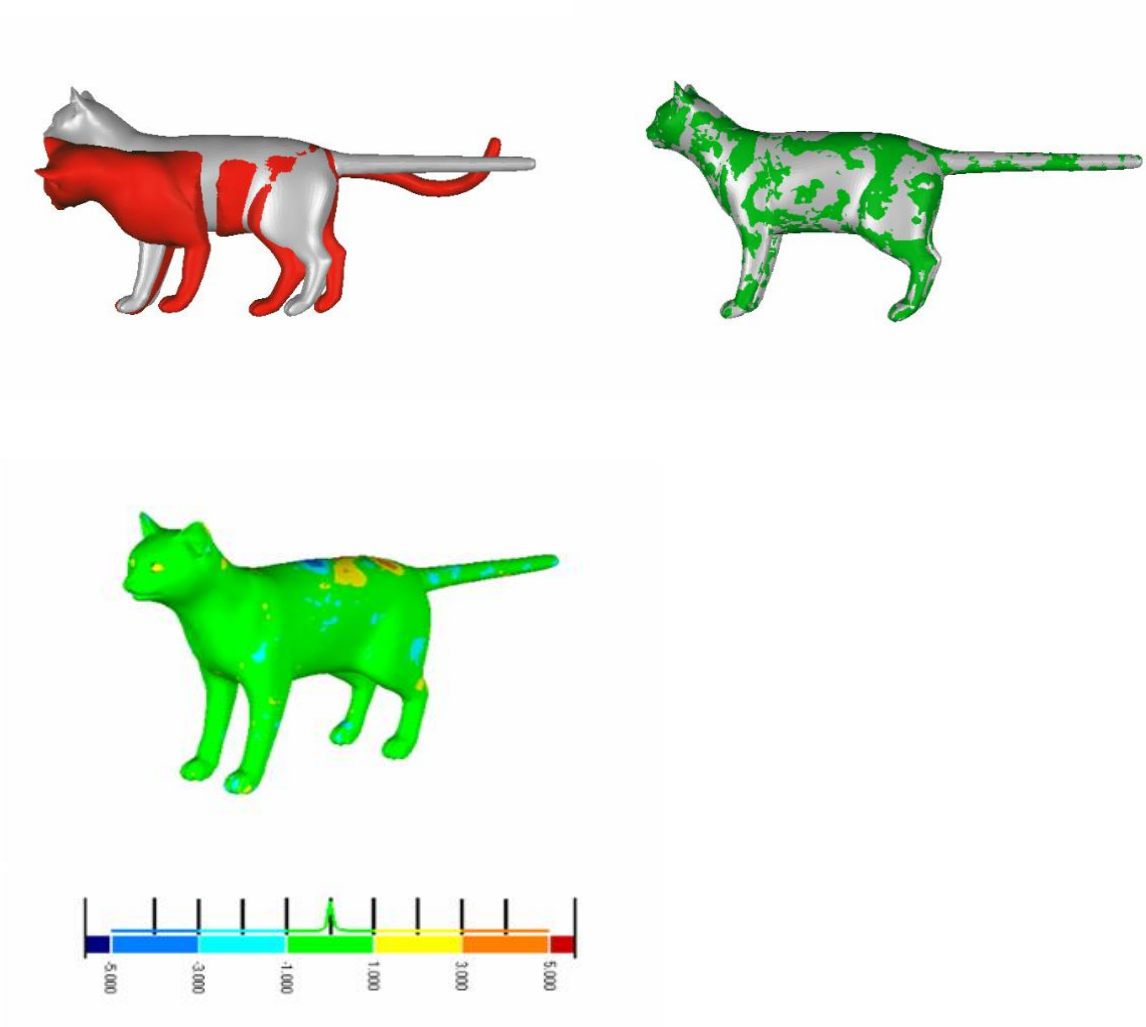

Figure 6.8 Non-rigid registration for Cat dataset with pose1 and pose3 (color bar in mm).

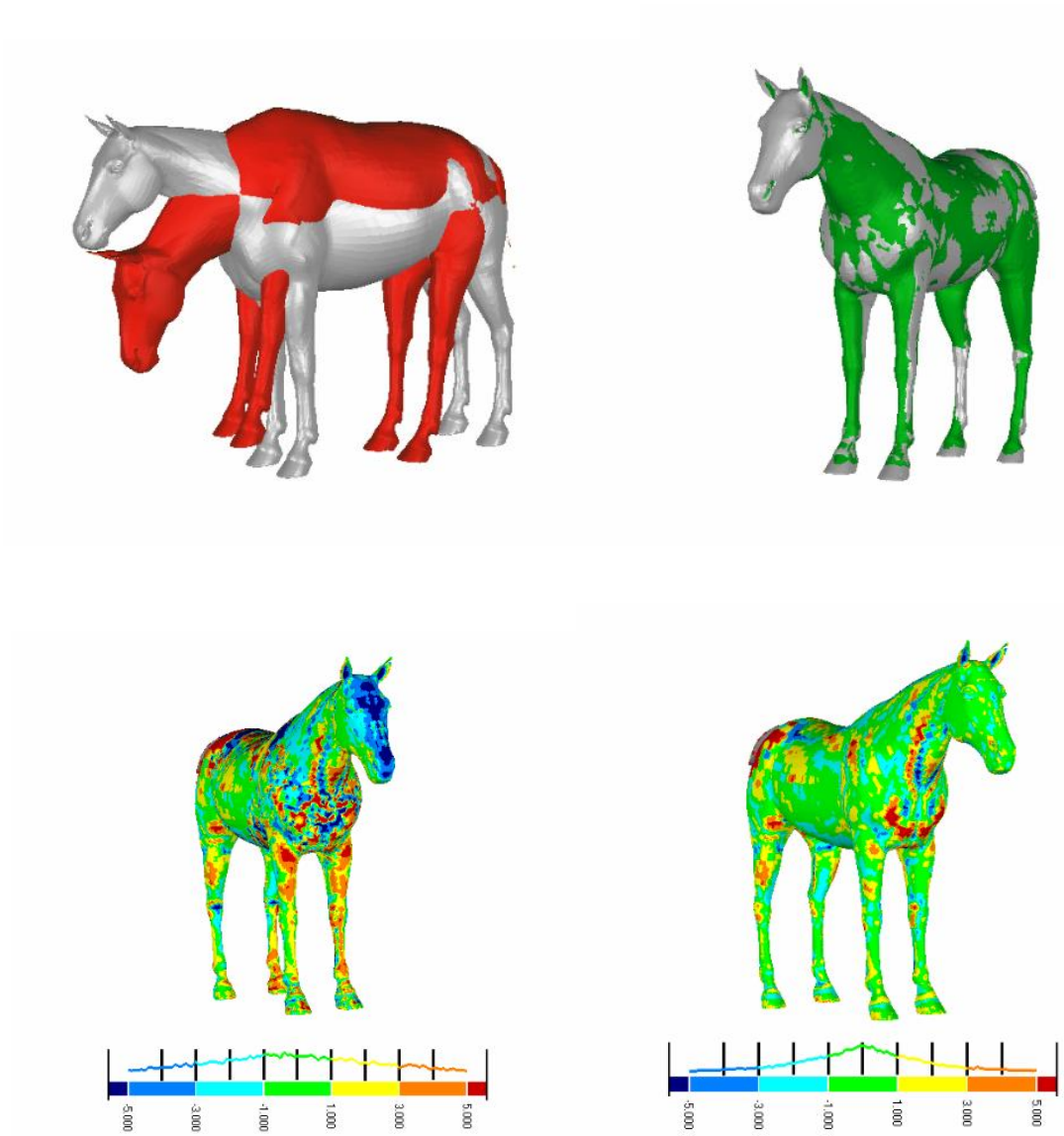

Figure 6.9 Non-rigid registration for Horse dataset with different poses (color bar in mm).

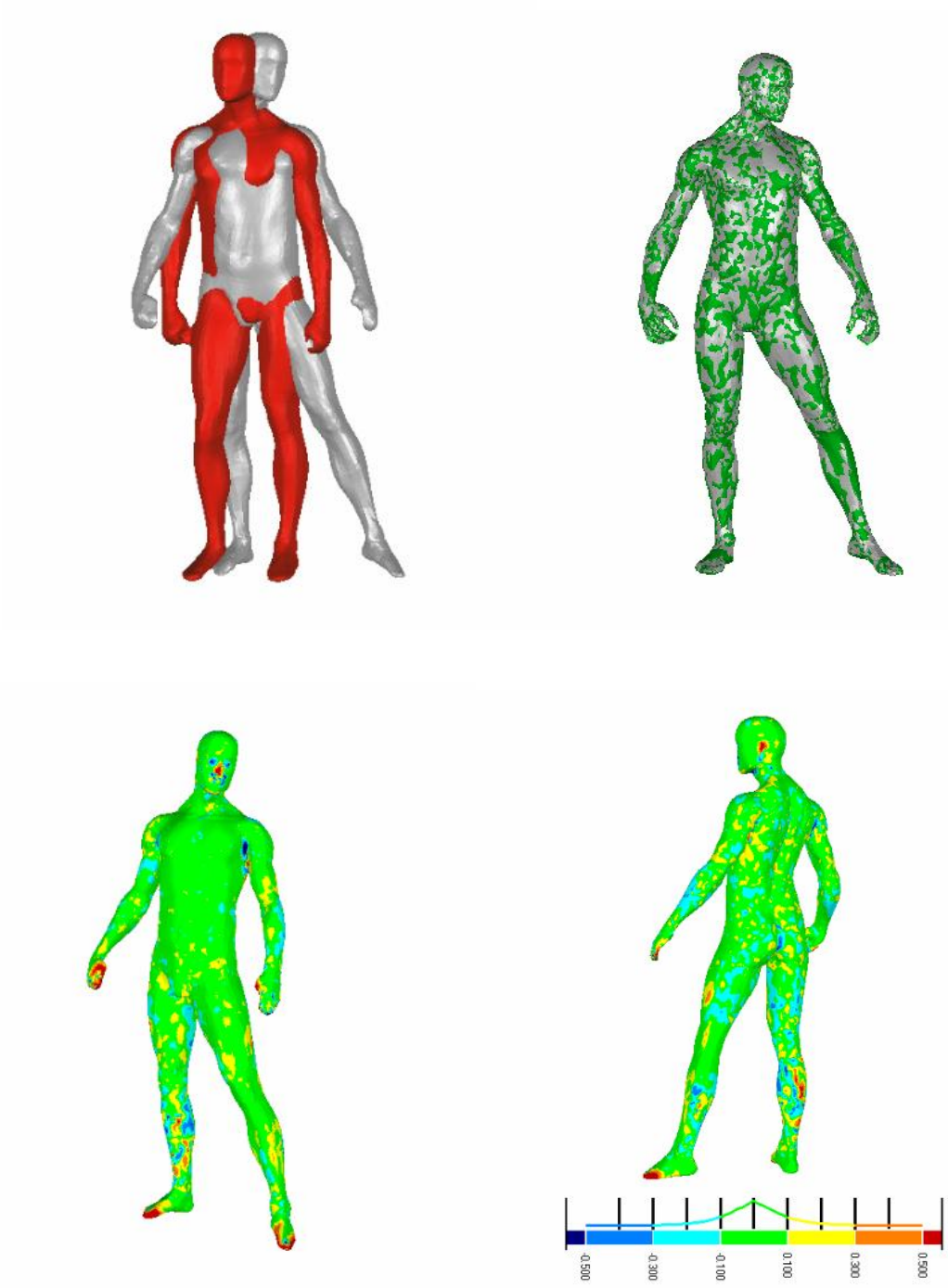

Figure 6.10 Non-rigid registration for Michael dataset with pose1 and pose2 (color bar in cm).

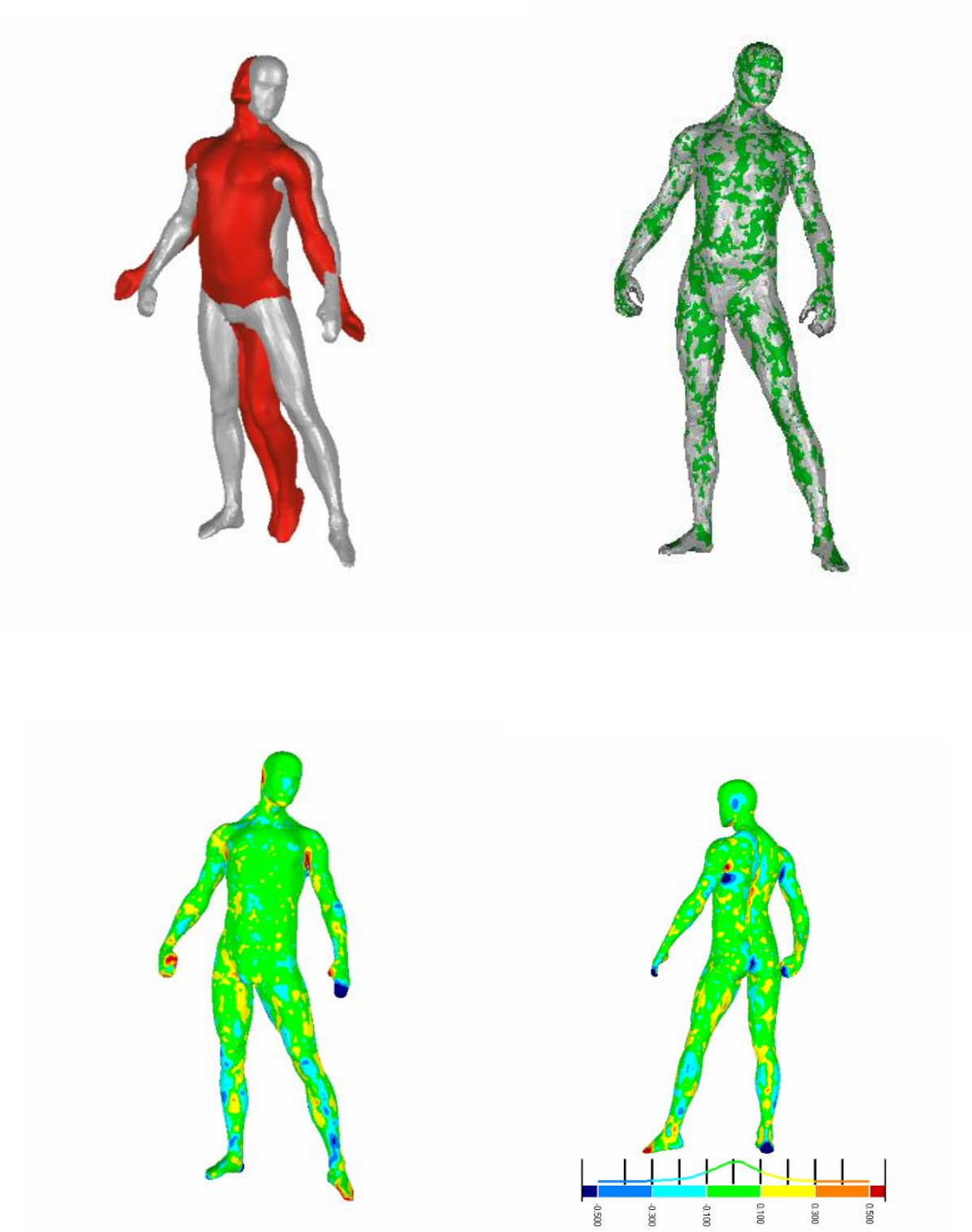

Figure 6.11 Non-rigid registration for Michael dataset with pose1 and pose3 (color bar in cm).

6.5.3 Discussion

Detecting and establishing stable correspondences is a crucial step in all approaches to registration problems and is one of the main challenges in non-rigid registration methods. In

this section, we compare the method proposed here with that of Ovsjanikov (2010) when finding correspondences in the case of isometric deformation. Ovsjanikov's method is one of the most popular for this task and has exhibited good performances in the author's experiments. It is similar to the proposed method in that it establishes correspondences based on the geodesic distances from scanning points to key points. Very importantly, like the proposed method, it allows the presence of measurement noise. Ovsjanikov's method was run using its author's original open codes (Ovsjanikov et al., 2010).

From Table 6.1, it can be seen that the proposed method performs well in the search for correspondences. Figure 6.12 compares the performances of Ovsjanikov's method and the proposed method in finding true correspondences in the case of isometric deformation. The proposed method obtains at least 90% true correspondences, which is approximately 10% higher than can be obtained using Ovsjanikov's method. As already mentioned, we are interested in introducing non-rigid registration to handle deformations in the measurement field, for which measurement noise is unavoidable. Therefore, we introduced $\sigma = \pm 2$ mm random errors in the geodesic distances. Figure 6.13 shows that the results from both methods were then affected by random errors. The advantage of the proposed method over Ovsjanikov's was less significant than in the case of the results presented in Fig. 6.12, with the success rates decreasing to approximately 20% and 18% for the proposed method and Ovsjanikov's method, respectively. One reason for this is that GD-4PCS needs to calculate geodesic distances from all points to four key points, whereas Ovsjanikov's method uses only one key point, so the proposed method is more sensitive to errors in geodesic distances. However, the benefit of having four key points rather than just one is still clear from the higher success rate in finding correspondences.

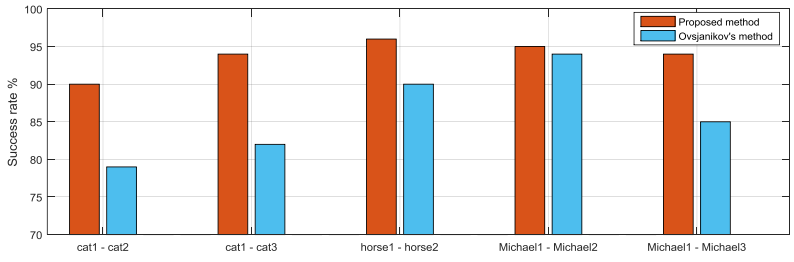

Figure 6.12. The comparisons of success rate of finding true correspondences in the isometric cases.

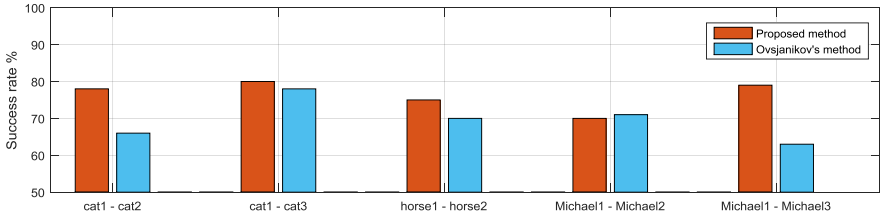

Figure 6.13. The comparisons of success rate of finding true correspondences in the approximately isometric cases.

6.6 Conclusions

In this paper, we have considered isometric deformations and have proposed a computational combination to execute non-rigid registration. The geodesic distance acts as an isometric invariant characteristic and can therefore be employed to search for correspondences using the proposed algorithm. The search process is based on the GD-4PCS method, with some constraints being exploited to improve the correspondences. The derived stable correspondence subsets thus obtained are used in a RANSAC framework to obtain initial values for each cluster. Finally, a fine registration based on these initial values is performed, with subsequent global optimization.

The main advantage of the method is that it establishes stable correspondences. Using the geodesic distance within the GD-4PCS method, we can reliably locate a point from a surface to its deformation. The RANSAC framework provides the possibility of obtaining initial values for each cluster without prior search of rigid clusters.

One of the limitations of our method is that if the assumption of consistency of geodesic distance between the surfaces is invalid, this will result in erroneous registration because incorrect correspondences will be established. Moreover, it should be noted that the proposed method does not show any advantage in terms of time consumption. In our experiments, the programs always need 3–5 minutes to complete a single registration. In future work, we propose to further reduce the effects of topological and other kinds of noise on the reliability of geodesic distances. Another issue is the need to address the symmetry problem in the GD-4PCS method in order to increase the success rate when searching for correspondences.

Chapter 7

Overview, Conclusions, and Outlook

TLS is a promising technique and has great potential for development as a surveying technique. Laser scanners are now under rapid development in terms of both hardware and data post-processing software, which provides more possibilities for applying TLS in geodetic engineering and geo-information. The aim of the work described in this thesis was to *promote deformation monitoring methods using TLS*. In order to achieve this aim, we have solved four significant problems in preparation for employing TLS for deformation monitoring. At the beginning of this thesis, we posed four key questions. We then proposed approaches to solving those questions. Now, at the end of the thesis, we will repeat those questions and give a brief overview of the solutions proposed for each of them. Conclusions can then be drawn with regard to the work presented here. Finally, we will point out the limitations of our proposed approaches and the outlook for future work.

7.1 Overview

7.1.1 Question 1: Is there a general technique to extract target centers from raw point clouds to represent specific positions?

A general method for extracting the center of a target was proposed to address this problem. We employed the weight total squares technique to extract an ideal target plane such that stochastic models of all observations could be feasibly considered. Then, based on the obtained target plane, the program extracted a "cross-lines" construct (expressed by discrete 3D points) by detecting gaps in the intensity values. Subsequently, we exploited the weight total squares technique again to regress the real cross lines and then to extract an intermediate point to represent the target center. A robust strategy, M-estimation, was employed in the fitting processes to avoid the influence of outliers. The results calculated by the proposed method were compared with those obtained by the dedicated software supplied with the scanner. Figure 7.1 shows the program pipeline.

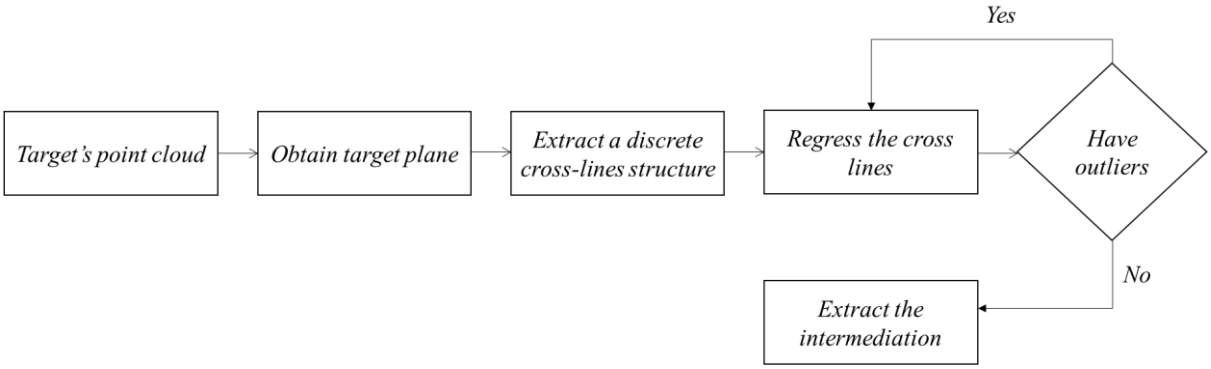

Figure 7.1 Pipeline of target identification.

7.1.2 Question 2: Can we predict a feasible configuration to complete the calibration of a laser scanner to provide the expected results?

First of all, we proposed specific criteria for assessing whether the estimated calibration parameters are sufficiently accurate. We related a statistical bound on the unknown deviation of the estimate to the standard deviations of the scanner's raw measurements. Moreover, in terms of a feasible separation of the estimated unknown parameters, both APs–APs and APs–EOs, we considered many descriptions in the early literature regarding the correlations and then selected a reasonable cut-off value as a threshold. A least squares method within a Gauss–Helmert model was exploited to execute adjustment. We carried out an observability analysis individually for each AP, highlighting the required number and spatial distribution of scanned object points. Finally, based on the above conclusions, we applied the calibration to a frequently used subset of APs. Taking into account the practical relevance of this approach, we subsequently discussed three calibration cases. Figure 7.2 shows schematically how this approach proceeds.

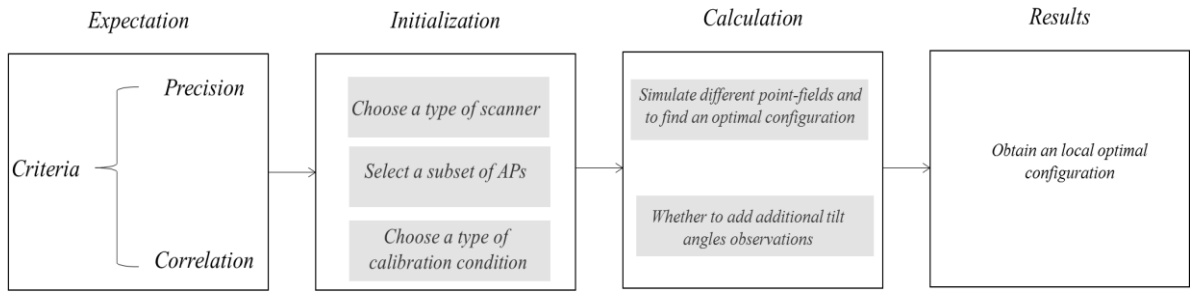

Figure 7.2 Pipeline of point-field calibration for a laser scanner.

7.1.3 Question 3: Can we register two kinds of point cloud that are captured by two different sensors and then further assess the behavior of each kind of residual after adjustment?

We presented an extension of the least squares 3D (LS3D) matching method, using the nonlinear Gauss–Helmert method (GH-LS3D) to estimate transformation parameters between two point clouds and to align such point clouds. This approach is based on the errors-in-variances model and is capable of simultaneously considering different stochastic models in one registration. Before alignment, outliers should be removed from the raw point clouds and the whole point clouds then optionally down-sampled. The correspondences in this program can be generated by different strategies (e.g., point-to-plane), following which a robust criteria can be used to remove poor correspondences. After an acceptable correspondence subset has been obtained, a rigid-body transformation is executed within a Gauss–Helmert model. A set of candidates can be obtained after adjustment and then transformed from the *target* point cloud to the *source* point cloud by using the estimated parameters. Subsequently, a specific criterion is applied to judge the transformed results. The iteration is terminated if the transformed accuracy is sufficient. Figure 7.3 shows the iteration of the proposed approach.

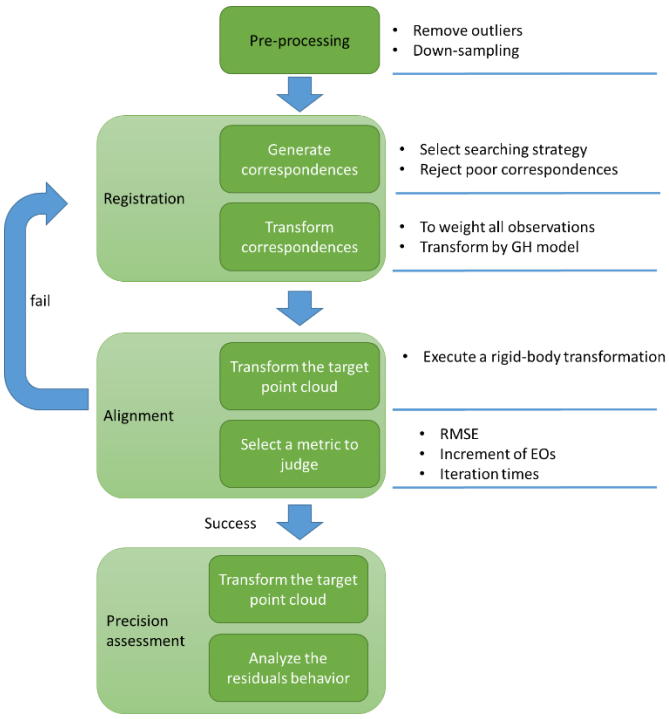

Figure 7.3 Pipeline of the GH-LS3D approach.

7.1.4 Question 4: Can we align two point clouds that are obtained from different epochs when the scanned object has different orientations in each epoch?

To address this question, we proposed a novel combination approach. First of all, geodesic distances were introduced instead of Euclidean distances in the 4PCS algorithm. Based on this substitution, we extended the 4PCS algorithm from rigid to non-rigid cases. Properties invariant between two point clouds can be found, even when deformations happened. In order to execute the extended 4PCS algorithm, we first extracted four key feature points from a raw point cloud. Down-sampling is also an optional strategy to accelerate the calculation. Robust strategies can also be introduced into the calculation to improve the quality of correspondences. After an acceptable correspondence subset has been generated, a RANSAC program is executed to align the rigid clusters. After each iteration, some points in the *source* point cloud can find their correspondences in the transformed *target* point cloud. If a given percentage of points in the *source* point cloud correspond to points in the transformed *target* point cloud, the iteration is terminated. The proposed framework is shown schematically in Figure 7.4.

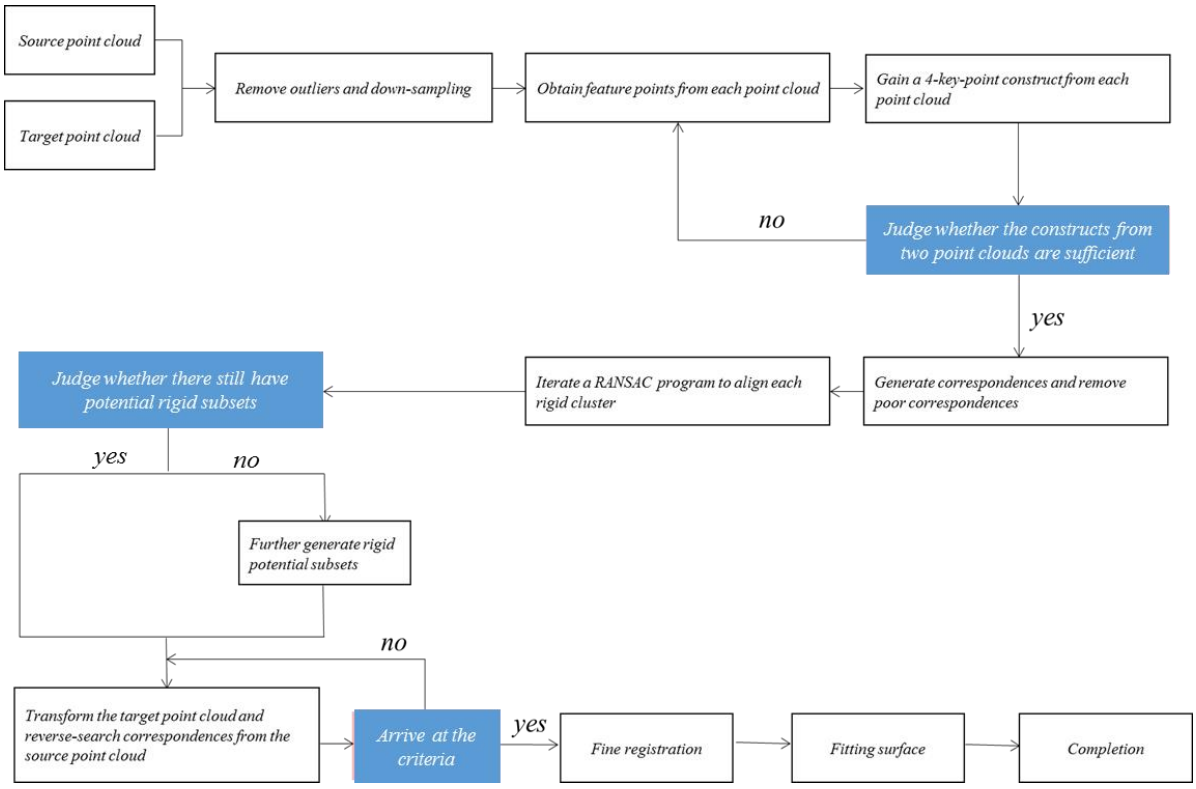

Figure 7.4 Pipeline of the proposed framework for non-rigid registration.

7.2 Conclusions

In this thesis, four novel approaches were proposed to separately solve different issues arising in deformation monitoring by TLS. For each approach, we carried out different experiments to verify its feasibility. Our conclusions from these studies are as follows:

- The proposed general extraction algorithm can be employed to accurately obtain a planar quadrant target center without the need for any information that is restricted for proprietary reasons. A4 paper targets can replace the targets supplied with the scanner when the proposed approach is used to extract a target center.
- The criteria derived for the precision can be exploited to assess whether the calibration parameters are accurate enough. If they are, then the estimated APs can be used to significantly reduce the deviation between the scanner measurements and the corresponding true values.
- The proposed configurations provide users with guidance on effective implementation of calibration in different cases to obtain the expected results (when the subset of APs is $\{a_0, b_1, b_2, c_0\}$).
- A starting point for determining a practically useful configuration of OPs within the point field can be determined for any subset of APs given the AP-per-AP analysis.
- The extended GH-LS3D matching approach allows users to perfectly align two point clouds that are captured from different scanners (e.g. Leica HDS 7000 and RIEGL VZ400).
- GH model is introduced into GH-LS3D to solve nonlinear LS problems such that the stochastic models of both source and target point clouds can be simultaneously considered in the adjustment.
- GH-LS3D method is a powerful fine rigid registration method in terms of registration accuracy and computational effective.
- The extended 4PCS algorithm allows the effective generation of correspondences in non-rigid cases.
- Based on the proposed non-rigid registration approach, we can use 3D information (i.e., 3D translations and 3 rotation angles) to represent deformation happened on an object itself in terms of rigid body motion.

As already mentioned, this thesis has made a number of preparations to the application of TLS in deformation monitoring. These can be used specifically to solve a variety of problems arising in deformation monitoring by TLS.

7.3 Outlook

This thesis has succeeded in its aim of making relevant contributions to the development of deformation monitoring by TLS, but of course there is still room for improvement. The following are some limitations of the current work, together with suggestions for future research.

7.3.1 The general target center extraction approach

The key limitation of the approach described here is that we do not consider the influence of external factors on the value of the intensity, which is the core information in the proposed approach. In fact, the intensity data from each scan will be affected by a number of uncertain factors, such as illumination, humidity, and incidence angle (Fang et al., 20105). Moreover, the proposed approach is sensitive to observational error. Although some robust strategies have been introduced to detect and eliminate outliers, the residual errors may cause a deterioration in the accuracy of both target-plane and cross-line fitting.

In the future, at least two improvements need to be made to the algorithm to compensate for these shortcomings. The first is an intensity correction mechanism and the second is the inclusion of robust judgment.

7.3.3 The GH-LS3D matching approach

We currently use the GH-LS3D method to solve rigid registration issues. Although this powerful approach can handle different kinds of observations in both *target* and *source* point clouds, so far we have only shown the posterior accuracy of each observation after adjustment, but have not really used this information to improve registration. Moreover, processing speed is a bottleneck for the GH-LS3D method, and the initial values can significantly influence the GH-LS3D method.

We will focus on analysis of the behavior of residuals in future work in order to maximize the advantages of the GH-LS3D. Multi-sensor fusion is also a potential area for future research using GH-LS3D. Further improvements could be made to GH-LS3D to increase its efficiency.

7.3.2 Configuration requirements for terrestrial laser scanner calibration

We give only locally optimal configurations to carry out a given subset of AP calibrations in different cases. Although such a given subset of APs contains the most significant system errors, for some scanners there may still be further unknown errors in the system. Furthermore, we do not give a configuration to perform calibration for hybrid scanners. Last, but not least, we use

a Monte Carlo closed-loop simulation to verify that the correlation is sensitive to the position of object points (OPs), but do not give a rigorous algebraic derivation to prove this conclusion.

Future work should take into account larger AP subsets than that treated here. Hybrid scanners should also be considered in the proposed point-field calibration. Moreover, in order to make the results rigorous, we need to give a rigorous algebraic derivation.

7.3.4 Non-rigid registration under isometric deformation

From the discussion in this thesis, it is clear that the key limitation of the proposed framework is the uncertainty in geodesic distances. This uncertain characteristic will be magnified in measurements using TLS because the scanned object surface is represented by a number of discrete points and those scanning points contain two sensitive characteristics. The first is that the position of a laser spot is relatively random. The second is that in measurements, all observations contain random errors. These two features will further magnify the uncertainties in geodesic distances. Furthermore, determination of the corresponding four-key-point constructions from two point clouds is time-consuming and may fail in some special cases.

Therefore, the most important way in which the proposed approach can be improved is by overcoming the uncertainty in geodesic distances to ensure the accuracy of the generated correspondences. Future work will concentrate more on this aspect. Moreover, we are also interested in finding an effective method for establishing the corresponding four-key-point constructions from two point clouds, for example by introducing geo-reference points to replace the search process.

7.4 Contribution

The field of deformation analysis in geodetic has developed nearly a century and already arrived at an advanced level, however, with the continuous upgrading of technology and instrument we need to constantly improve our understanding in the deformation analysis. In this thesis, we attempts to find solutions for rigorous area deformation analysis from point clouds. Although there are many shortcomings in our solutions, this thesis shows a new direction to promote the research in the deformation analysis and also displays a broad application space in geodetic.

References

Ackermann, F., 1984. Digital image correlation: performance and potential application in photogrammetry. Photogrammetric Record 11 (64), 429–439.

Aiger, D., Mitra, N.J. and Cohen-Or, D., 2008. 4-Points congruent sets for robust pairwise surface registration. *ACM Transactions on Graphics (TOG), 27 (3), pp. 1–10.*

Akca, D., 2007. Least Squares 3d Surface Matching. PhD Thesis, Swiss Federal Institute of Technology, Zürich.

Akca, D., 2010. Co-registration of surfaces by 3D least squares matching. *Photogrammetric Engineering and Remote Sensing 76 (3), 307–318*.

Altman, N.S., 1992. An introduction to kernel and nearest-neighbor nonparametric regression. *The American Statistician 46(3): 175-185*.

Arya, S., Das, G., Mount, D. M., Salowe, J. S., Smid, M., 1995. Euclidean spanners: short, thin, and lanky. *In Proceedings of the twenty-seventh annual ACM symposium on Theory of computing (pp. 489-498). ACM*.

Arya, S., Mount, D. M., Netanyahu, N. S., Silverman, R., Wu, A. Y., 1998. An optimal algorithm for approximate nearest neighbor searching fixed dimensions. *ACM 45 (6), 891–923*.

Bae, K.-H., 2006. Automated Registration of Unorganised Point Clouds from Terrestrial Laser Scanners. Ph.D. thesis, Curtin University of Technology.

Berretti, S., Del Bimbo, A. and Pala, P., 2006. Description and retrieval of 3D face models using iso-geodesic stripes. *In Proceedings of the 8th ACM International Workshop on Multimedia Information Retrieval (pp. 13-22). ACM*.

Besl, P., McKay, N., 1992. A method for registration of 3-d shapes. *IEEE Transactions on Pattern Analysis and Machine Intelligence 14 (2), 239–256*.

Bitelli, G., Dubbini, M., Zanutta, A., 2004. Terrestrial laser scanning and digital photogrammetry techniques to monitor landslide bodies. *International Archives of Photogrammetry, Remote Sensing and Spatial Information Sciences, 35(Part B 5), 246-251*.

Blais, G., Levine, M. D., 1995. Registering multiview range data to create 3D computer objects. *Pattern Analysis and Machine Intelligence, IEEE Transactions on, 17(8), 820-824*.

Boehler, W., & Marbs, A. (2005). Investigating Laser Scanner Accuracy, i3mainz. Institute for Spatial Information and Surveying Technology, FH Mainz, University of Applied Sciences, Mainz, Germany.

Bronstein, A.M., Bronstein, M.M. and Kimmel, R., 2006. Generalized multidimensional scaling: a framework for isometry-invariant partial surface matching. *Proceedings of the National Academy of Sciences, 103 (5), pp. 1168–1172*.

Bronstein, A.M., Bronstein, M.M. and Kimmel, R., 2008. Numerical Geometry of Non-Rigid Shapes. Springer.

Bronstein, A.M., Bronstein, M.M., Kimmel, R., Mahmoudi, M. and Sapiro, G., 2010. A Gromov–Hausdorff framework with diffusion geometry for topologically-robust non-rigid shape matching. *International Journal of Computer Vision, 89(2–3), pp. 266–286*.

Böhm, J., Becker, S,. 2007. Automatic marker-free registration of terrestrial laser scans using reflectance. *In Proceedings of 8th Conference on Optical 3D Measurement Techniques, Zurich, Switzerland (pp. 338-344).*

Carmichael, O., Huber, D., Hebert, M., 1999. Large data sets and confusing scenes in 3-D surface matching and recognition. *In Proc. 2nd Int. Conf. 3-D Digital Imaging Model. pp. 358–367*.

Chang, I. S., Lee, C. H., 1998. Membrane filtration characteristics in membrane-coupled activated sludge system—the effect of physiological states of activated sludge on membrane fouling. Desalination, 120(3), 221-233.

Chan, T.O., Lichti, D.D., Belton, D., 2015. A rigorous cylinder-based self-calibration approach for terrestrial laser scanners. *ISPRS Journal of Photogrammetry and Remote Sensing, 99, 84-99.*

Chang, W., Zwicker, M., 2008. Automatic registration for articulated shapes. *Computer Graphics Forum, 27 (5), pp. 1459–1468*.

Chen, Y., Medioni, G., 1991. Object modeling by registration of multiple range images. In: Proc. *IEEE International Conference on Robotics and Automation, vol. 3, Sacramento, CA, 9–11 April, pp. 2724–2729*.

Chen, Y., Medioni, G., 1992. Object modelling by registration of multiple range images. *Image and Vision Computing, 10 (3), pp. 145–155.*

Chua, C., Jarvis, R., 1997. Point signatures: A new representation for 3D object recognition. *Int. Journal of Computer Vision, vol. 25, no. 1, pp. 63-85*.

Deng, Y., Chen, Y., Zhang, Y., and Mahadevan, S. 2012. Fuzzy Dijkstra algorithm for shortest path problem under uncertain environment. Applied Soft Computing, 12(3), 1231-1237.

Ebeling, A., Chow, J., and Teskey, W. F., 2011.Deformation analysis of terrestrial monitoring observations on Turtle Mountain, Alberta.*Journal of Applied Geodesy* 5:1: 47-58.

Fang, X., 2013. Weight total least squares: necessary and sufficient conditions, fixed and random parameters. *Journal of Geodesy 87, 733–749*.

Fang, W., Huang, X., Zhang, F., Li, D., 2015. Intensity correction of terrestrial laser scanning data by estimating laser transmission function. *IEEE Trans. Geosci. Remote Sens., 53(2), 942-951*.

Feldmar, J., Ayache, N., 1994. Rigid and affine registration of smooth surfaces using differential properties. *In Computer Vision—ECCV'94 (pp. 396-406). Springer Berlin Heidelberg*.

Fischler, M. A., and Bolles, R. C. 1981. Random sample consensus: a paradigm for model fitting with applications to image analysis and automated cartography. Communications of the ACM, 24(6), 381-395.

Fleishman, S., Cohen-Or, D. and Silva, C.T., 2005. Robust moving least-squares fitting with sharp features. *ACM Transactions on Graphics (TOG), 24 (3), pp. 544–552*.

Fuller, W. A., 1987. Measurement Error Models. Wiley, New York.

Fusiello, A., Castellani, U., Ronchetti, L., Murino, V., 2002. Model acquisition by registration of multiple acoustic range views. *Computer Vision—ECCV 2002. Lecture Notes in Computer Science, vol. 2351. Springer, Berlin, pp. 805-819.*

Garcia-San-Miguel, D., Lerma, J.L., 2013. Geometric calibration of a terrestrial laser scanner with local additional parameters: An automatic strategy. *ISPRS Journal of Photogrammetry and Remote Sensing, 79, 122-136.*

Ge, X., Wunderlich, T., 2015. Target identification in terrestrial laser scanning. *Survey Review, 47(341), 129-140.*

Ge, X., Wunderlich, T., 2016. Surface-based matching of 3D point clouds with variable coordinates in source and target system. *ISPRS Journal of Photogrammetry and Remote Sensing, 111, 1-12.*

Glennie, C., Lichti, D. D. (2010). Static calibration and analysis of the Velodyne HDL-64E S2 for high accuracy mobile scanning. *Remote Sensing,2(6), 1610-1624*.

Glennie, C., Lichti, D. D. (2011). Temporal stability of the Velodyne HDL-64E S2 scanner for high accuracy scanning applications. *Remote Sensing,3(3), 539-553*.

Glennie, C. (2012). Calibration and kinematic analysis of the Velodyne HDL-64E S2 Lidar sensor. *Photogrammetric Engineering & Remote Sensing,78(4), 339-347.*

Godin, G., Rioux, M., Baribeau, R., 1994. Three-dimensional registration using range and intensity information. *Videometrics III, vol. 2350. SPIE, pp. 279-290*.

Godin, G., Laurendeau, D., Baribeau, R., 2001. A method for the registration of attributed range images. *IEEE International Conference on 3D Imaging and Modeling, Quebec, May 28-June 1, pp. 179 – 186*.

Godin, G., Boulager, P., 1995. Range image registration through viewpoint invariant computation of curvature. *International Archives of Photogrammety and Remote Sensing, 30(5/WI), 170-175*.

Gong, X., Lin, Y., Liu, J., 2013. 3D LiDAR-camera extrinsic calibration using an arbitrary trihedron. *Sensors 13 (2), 1902–1918*.

Gordon, S.J., Lichti, D. D., and Stewart, M., 2001.Application of a high-resolution, ground-based laser scanner for deformation measurements. *In Proc. of the 10th FIG International Symposium on Deformation Measurements, 19-22 March, Orange, California, USA.*

Gordon, S. J., 2005. Structural Deformation Measurement Using Terrestrial Laser Scanners. *PhD thesis, Curtin University of Technology, Department of Spatial Sciences, Australia.*

Gordon, S. J., and Lichti, D., 2007. Modeling terrestrial laser scanner data for precise structural deformation measurement. *J. Surv. Eng.*, 133(2), *pp.* 72-80.

Grant, D., Bethel, J., Crawford, M., 2012. Point-to-plane registration of terrestrial laser scans. *ISPRS Journal of Photogrammetry and Remote Sensing 72, 16–26*.

Granthamn, J.W., Stargardt, C.D., Dungey, C., and Eduardo, C.,1997. Laser Radar in Adverse Weather. *In: SPIE Proceedings Vol: 3065,pp. 84-93.*

Greenspan, M., Godin, G., 2001. A nearest neighbor method for efficient ICP. In: Proc. Third International Conference on 3-D Digital Imaging and Modeling, Quebec City, Canada, 28 May–1 June, pp. 161–168.

Gruen, A., 1984. Adaptive least squares correlation—concept and first results. Intermediate Research Project Report to Heleva Associates, Inc. Ohio State University, Columbus, Ohio, March, pp. 1–13.

Gruen, A., 1985a. Adaptive least squares correlation: a powerful image matching technique. *South African Journal of Photogrammetry, Remote Sensing and Cartography 14 (3), 175–187*.

Gruen, A., 1985b. Data processing methods for amateur photographs. *Photogrammetric Record 11 (65), 567–579*.

Gruen, A., Acka, D., 2005. Least squares 3D surface and curve matching. *ISPRS Journal of Photogrammetry and Remote Sensing 59, 151–174*.

Hartzell, P. J., Glennie, C. L., Finnegan, D. C., 2015. Empirical waveform decomposition and radiometric calibration of a terrestrial full-waveform laser scanner. *IEEE Trans. Geosci. Remote Sens., 53(1), 162-172.*

Hebert. M and Krotkov. E, 1992. 3-D Measurements from Imaging Laser Radars. *Intl. J. Image and Vision Computing, 10(3):170-178*.

Holst, Ch., Kuhlmann, H. 2014. Aiming at self-calibration of terrestrial lasers canners using only one single object and one single scan. *Journal of Applied Geodesy 8: 295–310.*

Hu, J. and Hua, J., 2009. Salient spectral geometric features for shape matching and retrieval. *The Visual Computer, 25 (5), pp. 667–675*.

Huang, Q.X., Adams, B., Wicke, M. and Guibas, L.J., 2008. Non‐rigid registration under isometric deformations. *Computer Graphics Forum, 27 (5), pp. 1449–1457.*

Huttenlocher, D., 1991. Fast affine point matching: an output-sensitive method. *In Proceedings of IEEE Computer Society Conference on Computer Vision and Pattern Recognition. CVPR' 91 (pp. 263–268). IEEE*.

Jain, V. and Zhang, H., 2006. Robust 3D shape correspondence in the spectral domain. *In Proceedings of IEEE International Conference on Shape Modeling and Applications, 2006. SMI 2006 (pp. 19-19). IEEE*.

Johnson, A., Kang, S., 1997. Registration and integration of textured 3D data. *In Proc. 3DIM '97, Ottawa, Canada, pp. 234–241*.

Jost, T., Hugli, H., 2002. A multi-resolution scheme ICP algorithm for fast shape registration. In 3D Data Processing Visualization and Transmission, 2002. Proceedings. *First International Symposium on (pp. 540-543). IEEE*.

Kaasalainen, S., Ahokas, E., Hyypp, J. and Suomalainen, J., 2005. Study of surface brightness from backscattered Laser intensity calibration of Laser data. *IEEE Geoscience and Remote Sensing Letters 2(3), pp. 255-259*

Kersten, T. H., Sternberg, H., Mechelke, K., Acevedo Proado, C. 2004.Terrestrial lasers canning system MENSI GS 100/GS200 – accuracy tests, experiences and projects at the Hamburg University of applied Sciences. *In*: *Proc. Panoramic Photogrammetry Workshop 2004, organized by TU Dresden, University of Stuttgart, and ISPRS WG V/1, February, 19-22.*

Kim, T., Im, Y. J., 2003. Automatic satellite image registration by combination of matching and random sample consensus. *Geoscience and Remote Sensing, IEEE Transactions on, 41(5), 1111-1117.*

Kremen, T., Koska, B. and Pospsil, J., 2006. Verification of Laser Scanning systems quality. *In: Proc. in the XXIII FIG Congress, Shaping the Change, Munich, Germany*

Langville, A. N., & Stewart, W. J. (2004). The Kronecker product and stochastic automata networks. *Journal of computational and applied mathematics*, 167(2), 429-447.

Lenzmann, L., Lenzmann, E., 2004. Rigorous adjustment of the nonlinear Gauss–Helmert model, third ed. Teubner-Verlag, Leipzig [in German].

Lichti, DD., Stewart, M., Tsakiri, M., and Snow, A.J. 2000. Benchmark Tests on a Three-Dimensional Laser Scanning System. *Geomat Res Australas* 72: 1-24.

Lichti, D.D., and Harvey, B. R. 2002. An investigation into the effects of reflecting surface material properties on TLS measurements. *Geomat Res Australas, 76:1-6.*

Lichti D.D., and Gordon SJ., 2004. Error Propagation in Directly Georeferenced Terrestrial Laser Scanner Point Cloud for Cultural Heritage Recording. In: *Proc. of FIG Working Week, Athens, Greece, May* 22-27.

Lichti, D.D., Franke,J., 2005. Self-calibration of the iQsun 880 laser scanner. In: Gruen, A., Kahmen, H. (Eds.), Optical 3-D Measurement Techniques *VII, vol. I, Vienna, Austria, 3-5 October. pp. 112-122.*

Lichti, D.D., Licht, M.G., 2006. Experiences with terrestrial laser scanner modelling and accuracy assessment. *The International Archives of the Photogrammetry, Remote Sensing and Spatial Information Sciences 36 (Part 5), 155-160.*

Lichti, D.D., 2007. Error modelling, calibration and analysis of an AM-CW terrestrial laser scanner. *ISPRS Journal of Photogrammetry and Remote Sensing 61 (5), pp. 307-324.*

Lichti, D.D., 2009. The impact of angle parametrisation on terrestrial laser scanner self-calibration. *International Archives of the Photogrammetry, Remote Sensing and Spatial Information Sciences 38 (Part 3/W8), pp 171-176.*

Lichti, D.D., 2010. Terrestrial laser scanner self-calibration: correlation sources and their mitigation. *ISPRS Journal of Photogrammetry and Remote Sensing 65 (1), 93-102.*

Lichti, D.D., Jacky Chow, Hervé Lahamya, 2011. Parameter de-correlation and model identification in hybrid-style terrestrial laser scanner self-calibration. *ISPRS Journal of Photogrammetry and Remote Sensing 66 (3), pp 317-326.*

Low, K., 2004. Linear least-squares optimization for point-to-plane ICP surface registration. Technical report, TR04-004, University of North Carolina.

Mahboub, V. (2012). On weighted total least-squares for geodetic transformations. *Journal of Geodesy, 86(5), 359-367*.

Masuda, T., Yokoya, N., 1995. A robust method for registration and segmentation of multiple range images. *Computer Vision and Image Understanding 61 (3), 295–307*.

Mellado, N., Aiger, D. and Mitra, N.J., 2014. Super 4PCS fast global point cloud registration via smart indexing. *Computer Graphics Forum, 33 (5), pp. 205–215*.

Mikhail, E.M., Ackermann, F., 1976. Observations and Least Squares. IEP-A Dun-Donnelley, New York.

Mills. J and Barber. D, 2003. "An Addendum to the Metric Survey Specifications for English Heritage – The Collection and Archiving of Point Cloud Data Obtained by Terrestrial Laser Scanning or Other Methods," English Heritage.

Mohamad, M., Ahmed, M.T., Rappaport, D. and Greenspan, M., 2015. Super generalized 4PCS for 3D registration. *In Proceedings of 2015 International Conference on 3D Vision. 3DV (pp. 598–606). IEEE*.

Mohamad, M., Rappaport, D. and Greenspan, M., 2014. Generalized 4-points congruent sets for 3d registration. *In Proceedings of 2014 International Conference on 3D Vision. 3DV (Vol. 1, pp. 83–90). IEEE*.

Monserrat, O., Crosetto, M., 2008. Deformation measurement using terrestrial laser scanning data and least squares 3D surface matching. *ISPRS Journal of Photogrammetry and Remote Sensing, 63(1), 142-154*.

Mpiperis, I., Malassiotis, S. and Strintzis, M.G., 2007. 3-D face recognition with the geodesic polar representation. *IEEE Transactions on Information Forensics and Security, 2 (3), pp. 537–547*.

Muhammad, N., Lacroix, S. (2010, October). Calibration of a rotating multi-beam lidar. *In Intelligent Robots and Systems (IROS), 2010 IEEE/RSJ International Conference on (pp. 5648-5653). IEEE*.

Mukupa, W., Roberts, G. W., Hancock, C. M. and Al-Manasir, K. 2016. A review of the use of terrestrial laser scanning application for change detection and deformation monitoring of structures. Survey Review, pp. 1-18.

Neitzel, F., 2010. Generalization of total least-squares on example of unweighted and weighted 2D similarity transformation. *Journal of Geodesy 84, 751–762*.

Niemeier, 2008. Ausgleichungsrechnung, De Gruyter, Berlin, New York.

Ovsjanikov, M., Mérigot, Q., Mémoli, F. and Guibas, L., 2010. One point isometric matching with the heat kernel. *Computer Graphics Forum, 29 (5), pp. 1555–1564*.

Park, S.Y., Subbarao, M., 2003. A fast point-to-tangent plane technique for multi-view registration. *IEEE International Conference on 3D Digital Imaging and Modeling, Banff, October 6-10, pp. 276-283*.

Pauly, M., Mitra, N.J., Giesen, J., Gross, M.H. and Guibas, L.J., 2005. Example-based 3D scan completion. *In Proceedings of Symposium on Geometry Processing (EPFL-CONF-149337, pp. 23–32).*

Pertl, A., 1984. Digital image correlation with the analytical plotter Planicomp C-100. *International Archives of Photogrammetry and Remote Sensing 25 (Part 3B), 874–882*.

Pope, A. J., 1972. Some pitfalls to be avoided in the iterative adjustment of nonlinear problems. In: Proc. *38th Annual Meeting of the American Society of Photogrammetry, Washington, DC, pp. 449–477*.

Polo, M. E., Felicísimo, Á. M., Villanueva, A. G., Martínez-del-Pozo, J. Á., 2012. Estimating the uncertainty of Terrestrial Laser Scanner measurements. *IEEE Trans. Geosci. Remote Sens., 50(11), 4804-4808.*

Pulli, K., Duchamp, T., Hoppe, H., McDonald, J., Shapiro, L., Stuetzle, W., 1997. Robust meshes from multiple range maps. *IEEE International Conference on 3d Digital Imaging and Modeling, Ottawa, Canada, October 4–8, pp. 160–168*.

Pulli, K., 1999. Multiview registration for large data sets. In: Proc. *IEEE International Conference on 3d Digital Imaging and Modeling, Ottawa, Canada, May 12–15, pp. 205–211*.

Randall, T. (2011) Construction Engineering Requirements for Integrating Laser Scanning Technology and Building Information Modeling. *Journal of Construction Engineering and Management* 137:10, *pp.* 797-805

Reshetyuk, Y. (2006) Calibration of terrestrial laser scanner Callidus1.1, Leica HDS3000 and Leica HDS2500. *Survey Review, Vol 38, 302 pp. 703-713.*

Reshetyuk, Y., 2009. Self-calibration and direct georeferencing in terrestrial laser scanning. Ph.D. Thesis in Infrastructure. Royal Institute of Technology (KTH), Stockholm, Sweden.

Reshetyuk, Y., 2010. A unified approach to self-calibration of terrestrial laser scanners. *ISPRS Journal of Photogrammetry and Remote Sensing 65 (1), pp. 445-456.*

Romsek, B.R., 2008. Terrestrial Laser Scanning: Comparison of Time-of-flight and Phase Based Measuring Systems. Master's thesis, Purdue University.

Rousseeuw, P., Leroy, A., 1987. Robust Regression and Outlier Detection, Wiley, New York, 1987.

Rusinkiewicz, S., Levoy, M., 2001. Efficient variants of the ICP algorithm. In 3-D Digital Imaging and Modeling, 2001. Proceedings. *Third International Conference on (pp. 145-152). IEEE.*

Rusu, R. B., Marton, Z. C., Blodow, N., Beetz, M. (2008). Persistent point feature histograms for 3D point clouds. *In Proc 10th Int Conf Intel Autonomous Syst (IAS-10), Baden-Baden, Germany (pp. 119-128).*

Rusu, R.B., Blodow, N. and Beetz, M., 2009. Fast point feature histograms (FPFH) for 3D registration. *In Proceedings of IEEE International Conference on Robotics and Automation. ICRA'09 (pp. 3212–3217). IEEE.*

Rusu, R.B., Cousins, S., 2011. 3D is here: Point Cloud Library (PCL). *In IEEE International Conference on Robotics and Automation (ICRA), Shanghai, China, May.*

Rüeger, J.M., 1990. Electronic Distance Measurement: an Introduction, third ed. Springer-Verlag, Heidelberg, Germany.

Sahillioglu, Y. and Yemez, Y., 2012. Minimum-distortion isometric shape correspondence using EM algorithm. *IEEE Transactions on Pattern Analysis and Machine Intelligence, 34 (11), pp. 2203–2215*.

Salvi, J., Matabosch, C., Fofi, D., Forest, J., 2007. A review of recent range image registration methods with accuracy evaluation. *Image and Vision Computing 25 (5), 578–596.*

Schaffrin, B., and Wieser, A. 2008. On weighted total least-squares adjustment for linear regression. *J. Geodesy*, 82(7), *pp.* 415-421.

Schaffrin, B., Snow, K., 2010. Total least-squares regularization of Tykhonov type and an ancient racetrack in Corinth. *Linear Algebra and its Applications, 432(8), 2061-2076.*

Schulz, T. 2008. Calibration of a Terrestrial Laser Scanner for Engineering Geodesy. Ph. D. Thesis in Institut für Geodäsie und Photogrammetrie, ETH, Zürich.

Sharp, G. C., Lee, S. W., Wehe, D. K., 2002. ICP registration using invariant features. *IEEE Transactions on Pattern Analysis and Machine Intelligence 24 (1), 90–102*.

Shen, Y., Li, B., Chen, Y., 2011. An iterative solution of weighted total least-squares adjustment. *Journal of Geodesy, 85(4), 229-238.*

Smeets, D., Hermans, J., Vandermeulen, D. and Suetens, P., 2012. *Isometric deformation invariant 3D shape recognition. Pattern Recognition, 45 (7), pp. 2817–2831*.

Snow, K. B. (2012). Topics in total least-squares adjustment within the errors-in-variables model: singular cofactor matrices and prior information (PhD dissertation, The Ohio State University).

Soucy, G., Ferrie, F.P., 1997. Surface recovery from range images using curvature and motion consistency. *Computer Vision and Image Understanding, 65(1), 1-18.*

Soudarissanane, S., Lindenbergh, R., Menenti. M. and Teunissen, P. 2009. Incidence angle influence on the quality of terrestrial laser scanning points. *Laser scanning 2009, IAPRS, Vol. XXXVII, part 3/W8, pp. 183-188*

Soudarissanane, S., Lindenbergh, R., Menenti. M. and Teunissen, P. 2011. Scanning geometry: Influencing factor on the quality of terrestrial laser scanning points. *ISPRS Journal of Photogrammetry and Remote Sensing 66 (4), pp. 389-399.*

Staiger, R., 2005. The Geometrical Quality of Laser Scanner (TLS).In: *Proc. of FIG Working Week 2005 and GSDI-8, Cairo, Egypt, April* 16-21.

Strutz, T., 2016. Data Fitting and Uncertainty (2nd edn). Springer.

Sun, J., Ovsjanikov, M., and Guibas, L., 2009. A concise and provably informative multiscale signature based on heat diffusion. *Computer Graphics Forum, 28 (5), pp. 1383–1392*.

Tam, G.K., Cheng, Z.Q., Lai, Y.K., Langbein, F.C., Liu, Y., Marshall, D., Martin, R.R., Sun, X.F. and Rosin, P.L., 2013. Registration of 3D point clouds and meshes: a survey from rigid to non-rigid. *IEEE Transactions on Visualization and Computer Graphics, 19 (7), pp. 1199–1217*.

Tarel, J. P., Civi, H., Cooper, D. B., 1998. Pose estimation of free-form 3D objects without point matching using algebraic surface models. *In Proceedings of IEEE Workshop Model Based 3D Image Analysis (pp. 13-21).*

Tenenbaum, J.B., De Silva, V. and Langford, J.C., 2000. A global geometric framework for nonlinear dimensionality reduction. *Science, 290, pp. 2319–2323*.

Tevs, A., Bokeloh, M., Wand, M., Schilling, A. and Seidel, H.P., 2009. Isometric registration of ambiguous and partial data. *In Proceedings of IEEE Conference on Computer Vision and Pattern Recognition. CVPR 2009 (pp. 1185–1192). IEEE.*

Tevs, A., Berner, A., Wand, M., Ihrke, I., Bokeloh, M., Kerber, J. and Seidel, H.P., 2012. Animation cartography—intrinsic reconstruction of shape and motion. *ACM Transactions on Graphics (TOG), 31 (2), p.12.*

Thiel, K-H., and Wehr, A., 2004. Performance capabilities of laser scanners – an overview and measurement principle analysis. *In: Proceedings of the ISPRS working group VIII/2 "Laser scanner for Forest and landscape assessment", Freiburg, Germany, October 3-6.*

Theiler, P.W., Wegner, J.D. and Schindler, K., 2014. Keypoint-based 4-Points Congruent Sets–Automated marker-less registration of laser scans. *ISPRS Journal of Photogrammetry and Remote Sensing, 96, pp. 149–163.*

Trucco, E., Fusiello, A., Roberto,V., 1999. Robust motion and correspondence of noisy 3-d point sets with missing data. *Pattern Recognition 20 (9), 889–898.*

Valanis, A., and Tsakiri, M., 2004.Automatic target identification for laser scanners. *In: Proc. of the XXth ISPRS Congress, Istanbul, Turkey, July 12-23.*

Van Gosliga R, Lindenbergh R, Pfeifer N. Deformation analysis of a bored tunnel by means of terrestrial laser scanning [M]. na, 2006.

Van Huffel, S., & Vandewalle, J. (1991). The total least squares problem: computational aspects and analysis (Vol. 9). Siam.

Wujanz, D., D. Krueger, and F. Neitzel. 2013. Defo Scan++: Surface based registration of terrestrial laser scans for deformation monitoring. Proceedings of 2nd Joint International Symposium on Deformation Measurement (JISDM), Nottingham.

Wunderlich, T., Wasmeier, P., Ohlmann-Lauber, J., Schäfer, T., Reidl, F., 2013. Objective Specifications of Terrestrial Laserscanners–A Contribution of the Geodetic Laboratory at the Technische Universität München.

Yang, R., Allen, P., 1998. Registering, integrating, and building CAD models from range data. *IEEE International Conference on Robotics and Automation, Levuven, May 16-20, pp. 3115-3120.*

Zinsser, T., Schmidt, J., Niemann, H., 2003. A refined ICP algorithm for robust 3-D correspondence estimation. *In: Proc. International Conference on Image Processing, Barcelona, Spain, 14–18 September, vol. 2, pp. 695–698.*

Zhang, Z. 1994. Iterative point matching for registration of free-form curves and surfaces. *IJCV 13(2): 119–152.*

Zhang, H., Sheffer, A., Cohen‐Or, D., Zhou, Q., Van Kaick, O. and Tagliasacchi, A., 2008. Deformation‐driven shape correspondence. *Computer Graphics Forum, 27 (5), pp. 1431–1439.*

Zhong, Y. 2009. Intrinsic shape signatures: a shape descriptor for 3D object recognition. *In Proceedings of IEEE International Conference on Computer Vision Workshops (pp. 689–696). IEEE.*

Zhou WJ. 1989. Classical theory of error and robust estimation. *Acta Geodaeticaet Cartographica Sinica, 18(2): pp. 115-120 in Chinese.*

List of Figure

List of Table

Acknowledgments

The work on which this thesis is based was carried out in the Department of Geodesy of the Technische Universität München (TUM). I am greatly indebted to all those who contributed to its realization.

First and foremost, I am extremely grateful to *Prof. Dr.-Ing. Thomas Wunderlich*, who gave me the valuable opportunity to pursue a PhD under his supervision. He provided me with scientific freedom and a good working environment. He also made many valuable suggestions for my research. Moreover, my family and I want to thank him for having so much concern for our personal lives.

Second, I would like to express my gratitude to *Prof. Dr.-Ing. Andreas Wieser* from the Institute of Geodesy and Photogrammetry (IGP) of ETH Zürich. Thank you for your guidance and interest in my work.

Thanks to *Prof. Dr.-Ing. Hans-Berndt Neuner* who kindly accepted as a co-reviewer as this thesis.

I am also grateful to *Dr. Peter Wasmeier* for his suggestions for my research and for his assistance in completing so many experiments during the last four years. Also, many thanks are due for translating the abstract of this thesis into German.

Many thanks go to *Dipl. -Ing. Christoph Reith* for his great help in my life. He helped my family and me to integrate into life in Germany.

There were a large number of other people with whom I worked: Dr.-Ing. Wolf-Rüdiger Barth, Dipl. -Ing. Ohlmann-Lauber Johannes, Dipl.-Ing. Andreas Wagner, M. Sc. Wolfgang Wiedemann, Ms. Ingeborg Nominacher, and Mr. Helmut Schreyer. Thank you all for your time and patience!

Thanks also go to my classmates Ms. Khambud Rattikarn, Dr. Ding LingFang, Dr. Jin YanMin,and M. Sc. Yao ZhiHang and to my many friends at Tongji University.

Last, but not least, I would also like to thank my parents, *Mr. Ge QingBin and Ms. Li ChengXiu*, for their patience and for supporting me in every aspect of my life. Thanks go to my parents-in-law, *Mr. Xie Jia* and *Ms. Hu Mang*. Thanks go to my wife, *Ms. Xie Yumeng*, for her company and support. Her unconditional and consistent support, quiet patience, and unwavering love over the last four years were undoubtedly the most vital ingredients that enabled me to finish this work successfully. Finally, I would like to thank my wife again for the priceless gift that she has given us—our baby girl, *Phoenix*. Thanks for coming into our lives, *Phoenix*!